

MESOSCALE MODELING OF DIRECTED SELF-ASSEMBLIES OF BLOCK COPOLYMERS FOR NANOLITHOGRAPHY

A Dissertation

Presented to the Faculty of the Graduate School

of Cornell University

In Partial Fulfillment of the Requirements for the Degree of

Doctor of Philosophy

by

Shubham Dattaram Pinge

May 2019

© 2019 Shubham Dattaram Pinge

MESOSCALE MODELING OF DIRECTED SELF-ASSEMBLIES OF BLOCK
COPOLYMERS FOR NANOLITHOGRAPHY

Shubham Dattaram Pinge, Ph.D.

Cornell University 2019

Over the past decade, with the ever-increasing demand for miniaturization of micro-electronic devices, directed self-assembly (DSA) of block copolymers (BCPs) has attracted the interest of both academia and industry as a promising ‘bottom-up’ technique to develop defect free nanolithographic patterns. DSA is not restricted by inherent diffraction-based limitations of conventional photo-lithography and has a much lower cost of ownership compared to the competing alternatives. Two of the most prominent DSA techniques used to orient BCPs include graphoepitaxy which uses surface topography to direct the BCPs and chemoepitaxy, that employs enthalpic interactions of a patterned substrate to form ordered structures out of thin films. This work first explores graphoepitaxial BCP self-assembly to form ordered cubically packed cylindrical arrays using topographical pillars. Using a coarse-grained molecular dynamics (CGMD) framework, simulations are carried out on an asymmetric BCP confined between two flat plates at two different plate dimensions: least confinement and highest confinement. The least and highest radial separation between adjacent pillars are kept the same as the flat plate separations. A direct correlation was observed in the number of continuous micro-domains of the maximum and minimum confinement dimensions in the pillars template with the least and highest flat plate separations trials. With the optimum chain length employed, the surfaces with affinity to the minor phase can direct the BCP self-assembly to form ordered arrays of minor phase cylinders. Design plots were thus generated at various BCP volume fractions to find the optimum BCP molecular weights.

Secondly, we study chemoepitaxial DSA with Liu-Nealey flow to form lamellae patterns with symmetric BCPs with a CGMD framework. Defect-free lamellae are formed for the two substrate geometries after which the system is quenched below the glass transition. The defect free lamellae are then etched using either a wet or a dry etching schematic. Depending on the type of etching, parameters like solvent type (wet) or selectivity (dry) are studied for their effect on resist morphology. Subsequently, a three-dimensional edge detection is performed on the resist domains (PS) to evaluate the edge roughness on three process stages: anneal, pre-etch and post-dry/wet etch. The simulations results are also compared with top view and cross-sectional SEM images. Efforts to mitigate roughness and defectivity by employing additives, using BCP blends of different molecular weights or replacing a fraction of the BCPs with equivalent homopolymers is also studied. Some common defects and their possible annihilation using suitable dry-etches is then discussed. Lastly, efforts to model the materials and processes for the next-generation lithographic techniques is studied. These include preliminary results for oligomers for self-assembled monolayer nanopatterns and chemically amplified resists for extreme ultraviolet lithography.

BIOGRAPHICAL SKETCH

Shubham Dattaram Pinge was born on March 17, 1992 in the picturesque state of Goa on the western coast of India. He graduated from Mushtifund high school in 2007 and Mushitfund higher secondary school in 2009. He joined the National Institute of Technology Karnataka (NITK) in the coastal town of Surathkal for his undergraduate studies majoring in Chemical Engineering. In his sophomore year he secured a visiting student fellowship at the Raman Research Institute (RRI), Bangalore followed by the Indian National Academy of Engineering fellowship in his junior. He graduated with a Bachelor in technology degree in Chemical Engineering from NITK in 2013.

Upon graduation, he moved to the United States for his graduate studies joining Cornell University for the Masters in Engineering (M.Eng) program in Chemical Engineering. While working for his M.Eng degree, he specialized in polymers processing working on a project developing polymer based rheological modifiers for aqueous petroleum coke slurries under the supervision of Prof. Yong L. Joo. In 2014, he continued his graduate studies working towards his Master of Science in Chemical Engineering at the Joo research group. In the summer of 2015, Shubham joined the PhD program extending his research on self-assemblies of block copolymers for lithography. Upon graduation, Shubham is expected to join the Computational Imaging Technology group at Intel Corporation in Portland, Oregon as a Senior Imaging Scientist.

to my mother, father, and brother

ACKNOWLEDGEMENT

I would like to express my sincerest gratitude to Prof Yong L. Joo for giving me the opportunity to work on this project and guiding me throughout my tenure at Cornell. Prof. Joo's support, research inputs and career advice have been invaluable laying the foundation for my future professional career. I am also thankful to Prof. Ulrich Wiesner, Prof. Susan Daniel, and Prof. Paulette Clancy for their role in my special committee. Their comments, discussions and criticism have helped me improve as a researcher and have greatly shaped my PhD thesis. My special thanks goes to Prof. Tobias Hanrath for attending my B-exam at a short notice. My growth as a graduate student was greatly influenced when I had the opportunity to be a teaching assistant for Prof. Brad Anton. I am thus grateful for his guidance and tips that I believe has helped me improve my communication and teaching skills.

My acknowledgement also goes to my experimental and industrial collaborators at EMD Performance Materials, NJ. The discussions, research inputs, feedback, and experimental data has been extremely useful to collaborate my modeling work throughout my graduate studies. I am also thankful to George Shebert for the numerous discussions and inputs he has provided with regards to my research. I also appreciate the support and help provided by my friends at the Joo research group: Andrew, Joe, Mounica, Chris, Travis, Ghazal, Mohammad, Zhenia, Mani, Ling, and others.

This work used the Extreme Science and Engineering Discovery Environment (XSEDE), which is supported by National Science Foundation grant number ACI-1053575.

Finally, my sincerest gratitude goes to family: my mother, father, and Sumukh. Their support, not just during my graduate studies, but throughout the ups and down of my life cannot be expressed in words.

TABLE OF CONTENTS

Abstract	iii
Biographical Sketch	v
Dedication	vi
Acknowledgements	vii
List of Figures	xiii
List of Tables	xix
Chapter 1: Introduction	1
Chapter 2: Designing an ordered template of cylindrical arrays based on a simple flat plate confinement of block copolymers: a coarse-grained molecular dynamics study	23
2.1 Introduction	23
2.2 Model and methods.....	27
2.2.1 Model details.....	27
2.2.2 Thermostat	29
2.2.3 Confinement templates	31
2.2.4 Simulation details.....	34
2.3 Results and discussions.....	36
2.3.1 Self-assembly under periodic conditions	36
2.3.2 Flat plate study.....	38
2.3.3 Confinement using silica pillars with no substrate	46
2.3.4 Confinement using silica pillars with bottom substrate.....	54

2.3.5 Geometry comparison	56
2.4 Conclusions	61
2.5 References	63
Chapter 3: Three-dimensional line edge roughness in pre-and post-wet-etch line and space patterns of block copolymer lithography	67
3.1 Introduction	67
3.2 Models and methods	71
3.3 Results and discussions	74
3.3.1 Lamellae formation	74
3.3.2 Morphology evaluation with solvent etching	76
3.3.3 Multi-stage LER evaluation	79
3.3.4 Experimental comparison	83
3.4 Summary	89
3.5 References	90
Chapter 4: Mesoscale modeling of directed self-assembly of line and space patterns via ion-bombardment dry-etching	97
4.1 Introduction	97
4.2 Models and Methods	101
4.2.1 Process and simulation parameters	103
4.2.2 Interaction potential between etch beads	105
4.3 Results	106

4.3.1 Optimizing simulation parameters	107
4.3.2 Effect of etch gas pressure	110
4.3.3 Effect of etch gas selectivity	111
4.3.4 Effect of selectivity on resist morphology	113
4.3.5 Multi-stage LER comparisons	116
4.3.6 Dry-etching for substrate with topography	119
4.3.7 Model validation	120
4.4 Summary	122
4.5 References.....	123
Chapter 5: BCP formulation variation: effect on roughness and defectivity.....	127
5.1 BCP blends: effect on edge roughness.....	127
5.2 BCP and homopolymer blends: effect on defectivity	134
5.3 Etching defective systems.....	140
5.4 Additives study for roughness reduction	146
Chapter 6: Future work: next-generation lithography technologies	154
6.1 Nanopatterns using oligomeric self-assembled monolayers.....	156
6.1.1 Introduction.....	156
6.1.2 Model and methodology	158
6.1.3 Results.....	160
6.1.3.1 Self-assembled monolayer on a substrate	161
6.1.3.2 Self-assembled monolayer on a patterned substrate	164

6.1.4 Summary	168
6.2 Stochastics coarse grained molecular dynamics simulations for extreme-ultraviolet resists.....	169
6.2.1 Introduction.....	169
6.2.2 EUV Process	170
6.2.3 Modeling details.....	173
6.2.4 Results.....	175
6.2.4.1 Phase-I (Self-Assembly)	175
6.2.4.2 Phase-II (Photon exposure and PAG dissociation)	176
6.2.4.3 Phase III (Acid deprotection) and Phase IV (development)	177
6.2.5 Summary	180
6.3 References.....	181

LIST OF FIGURES

Figure 1.1. Moore’s law scaling and development of newer nodes with faster, more energy efficient transistors	2
Figure 1.2. Phase diagram and morphologies with comparisons with other studies for BCP bulk self-assembly.....	4
Figure 1.3. Process schemes for graphoepitaxy and chemoepitaxy.....	7
Figure 1.4. Morphology of ordered cylindrical arrays via graphoepitaxy and lamellae via chemoepitaxy	9
Figure 1.5. Schematic for Liu-Nealey flow and subsequent etching to form line and space patterns	10
Figure 1.6. Power spectral density plots for two edge profiles with different low and high frequency contributions	12
Figure 2.1. Geometric templates for BCP confinement (top and side views)	31
Figure 2.2. Phase diagram and morphologies with comparisons with previous studies for BCP bulk self-assembly	36
Figure 2.3. Flat plate BCP morphology for 17σ confinement with concentration plots for minor phase volume fraction 0.3	41
Figure 2.4. BCP-surface interaction pairwise potential phase-space for 17σ confinement with morphology snapshots	43
Figure 2.5. Flat plate BCP morphology for 42σ confinement with concentration plots for minor phase volume fraction 0.3	45
Figure 2.6. Minor phase density plots for BCP with a minor phase volume fraction of 0.3 under ordered pillars confinement.	47

Figure 2.7. Minor phase density plots for three volume fractions and the chain lengths for ordered pillar confinement with surface coverage plots	50
Figure 2.8. Fractional minor phase concentration vs normalized confinement dimension plot for BCP-surface interaction pairwise potential for minor phase volume fraction of 0.25, N_{60}	53
Figure 2.9. Minor phase density xy plots of the morphology formed by pillars with bottom substrate at three volume fractions	54
Figure 2.10. Comparison of the morphologies formed by the flat plate geometries at two confinements -17σ and 42σ with the ordered pillars template at default conditions.	58
Figure 2.11. Design plots to form ordered cylindrical arrays with flat plate studies.....	60
Figure 2.12. Design plots generated by varying minor phase volume fractions to form ordered cylindrical arrays with flat plate studies	60
Figure 3.1. Substrate for LiNe CGMD simulations with flat substrate and substrate with topography	73
Figure 3.2. Morphology profiles after annealing for LiNe flow substrates	75
Figure 3.3. PS Line-Width vs film thickness plots for three solvent types.....	77
Figure 3.4. LER vs film thickness plots along with height averaged LER for the three process stages: anneal, pre-etch and post-etch for two substrate types	80
Figure 3.5. LWR vs film thickness plots along with height averaged LWR for the three process stages: anneal, pre-etch and post-etch for two substrate types	81
Figure 3.6. Height averaged power spectral density for PS domains for the three process stage for flat substrate geometry	83
Figure 3.7. SEM image edge detection with LER histogram and model validation.....	84

Figure 3.8. Surface power spectral density, roughness exponent histogram, correlation length fitting and histogram	86
Figure 3.9. Three-dimensional edge detection for SEM image and comparison with CGMD etched with poor solvent and good solvent	88
Figure 4.1. Schematic of dry-etching setup	100
Figure 4.2. Kinetic evolution of resist morphology with PS selective and PMMA selective etch beads	102
Figure 4.3. Early time velocity distribution for the etch beads for various interaction strengths for the soft-potential.....	107
Figure 4.4. Early time x,y -velocity distribution for a constant V_z	109
Figure 4.5. Resist morphology at three different etch pressures at a constant V_z and selectivity.....	110
Figure 4.6. Kinetic evolution of resist profile at constant pressure and at three different selectivities.....	112
Figure 4.7. Effective selectivity calculated at complete PMMA removal as a function of imposed simulation selectivity	113
Figure 4.8. Line-Width variation for different etch selectivities	114
Figure 4.9. LER variation for different etch selectivities for the left and right edge of the three domains	115
Figure 4.10. LER variation for the three process stages: anneal, pre-etch and post-etch for the left and right edge of the three domains	116
Figure 4.11. Height averaged LER comparison for the three domains for the three process stages: anneal, pre-etch and post-dry etch	117

Figure 4.12. Power-spectral density plots for the three process stages for dry etching.....	118
Figure 4.13. Kinetic evolution of a resist for a substrate with topography	120
Figure 4.14. Model validation by comparing the experimental SEM image roughness values with CGMD dry-etch and CGMD wet-etch.....	121
Figure 5.1. Concentration plots for scheme-2 and scheme-3 BCP blend for the anneal and pre-etch process stage	129
Figure 5.2. Line-Width Roughness (LWR) and Line-Width vs film thickness for the two blends, scheme-2 and scheme-3 compared to the scheme-1 in default.....	131
Figure 5.3. Line-Edge Roughness vs film thickness for the left and right edges for the three resist domains for the BCP blends	132
Figure 5.4. Height averaged roughness values for BCP blends.....	133
Figure 5.5. Morphologies seen for LiNe DSA flow: lamellae, angled lamellae and defects	134
Figure 5.6. Ease of lamellae formation for the BCP blends	135
Figure 5.7. Effect of homopolymer addition on defectivity	137
Figure 5.8. Larger simulation box with dislocation defects with two PS patterning line in the x-direction	138
Figure 5.9. Three defective BCP systems chosen for etching studies	140
Figure 5.10. Time snapshots for etching on a defective morphology for system-I for four selectivities.....	142
Figure 5.11. Time snapshots for etching on a defective morphology for system-II for four selectivities.....	144
Figure 5.12. Time snapshots for etching on a defective morphology for system-III for selectivity = 2.5	145

Figure 5.13. Morphology formed for neutral <i>N7</i> additive for 3X multiplication.	148
Figure 5.14. Effect of oligomeric chain length for 2.5 % neutral additive concentration and substrate 2X multiplication and effect of oligomeric concentration for <i>N5</i> neutral oligomers and 2X substrate	149
Figure 5.15. Effect of additives on the BCP interfacial width.....	150
Figure 5.16. BCP structure manipulation with additives	151
Figure 5.17. Concentration spread for tri-BCP and interfacial width for PS-PMMA and third block BCP spread.....	152
Figure 5.18. Concentration spread for the pendant group for three pendant types for <i>N2</i> and effect of chain length for pendants repulsive to PS and PMMA	153
Figure 6.1. Schematic of using SAMs with atomic layer deposition.....	156
Figure 6.2. Bulk self-assembly of the oligomer	160
Figure 6.3. Biased unpatterned and patterned substrate with dimensions along with morphology of the system after the self-assembly phase and subsequent monolayer formation.....	162
Figure 6.4. Morphology after self-assembly and monolayer formation for biased unpatterned substrate for <i>N5</i> at four film thicknesses with bead tethering and surface coverage statistics ...	164
Figure 6.5. Patterned substrate (type-I) self-assembly and monolayer formation for two oligomeric chain lengths	165
Figure 6.6. Patterned substrate (type-II) self-assembly and monolayer formation for two oligomeric chain lengths	166
Figure 6.7. Chain tethering statistics for substrate type-I and type-II for chain length <i>N5</i> and <i>N10</i>	167
Figure 6.8. EUV process schematic and individual components for each stage	170

Figure 6.9. Polymer resin types for chemically amplified EUV resists.....	171
Figure 6.10. Morphology of the chemically amplified resist after phase-I along with the concentration spread for additives	175
Figure 6.11. Morphology post-EUV exposure and acid dissociation along with a schematic of acid deprotection to a resist chain.....	176
Figure 6.12. Acid deprotection kinetics schematic	177
Figure 6.13. Effect of acid reactivity with variable acid bead reactive radius on deprotection along with concentration profiles	179

LIST OF TABLES

Table 2.1. Types of long-range pairwise potential interactions for pillars / flatplate study.....	29
Table 2.2. Parameters for the pillars/flat plate confinement studies	35
Table 2.3. Polymer chain statistics for 17 σ confinement.	40
Table 2.4. Polymer chain statistics for 42 σ confinement.	46
Table 4.1. Comparison of Ar and O ₂ etch chemistry.	199
Table 5.1. Interactions of the various types of additives with other bead types in the simulation for tri-BCP.....	147

CHAPTER 1

INTRODUCTION

The fabrication of microchips requires variety of intricate physical and chemical processes. Nanolithography is often employed to produce these micro and nanopatterns¹⁻². The conventional mode of manufacturing these devices involves the use of a top-down process called photolithography³⁻⁴. Even though the process has its limitation, it has fulfilled the expectations of Moore's Law²⁵ for decades largely due to the innovative engineering solutions to the fundamental issues. This innovation has paved the way for a more connected and accessible globe driving growth in the modern digital age. From personal computers and mobile devices to storage devices, data centers and even telecommunication systems, the strive to produce faster devices with more features with minimal leakage and power consumptions has truly transformed the world as we see it.⁵ (figure 1.1)

The impact of the progress of the semiconductor industry can be assessed to be manifold⁵. We have economic impact, wherein high performance, energy efficient devices have been developed by fitting more transistors per unit area. The end cost to the user has also reduced over the years. If we compare the Intel4004 chip first produced in 1971 with the Intel i7 Skylake, 14 nm processor (2015), the performance of the newer processor is 3500 times better at 90,000 times higher efficiency and remarkably at 1/60,000 the price of the older technology!⁵⁻⁶ This development with improved computational power has led to significant technological progress in other industries like automotive, construction, pharmaceutical to name a few.

It has also paved way for industries for the coming decade like high performance computing, data science, machine learning to even the vast empire of the social media. The societal impact is also noteworthy. Computers have helped us develop lifesaving drugs, optimized energy productions, put satellites in orbits, build bridges, dams, and skyscrapers and countless more tasks without which the world today would be unrecognizable as we know it. The heart of this progress lies in the scaling of Moore's law and the ingenuity of the researchers in developing photolithography have helped us scale Moore's Law for over five decades now.

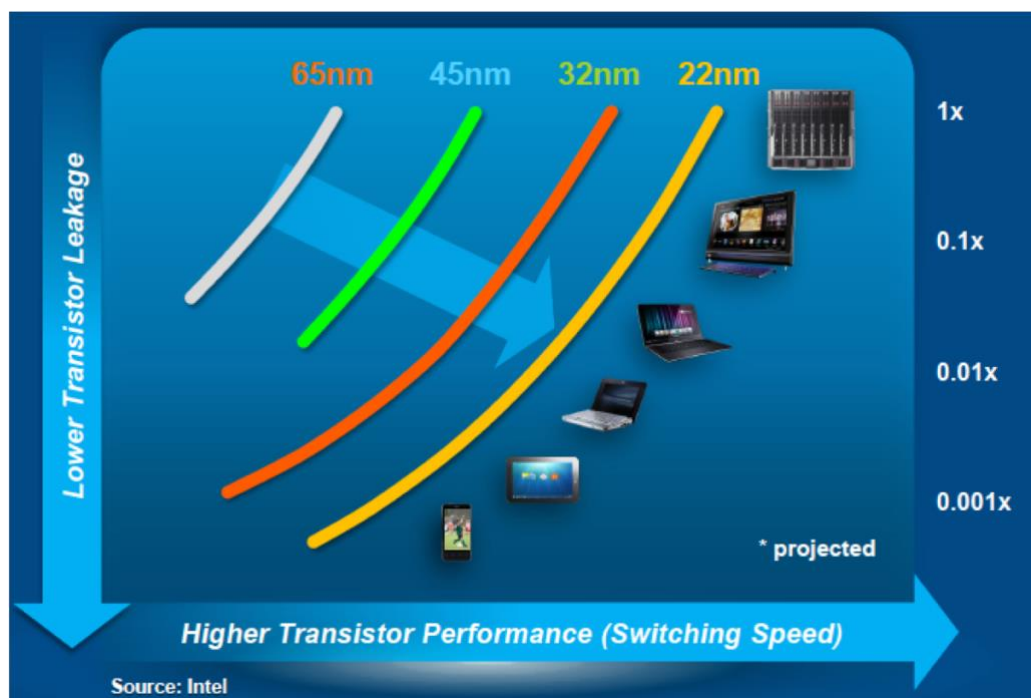


Figure 1.1: Moore's law scaling and development of newer nodes with faster, more energy efficient transistors. Figure adapted from Vivek Singh. *EUV: The Computational Landscape. EUVL Workshop 2014.*⁷

Photolithography uses one or multiple optical sources, photo resists and photo masks but also requires the use of resolution enhancement techniques like optical proximity correction, phase shift

masks making it economically less viable⁸⁻⁹. It has the primary disadvantage of diffraction-based limits for the features produced⁸. To produce devices with smaller features, it is essential to reduce the wavelength of the optical sources and this can be cost ineffective. Critics of photolithography have been predicting the demise of the technology for a few years now¹⁰⁻¹¹. Researchers have suggested the need for a major technological break in the coming years to prevent any disruption in the scaling. Eventually, it is expected that the industry will move to a non-Silicon based technology. But the vast infrastructure and the knowledge developed on Silicon based technologies requires the immediate development and subsequent production of alternatives to photolithography.

Other top-down techniques like extreme ultra-violet lithography (EUV)¹² have thus gained recent popularity. Intel is expected to start production of the 7nm node using EUV by 2020-21 and has thus invested billions of dollars developing the technology. Although the overall outlook looks bright, there are still some concerns for high-volume manufacturing.¹⁴ Issues arising out of shot noise of the EUV source is a fundamental issue that experts believe strongly affect the technology performance. The photon density for EUV is significantly lower than photolithography, thus any variation in the photon energy distribution leads to stochastic variation in the resists and subsequent pattern transfer¹⁵. EUV also has a high cost of ownership and may not be an economical alternative to manufacture entry-level devices.

A viable alternative bottom-up technique to form sub-20 nm features comparable to extreme ultra-violet lithography with hierarchical structure formation and long-range order but significant reduction in cost-of-ownership is directed self-assembly (DSA) using block copolymers (BCPs)¹⁻

2, 16-21. As the demands of lower sizes with higher densities for magnetics storage devices²², flash memory devices²³, semiconductor capacitors²⁴ among others continue to spread, the technology has attracted considerable attention of academia and industry alike. The harmonic spatial arrangement and periodicity offered by the technique offers manufacturers new strategies for the fabrication of electronic and energy storage devices. In accordance with Moore's Law²⁵, the demand for manufacturing high performance devices economically is estimated to surge in the coming years and researchers are expected to develop DSA lithography to form defect free patterns²⁶ with optimal control and tolerance on the lithographic features.

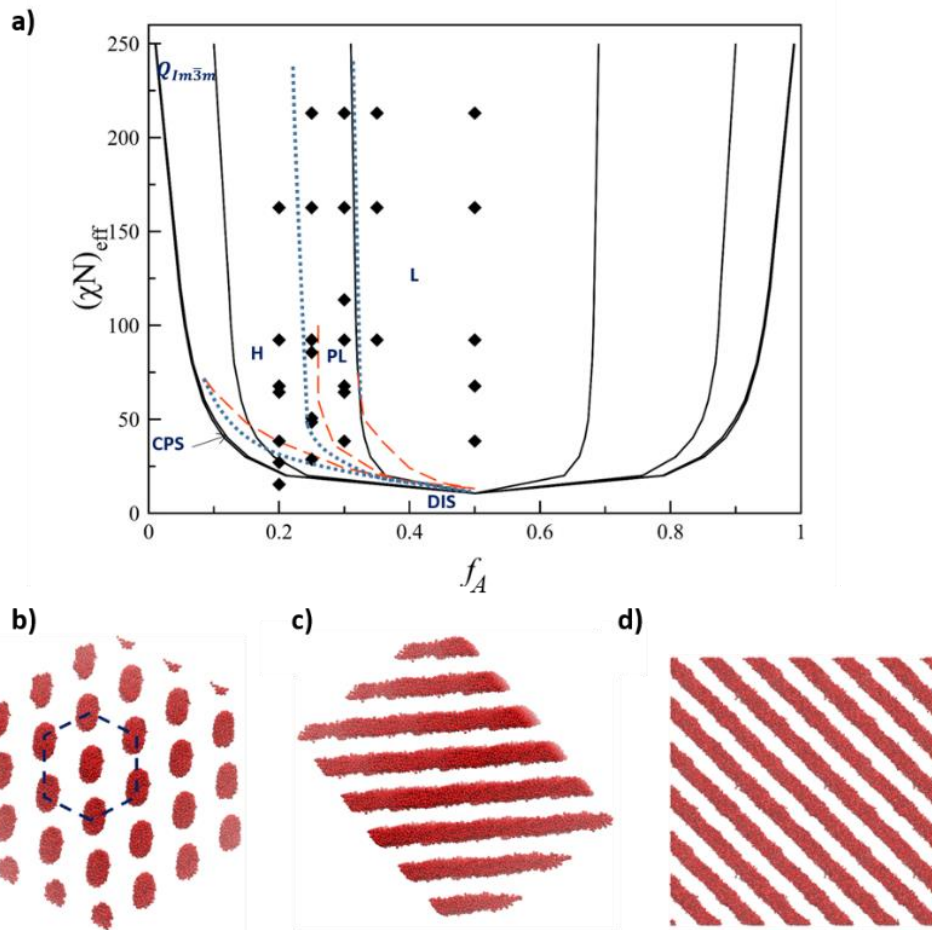


Figure 1.2: a) BCP self-assembly phase diagram. H=Hexagonally packed cylinders, PL=perforated Lamellae, L=Lamellae, DIS=disordered, CPS=Cubically packed spheres. The dotted blue lines signify the phase boundary by this study. Refer Chapter 2 for further details. b) Hexagonally packed cylinder morphology. c) perforated lamellae (perforation not seen) d) Lamellae morphology

BCPs self-organize at molecular level building blocks and forming nano-structures like lamellae, hexagonally packed cylinders, gyroids and spherical micelles with characteristic length scales on the order of 5-50 nm^{27,28}. As some of these nano-structures resemble the lithographic features desired in the semi-conductor industry, they are used as a nano-template in the manufacture of micro-chips. As the two blocks in a di-block copolymer tend to differ in their chemical properties (incompatible with each other), they favor separating out into two phases forming micro-domains. The morphology formed by the BCPs depend on three main factors: the Flory-Huggins parameter (χ), the volume fraction of the minor phase (f_A) and the degree of polymerization (N)^{27,28}. The latter two factors are governed by the polymerization stoichiometry and influence the translational and configurational entropy. As evident from the equation below, the Flory-Huggins parameter has an enthalpic contribution, α and an excess entropic contribution β ²⁹.

$$\chi = \alpha T^{-1} + \beta \quad \text{equation 1.1}$$

The coefficients α and β depend on the temperature (T), f_A , N and the material property of the monomers. Polymer melts are often modelled as Gaussian chains comprising of spherical beads. These molecules often exhibit building-block anisotropy similar to various shaped nano-colloidal particles³⁰. To account for this anisotropy of the monomer beads and the non-random nature of their mixing, the entropic contribution β is introduced in the expansion of the Flory Huggins term²⁹. The entropic contribution becomes all more crucial in cases where the confinement dimension is comparable to the BCP domain size, a “two-dimensional melt” as opposed to a bulk melt³¹. Some examples of such systems include polymers confined with topographic features as

employed in DSA techniques or chains on adsorbed layers like lipid bilayer systems. The chains in these systems are highly confined. They strongly segregated and show only slight overlap. Contrastingly, in a three-dimensional melt chains interpenetrate strongly behaving ideally as evident from the self-consistent argument. In either case, the chains tend to spatially re-organize or self-assembly so as to minimize the free energy of the system.

The process of BCP self-assembly that is exclusively thermodynamically driven is slow, with limited control on the domain size and sometimes with poor degree of micro-phase separation. The morphology of the system may have a strong local order but, in many cases, lack long range orientational and translational order. DSA combined with advanced lithographic techniques offers an additional driving force that provides orientational order to create patterns suitable for lithographic applications.

Several reports have also demonstrated the use of simple shear and extensional flows to polymer melts and BCP films to better form the desired hierarchal structures³²⁻³⁶. Application of such external force fields can better align lamellar¹⁹, cylinder and to a certain extent spherical micelles micro-domain with increased order in one or more dimensions³⁵. In some cases where the external field is flow induced, as the size of micro-domains of the system of interest is reduced and we transition from bulk to thin films, its efficiency diminishes. Other force fields in the form of electric and magnetic fields have also been employed to improve the BCP ordering. The need of continuous electrode contact for the process and significantly high BCP dielectric constant with risks of its breakdown during the self-assembly limits the scalability in using electric field for alignment. For magnetic force fields to be effective to drive the ordering, it requires the use of a specialized

polymer or a superconducting magnetic field often produced by using NMR which makes the process less attractive as compared to the economical alternatives¹⁹. For its effectiveness and affordability, most commonly employed DSA techniques in the semi-conductor industry include chemoepitaxy³⁷ and graphoepitaxy³⁸⁻³⁹.

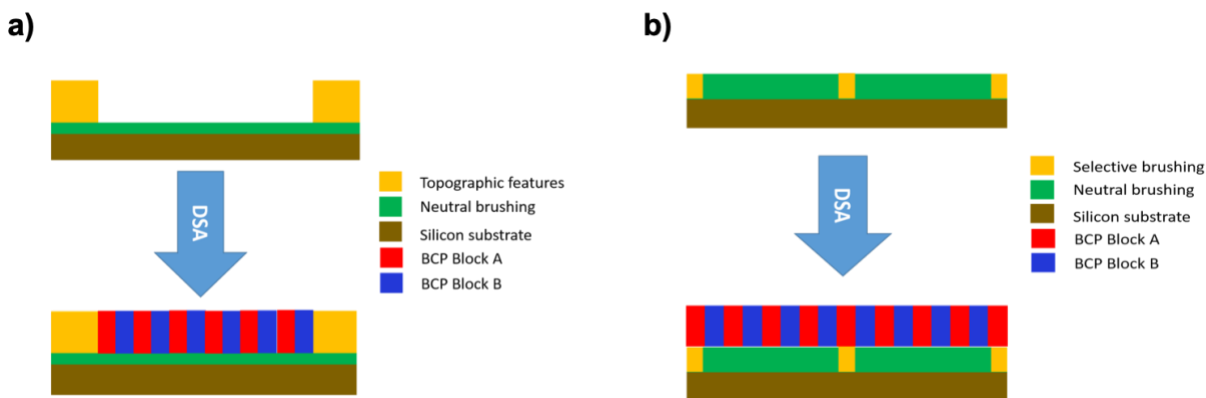


Figure 1.3: Process schemes for a) graphoepitaxy and b) chemoepitaxy. Graphoepitaxy uses surface topography to direct BCPs while chemoepitaxy use patterned substrate to direct.

Graphoepitaxy³⁸⁻³⁹ is another class of DSA that uses topography and surface roughness to direct the self-assembly, most commonly employed for asymmetric BCPs with volume fractions close to 0.3 (figure 1.3a). The surface features and the substrate can also be chemically treated to provide an additional driving force. The polymer in this case experiences entropic constraints arising from the confinement of the topography. The resulting BCP morphology formed is of periodic arrays of cylinders while the nano-lithographic pattern formed is called a ‘contact-hole’ (figure 1.4 a). The contact hole cylinder template is used in the manufacture of integrated circuit micro-chips for the flow of electrons using vertical interconnect access (*via*), physically connecting multiple or adjacent layers. These *via* connect electrodes likes gates, sources, and drains of transistors for very large-scale integration circuits and is considered one of the most difficult lithographic challenge.⁴⁰

In the second chapter of this work we tackle this challenge by studying the formation of contact hole patterns with graphoepitaxial DSA using coarse-grained molecular dynamics simulations. We start with a simple flat plate confinement with the bottom and top substrate attractive to the minor phase at two confinement lengths. The results obtained in the flat plate study with the least and highest confinement dimensions were used to design a topography of silica pillars with and without a bottom substrate to form ordered cylindrical BCP arrays. The least and highest radial separation between adjacent pillars are kept the same as the flat plate separations. A direct correlation was observed in the number of continuous micro-domains of the maximum and minimum confinement dimensions with the 17σ and 42σ flat plate trials. With the optimum chain length employed, the surfaces with affinity to the minor phase can direct the BCP self-assembly to form ordered arrays of minor phase cylinders. Design plots were thus generated for the experimentalists to know the working regime in terms of the BCP molecular weight for a fixed BCP volume fractions and pillar geometry and separation.

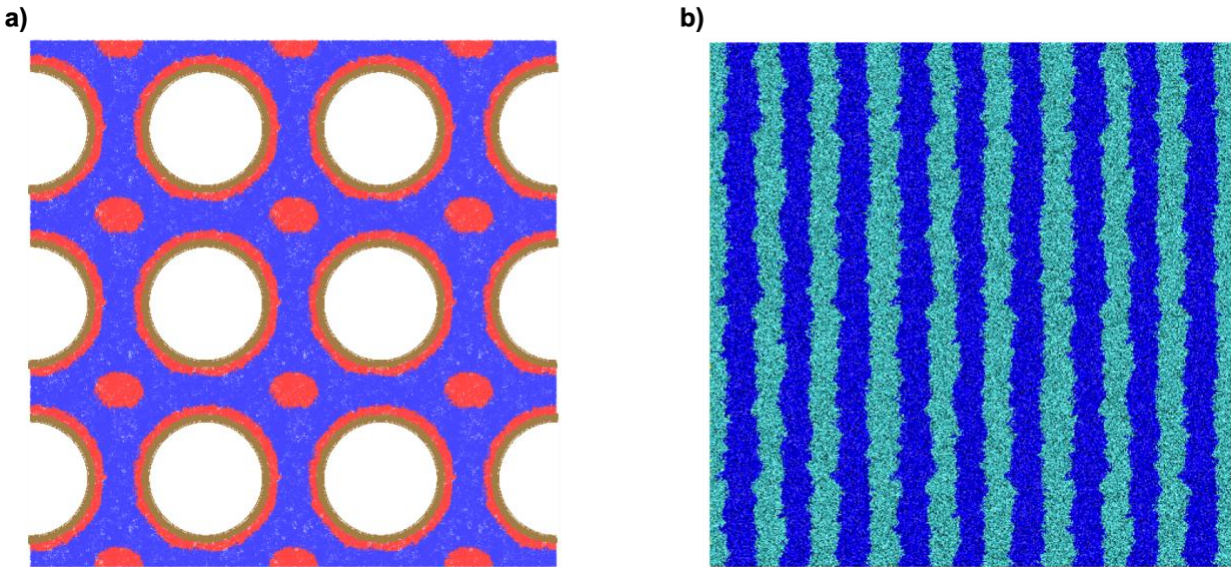


Figure 1.4 a) Morphology of an ordered cylindrical arrays formed by asymmetric BCP. When the minor phase (red) is etched off, the pattern so formed is a contact hole pattern. b) Morphology of ordered defect free lamellae. When one of the phases is etched off, the morphology formed will be a line and space pattern

Chemoepitaxy^{16, 37} utilizes chemicals that have been carefully crafted on a relatively flat substrate to direct the self-assembly. The chemical pattern is selective to one of the two phases which helps in aligning the block copolymer domains. The morphology usually probed in this technique is lamellae and the nano-lithographic pattern thus formed is called a line and space pattern. One of the lamellae blocks is then etched away which serves as a pathway for the two-dimensional flow of electrons in the manufacture of logic gates.

The most popular technique for this approach is DSA with LiNe⁴¹⁻⁴² flow (named after its inventors Liu and Nealey). The current industry standard for the BCP is polystyrene-block-polymethyl methacrylate (PS-*b*-PMMA). Using this technique, chemically patterned substrates can effectively direct dense arrays of features with long-range order over wide areas. The BCP thin film is guided using a part of a substrate that has chemical affinity towards one of the blocks. In figure 1.5, the

PS-pinned region (PS mat) is coated with short chained PS brushes while the rest of the substrate is coated with a random PS-*b*-PMMA brush (neutral layer)

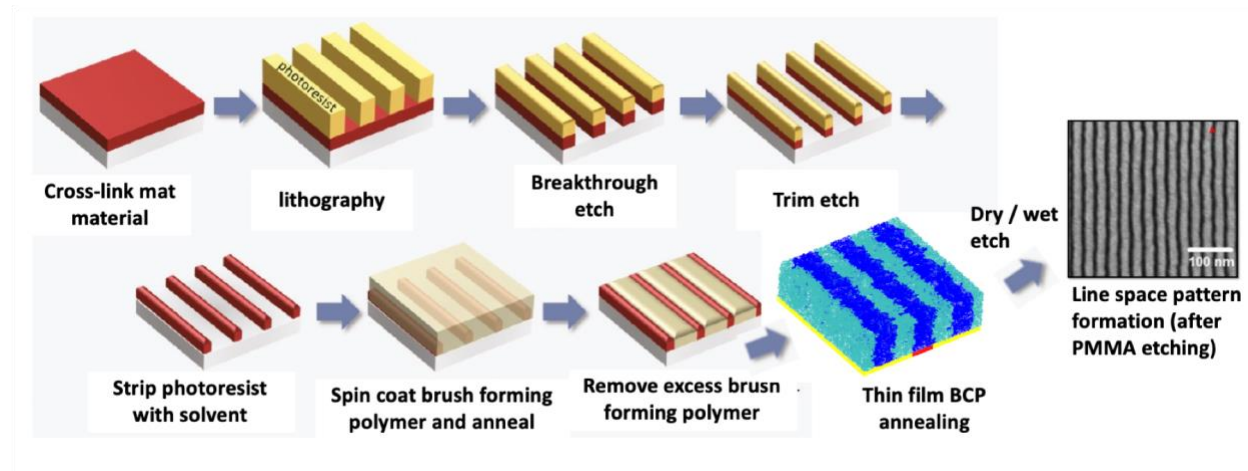


Figure 1.5 Schematic for Liu-Nealey flow and subsequent etching to form line and space patterns. Cartoon adapted from Liu *et. al*⁴¹

The process starts with spin-coating a cross-linked PS mat to form a resist layer. This pattern is subjected to an advanced lithographic technique like 193 nm immersion lithography or e-beam lithography and subsequently etched to create a patterned substrate⁴³. The pitch is of this patterning is two to five times higher than what is desired from subsequent DSA. We can define a pattern multiplication as half the number of BCP domains of minor and major phase that exists between the patterning on the substrate. The system is further etched to expose some of the cross-linked mat at the required location in breakthrough etch. This is followed by etching off the mat to trim its height so that the dimensions and width of the patterning is as desired. The photoresist is then stripped with a solvent and the space in between the polymer is spin coated with random polymer brushes (PS-*b*-PMMA). These random brushes are about 12,000 gmol⁻¹ for BCP of periods 28-30 nm. The system is then annealed, and excess brush is removed to form a LiNe flow chemically patterned substrate. This substrate will possess some topography with the patterned line being at a

higher height than the surrounding neutral brush. A thin-film of BCP is then spin-coated to a thickness of $\sim 1.2L_0 = 35$ nm. It is important that the film thickness be at least $1 \times L_0$ so as to prevent formation of undesired structures. After the self-assembly if the structure form is void of any defects, the minor phase is etched off using either a dry or a wet etch scheme. Dry etching is the preferred method for line and space patterns to prevent any pattern collapse induced by solvents during low solvent conditions post etching. Dry etching is most popularly carried out using an Ar/O₂ plasma while wet etching with acetic acids⁴⁴.

The line and space patterns formed are seldom smooth (figure 1.4b) as the BCPs have inherent roughness due to the spread of its interfacial widths. The etching process can also contribute to this roughness. This roughness is characterized as Line-Edge Roughness (LER)⁴⁵⁻⁴⁶ which is defined as the 3σ edge deviation from the average value. The International Technology Roadmap for Semiconductors (ITRS) has identified sub 2nm Silicon LER values for the 14nm node currently being explored with LiNe flow DSA. It is also crucial to note that the LER possess information both in space and frequency domains. As seen in figure 1.6, two edges may have the same 3σ magnitude of roughness but its response in the Fourier domain can be totally different with varying contributions for the high and low frequency roughness.⁴⁷

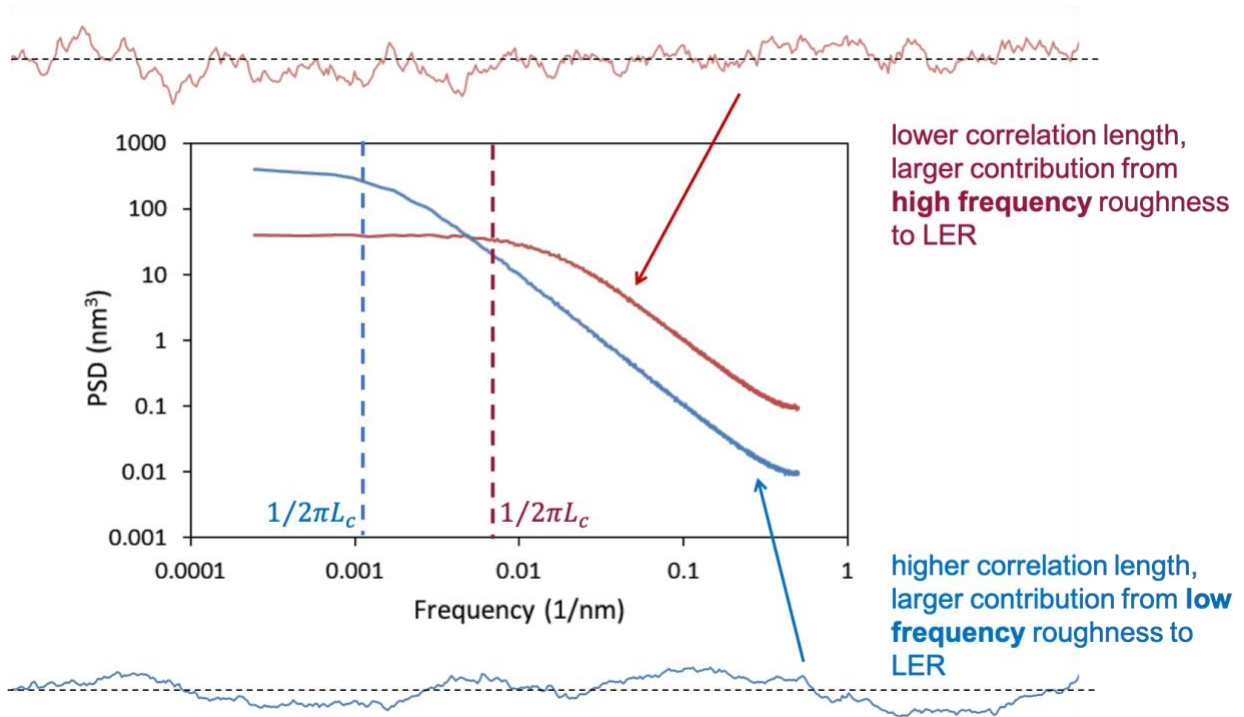


Figure 1.6: Power spectral density plots for two edge profiles with different low and high frequency contributions

High roughness values can lead to catastrophic failures of the transistor device. Rough edges lead to hindrance of electron flows leading to discrepancies in the resistances and capacitances of the device. Low frequency roughness leads to variation in line to line edges and high frequency roughness leads to major failures due to in-line variation. Hence for possible future commercialization of this technology it is crucial simulate, model and characterize the roughness along with the high and low frequency contributions at various process stages.

In line with above stated goal, in chapter 3, we employ large-scale coarse-grained molecular dynamics (CGMD) simulations to study the three-dimensional line edge roughness associated with the line and space patterns of chemo-epitaxially directed symmetric BCPs. The diblock copolymer (BCP) chain length and interaction parameters are validated with experimental BCP period, L_0 and

corresponding molecular weight. Two types of substrate geometries are studied in the simulations: a) flat and b) substrate with topography. Defect-free lamellae are formed for the two geometries after which the system is quenched below the glass transition before selectively wet-etching off one of the BCP phases. Three types of etching solvent and its effect of the resist domain morphology post-etch is studied. The Line Edge Roughness of the polymer domains is evaluated over three process stages: anneal, pre-etch and post-etch in presence of a selective solvent. Power spectral density plots are then generated to elucidate the contribution of low and high frequency roughness for the three process stages. Finally, we show that the roughness values obtained from the simulations are in close agreement with the experimental SEM images. The SEM images are also analyzed to obtain the roughness exponent and correlation length inherent to the process and the BCP.

In Chapter 4, a dry-etching schematic is explored in detail. This etching process would be closer to the experimental trials and the subsequent comparison would also be more precise. The model followed captures ion-bombardment which is the dominant mechanism followed by Ar plasma based etches. Although the most popular etch remains Ar/O₂ dry etch, the amount of O₂ radicals in the system remains around 10%. Thus, the reactive-ion etching mechanism followed by O₂ radicals will be superseded by the ion-bombardment etching. Future improvements are expected to this model that captures reactive-ion etching as well as resist cross-linking. For the current model, a multi-stage LER evaluation is performed just as in chapter 3 in both space and frequency domains.

LER remains one of the two major holdups for possible high-volume manufacturing, the other being high defectivity. Defective nanopatterns in most cases cannot be used for further pattern

transfer to the Silicon. These defects are not the lowest free energy state but a kinetically trapped metastable state. If we wait, for infinite time, the defects will eventually annihilate itself. But the more time we anneal the system, lower will be the throughput and higher will be cost of the process. Hence it is crucial to explore the simulation parameter space and offer useful insights to the manufacturer to attempt those trials with lowest probability to form defects.

In Chapter 5, the BCP formulation is varied and its effect on Line-Edge Roughness as well as defectivity is studied. Formulation variation include: employing BCP blends, replacing fraction of BCP chains with homopolymers and addition of oligomeric additives. The defective trials, their response and possible annihilation via dry-etching is also analyzed in this chapter.

Lastly, efforts to model the materials and processes for the next-generation lithographic techniques is studied. These include preliminary results for oligomers for self-assembled monolayer nanopatterns and chemically amplified resists for extreme ultraviolet lithography.

REFERENCES

1. Stoykovich MP, Kang H, Daoulas KC, Liu G, Liu CC, de Pablo JJ, Müller M, Nealey PF. Directed self-assembly of block copolymers for nanolithography: fabrication of isolated features and essential integrated circuit geometries. *Acs Nano*. 2007 Oct 1;1(3):168-75.
2. Jeong SJ, Kim JY, Kim BH, Moon HS, Kim SO. Directed self-assembly of block copolymers for next generation nanolithography. *Materials Today*. 2013 Dec 31;16(12):468-76.
3. Levinson HJ. *Principles of lithography*. SPIE press; 2005.
4. Brock DC, Moore GE, editors. *Understanding Moore's law: four decades of innovation*. Chemical Heritage Foundation; 2006.
5. Over 50 Years of Moore's Law [Internet]. Intel.com. [cited 2019Jan19]. Available from: <https://www.intel.com/content/www/us/en/silicon-innovations/moores-law-technology.html>
6. The Story of the Intel® 4004 [Internet]. Intel.com. [cited 2019Jan19]. Available from: <https://www.intel.com/content/www/us/en/history/museum-story-of-intel-4004.html>
7. Vivek Singh. EUV: The Computational Landscape. EUVL Workshop, 2014. Available from: <https://www.euvlitho.com/2014/P1.pdf>
8. Mack CA. *Field guide to optical lithography*. Bellingham, Washington, USA: SPIE Press; 2006 Jan 24.

9. Fritze M, Tyrrell BM, Astolfi DK, Lambert RD, Yost DR, Forte AR, Cann SG, Wheeler BD. Subwavelength optical lithography with phase-shift photomasks. *Lincoln Laboratory Journal*. 2003;14(2):237-50.
10. Waldrop MM. The chips are down for Moore's law. *Nature News*. 2016 Feb 11;530(7589):144.
11. Schulz M. The end of the road for silicon?. *Nature*. 1999 Jun;399(6738):729.
12. Wu B, Kumar A. Extreme ultraviolet lithography: a review. *Journal of Vacuum Science & Technology B*. 2007 Nov 1;25(6):1743-61.
13. Shilov A. Intel: EUV-Enabled 7nm Process Tech is on Track [Internet]. RSS. AnandTech; 2018 [cited 2019Jan19]. Available from: <https://www.anandtech.com/show/13683/intel-euvenabled-7nm-process-tech-is-on-track>
14. Tyson M. Intel optimistic over 7nm EUV node schedule [Internet]. Corporate - News - HEXUS.net. HEXUS; 2018 [cited 2019Jan19]. Available from: <https://hexus.net/tech/news/cpu/125156-intel-optimistic-7nm-euv-node-schedule/>
15. Brainard RL, Trefonas P, Lammers JH, Cutler CA, Mackevich JF, Trefonas A, Robertson SA. Shot noise, LER, and quantum efficiency of EUV photoresists. In *Emerging Lithographic*

Technologies VIII 2004 May 20 (Vol. 5374, pp. 74-86). International Society for Optics and Photonics.

16. Ruiz R, Kang H, Detcheverry FA, Dobisz E, Kercher DS, Albrecht TR, de Pablo JJ, Nealey PF. Density multiplication and improved lithography by directed block copolymer assembly. *Science*. 2008 Aug 15;321(5891):936-9.
17. Kim J, Wan J, Miyazaki S, Yin J, Cao Y, Her YJ, Wu H, Shan J, Kurosawa K, Lin G. The SMART TM Process for Directed Block Co-Polymer Self-Assembly. *Journal of Photopolymer Science and Technology*. 2013;26(5):573-9.
18. Kim SO, Solak HH, Stoykovich MP, Ferrier NJ, de Pablo JJ, Nealey PF. Epitaxial self-assembly of block copolymers on lithographically defined nanopatterned substrates. *Nature*. 2003 Jul 24;424(6947):411-4.
19. Hu H, Gopinadhan M, Osuji CO. Directed self-assembly of block copolymers: a tutorial review of strategies for enabling nanotechnology with soft matter. *Soft matter*. 2014;10(22):3867-89.
20. Koo K, Ahn H, Kim SW, Ryu DY, Russell TP. Directed self-assembly of block copolymers in the extreme: guiding microdomains from the small to the large. *Soft Matter*. 2013;9(38):9059-71.

21. Park C, Yoon J, Thomas EL. Enabling nanotechnology with self assembled block copolymer patterns. *Polymer*. 2003 Oct 31;44(22):6725-60.
22. Cheng JY, Ross CA, Chan VH, Thomas EL, Lammertink RG, Vancso GJ. Formation of a cobalt magnetic dot array via block copolymer lithography. *Advanced Materials*. 2001 Aug 1;13(15):1174-8.
23. Guarini K, Black C, Zhang Y, Babich I, Sikorski E, Gignac L. Low voltage, scalable nanocrystal FLASH memory fabricated by templated self assembly. In *INTERNATIONAL ELECTRON DEVICES MEETING 2003 Dec 8* (pp. 541-544). IEEE; 1998.
24. Black CT, Guarini KW, Milkove KR, Baker SM, Russell TP, Tuominen MT. Integration of self-assembled diblock copolymers for semiconductor capacitor fabrication. *Applied Physics Letters*. 2001 Jul 16;79(3):409-11.
25. Moore GE. Cramming more components onto integrated circuits, Reprinted from *Electronics*, volume 38, number 8, April 19, 1965, pp. 114 ff. *IEEE Solid-State Circuits Newsletter*. 2006;3(20):33-5.
26. Li W, Müller M. Defects in the self-assembly of block copolymers and their relevance for directed self-assembly. *Annual review of chemical and biomolecular engineering*. 2015 Jul 24;6:187-216.

27. Bates FS, Fredrickson GH. Block copolymer thermodynamics: theory and experiment. Annual Review of Physical Chemistry. 1990 Oct;41(1):525-57.
28. Bates FS, Fredrickson GH. Block copolymers-designer soft materials. Physics today. 2000.
29. Bates FS. Polymer-polymer phase behavior. Science. 1991 Feb 22;251(4996):898-905.
30. Glotzer SC, Solomon MJ. Anisotropy of building blocks and their assembly into complex structures. Nature materials. 2007 Aug 1;6(8):557-62.
31. De Gennes PG. Scaling concepts in polymer physics. Cornell university press; 1979.
32. Kalra V, Mendez S, Escobedo F, Joo YL. Coarse-grained molecular dynamics simulation on the placement of nanoparticles within symmetric diblock copolymers under shear flow. The Journal of chemical physics. 2008 Apr 28;128(16):164909.
33. Kalra V, Joo YL. Coarse-grained molecular dynamics study of block copolymer/nanoparticle composites under elongational flow. The Journal of chemical physics. 2009 Dec 7;131(21):214904.
34. Kalra V, Escobedo F, Joo YL. Effect of shear on nanoparticle dispersion in polymer melts: A coarse-grained molecular dynamics study. The Journal of chemical physics. 2010 Jan

14;132(2):024901.

35. Rolfe BA, Chun J, Joo YL. Dynamics of micelle–nanoparticle systems undergoing shear: a coarse-grained molecular dynamics approach. *Soft Matter*. 2013;9(43):10294-305.
36. Shebert GL, Joo YL. Effect of elongational flow on immiscible polymer blend/nanoparticle composites: a molecular dynamics study. *Soft Matter*. 2016;12(28):6132-40.
37. Cheng JY, Rettner CT, Sanders DP, Kim HC, Hinsberg WD. Dense self-assembly on sparse chemical patterns: Rectifying and multiplying lithographic patterns using block copolymers. *Advanced Materials*. 2008 Aug 18;20(16):3155-8.
38. Bitai I, Yang JK, Jung YS, Ross CA, Thomas EL, Berggren KK. Graphoepitaxy of self-assembled block copolymers on two-dimensional periodic patterned templates. *Science*. 2008 Aug 15;321(5891):939-43.
39. Cheng JY, Ross CA, Thomas EL, Smith HI, Vancso GJ. Fabrication of nanostructures with long-range order using block copolymer lithography. *Applied physics letters*. 2002 Nov 4;81(19):3657-9.
40. FEOL (Front End of Line: substrate process, the first half of wafer processing)9. Contact holes [Internet]. *Smart Manufacturing Solutions* : Fujitsu Ireland. [cited 2019Jan19]. Available from: <http://www.fujitsu.com/jp/group/mifs/en/resources/news/library/tech->

[intro/process/contact.html](#)

41. Liu CC, Han E, Onses MS, Thode CJ, Ji S, Gopalan P, Nealey PF. Fabrication of lithographically defined chemically patterned polymer brushes and mats. *Macromolecules*. 2011 Mar 18;44(7):1876-85.
42. Liu CC, Ramírez-Hernández A, Han E, Craig GS, Tada Y, Yoshida H, Kang H, Ji S, Gopalan P, De Pablo JJ, Nealey PF. Chemical patterns for directed self-assembly of lamellae-forming block copolymers with density multiplication of features. *Macromolecules*. 2013 Feb 11;46(4):1415-24.
43. Gronheid R, Nealey P, editors. *Directed Self-assembly of Block Co-polymers for Nano-manufacturing*. Woodhead Publishing; 2015 Jul 17.
44. Sarrazin A, Posseme N, Pimenta-Barros P, Barnola S, Gharbi A, Argoud M, Tiron R, Cardinaud C. PMMA removal selectivity to polystyrene using dry etch approach. *Journal of Vacuum Science & Technology B, Nanotechnology and Microelectronics: Materials, Processing, Measurement, and Phenomena*. 2016 Nov;34(6):061802.
45. Baravelli E, Dixit A, Rooyackers R, Jurczak M, Speciale N, De Meyer K. Impact of line-edge roughness on FinFET matching performance. *IEEE Transactions on Electron Devices*. 2007 Sep;54(9):2466-74.

46. Leung G, Lai L, Gupta P, Chui CO. Device-and circuit-level variability caused by line edge roughness for sub-32-nm FinFET technologies. IEEE Transactions on Electron Devices.

2012 Aug;59(8):2057-63.

47. Chris Mack. Stochastic and the Phenomenon of Line-Edge 2017 2017 Feb 27. Tutorial talk at the SPIE Advanced Lithography Symposium, San Jose, California.

CHAPTER 2

DESIGNING AN ORDERED TEMPLATE OF CYLINDRICAL ARRAYS BASED ON A SIMPLE FLAT PLATE CONFINEMENT OF BLOCK COPOLYMERS: A COARSE-GRAINED MOLECULAR DYNAMICS STUDY

2.1 INTRODUCTION

In this work, we study the self-assembly of asymmetric di-block copolymers of volume fractions close to 0.3 under three different confinements using a coarse-grained molecular dynamics (CGMD) framework. Firstly, we study the effect of topography imposed by a simple flat plate confinement. Two plate separation distances were chosen corresponding to two different confinement effects experienced by the BCP. Smaller the separation, higher was the entropic penalty imposed by the system. Trials were performed by varying the polymer and surface properties to explore the various morphologies formed by the flat plate template. The results obtained by this template were used to design the second geometry using ordered silica pillars to form a template of cylindrical BCP arrays.

The two plate separations employed in the flat plate template were used as the least and highest separation of the adjacent pillars along the line joining its centers. (Figure 2.1) Along with the confinement effect, this geometry imposes an added complexity caused by the curvature of the pillars. Thirdly, the effect of addition of a bottom substrate on which the pillars rest was studied. The substrate offers an additional confinement effect in the direction perpendicular to that imposed by the pillars, thus further constricting the BCP movement.

As the main application of these templates is to form ‘contact-hole’ lithographic patterns, we desire to form minor phase cylinders with no micro-bridging between the minor phase domains, with uniformity across the radial and axial directions. The uniformly formed, ordered minor phase cylinders has ease in post processing. The pattern formed by the system is used as a polymer-mask with the major phase acting as a photo-resist while the minor phase is etched away forming the hollow cylinder electron pathway used to guide electrons. The guided pattern forms the primary matrix to be used in the manufacture of transistors and other micro-electronic devices. Defect like micro-bridging, or disclination and dislocation defects observed in line-spaced patterns leads to broken symmetry and cannot be used for further post-processing. Thermodynamically, the micro-bridged state is not considered the least free energy state of the system but a kinetically trapped meta-stable state. If one waits for infinite time, the defects can be annihilated, but this luxury is not available in an industrial setting. It is understandable that the manufacturer seeks to achieve a defect free optimal structure with least annealing time for high throughput and economic benefits. Simulations are thus especially useful to elucidate the formation of these meta-stable state and the parameters that increases the rate of the self-assembly. The scope of this study is limited to the pattern formation and understanding the fundamental aspects of the BCP self-assembly.

Apart from a few sparse Molecular Dynamics studies^{1,2} of BCP self-assembly, most of the simulation work studying BCP morphology formation for nano-lithographic applications use a self-consistent field theory³ or a field-theoretic framework⁴. Huinink et. Al⁵ employ a dynamic density functional theory approach to study the effect selective surfaces have on the morphology of asymmetric cylinder forming di-BCPs. The authors show that the interaction strength of the surfaces with the BCPs and the film thickness greatly affect the morphology as well as the stability

of the corresponding phases. In an earlier publication⁶, the same authors have used a similar approach to generate comprehensive phase diagrams for thin films that predicted phases such as parallel cylinders, perpendicular cylinders, parallel lamellae and parallel perforated lamellae for a BCP that forms hexagonally packed cylinder in the bulk. In another recent work by Nikoubashman *et al.*⁷, a dissipative particle dynamics (DPD) framework is used to effectively study the self-assembly of cylinder forming PS-PHMA like BCP thin films by varying parameters like block compositions, film thickness among others with close agreements to experiments. Nikoubashman and co-workers⁸ have also studied directed self-assembly of cylinder forming PS-PHMA using theoretically informed coarse-grained simulations technique⁹ in conjunction with DPD. The domains in the BCP thin-films were aligned using shear and thus the hydrodynamic interactions considered by the DPD framework was important for accurate comparison with experiments.

There has also been some early theoretical work carried out by Turner¹⁰ and later followed by Walton and co-workers¹¹ studying the morphology formed by lamellae forming symmetric BCP confined between two biased infinite plates. The plate separations were kept at either odd or even multiples of the bulk equilibrium lamellar period and prediction via free energy models were made for ‘horizontal symmetric’ or horizontal anti-symmetric’ morphologies. Other works about asymmetric cylinder forming block copolymers confined between flat surfaces include a comprehensive study by Wang *et al.*¹² using Monte Carlo simulations. The authors study the effect of various surface-BCP interactions for different plate separations as a function of the pitch of the bulk hexagonal cylinders for the BCP. The morphologies observed include perpendicular cylinders, parallel cylinders, mixed cylinders as well as non-cylindrical structures like lamellae and perforated lamellae (for minor phase selective surfaces).

The current study uses large scale molecular dynamics that matches the device dimensions adopting simple length scale arguments from flat plate confinement studies to predict the more intricate geometry formation of ordered pillars template.

2.2 MODEL AND METHODS

2.2.1 Model details

The polymer studied in this paper is an asymmetric A - B type di-block copolymer with A being the minor phase. The most popular BCP employed in DSA is Polystyrene-block-polymethylmethacrylate (PS- b -PMMA) and the adopted model takes this into consideration. In a coarse-grained framework, the typical strategy used is reducing the degrees of freedom with some loss in microscopic structural characteristics of the system without restricting the length scale probed. The methodology followed for coarse graining in this work is similar to the one studied by Chremos *et al.*¹³ The block copolymers are modeled as bead-spring particles and the constituent Kuhn segments are mapped to a typical Lennard-Jones particle. The monomer size (σ) is considered to be 1.8 nm which is the theoretical Kuhn length of styrene. This corresponds to 5.4 molecules of styrene in 1 coarse grained styrene bead. If we apply the constraint that the volume occupied by both type of beads to be equal, it would correspond 5.8 molecules of methyl methacrylate (MMA) in a coarse-grained bead. This approximation is justified as the Kuhn lengths of MMA and styrene are quite alike. Similar coarse-graining can be applied to other BCP pairs by equating the coarse-grained molar volume. The extent of coarsening of the methodology allows to explore length scales close to the actual device dimensions without compromising on the box size. As the size of each monomer bead is comparable to the Kuhn segment, the loss in degrees of freedom due to the angles and dihedrals is minimum. A variety of chain lengths from $N10$ to $N120$ have been studied depending on the confinement geometry. The volume fraction of the minor phase is close to 0.3 (varies from 0.25 to 0.35).

Within a polymer chain, the neighboring atoms are joined by a bond which is essentially a bead-spring arrangement. The spring constant, K was considered to be $30 \epsilon \sigma^{-2}$ while the maximum extensibility, R_{max} was fixed at 1.5σ ¹⁴.

$$U_{fene}(r) = -\frac{1}{2} K R_{max}^2 \ln \left[1 - \left(\frac{r}{R_{max}} \right)^2 \right] \quad \text{equation-2.1}$$

Monomers of each block in the polymeric chain are given the purely repulsive Weeks-Chandler-Anderson (WCA) potential which account for the excluded volume interactions¹⁵. This is essentially a shifted 12-6 Lennard-Jones force field which is terminated at $2^{\frac{1}{6}} \sigma$, truncating its attractive portion.

$$U_{rep}(r) = \begin{cases} 4\epsilon \left[\left(\frac{\sigma}{r} \right)^{12} - \left(\frac{\sigma}{r} \right)^6 \right], & r \leq 2^{\frac{1}{6}} \sigma \\ 0, & r > 2^{\frac{1}{6}} \sigma \end{cases} \quad \text{equation-2.2}$$

Here U_{rep} is the repulsive potential, r , is the separation between the centers of mass of two beads and ϵ is the Lennard-Jones interaction parameter.

The like monomer groups are provided with a modified form of 12-6 Lennard-Jones potential, U_{att} with a GROMACS style correction for the tail such that the energy smoothens out to zero at the cutoff radius (r_c). The tail correction, S_{LJ} is applied for $r_1 = 1.9149 \sigma$ to the cut-off radius r_c of 2.5σ where it becomes zero.

$$U_{att}(r) = \begin{cases} 4\epsilon \left[\left(\frac{\sigma}{r} \right)^{12} - \left(\frac{\sigma}{r} \right)^6 \right] + S_{LJ}(r) & r < r_c \\ 0, & r > r_c \end{cases} \quad \text{equation-2.3}$$

$$S_{LJ}(r) = \begin{cases} C, & r < r_1 \\ \frac{a}{3}(r - r_1)^3 + \frac{b}{4}(r - r_1)^4 + C, & r_1 < r < r_c \end{cases}$$

Surface beads that are attractive to polymer beads have pair interactions described as $U_{att}(r)$ while the repulsive interactions between the surfaces and the polymer follows the $U_{rep}(r)$ force field. The default interaction of the surfaces is attractive to the minor phase and repulsive to the major phase. The surface-polymer interaction strength ϵ_{S-A} and ϵ_{S-B} is a variable with a default energy value of $1.0 k_b T$. The distinct types of interactions have been summarized in Table 2.1.

Table 2.1 : Types of long-range pairwise potential interactions

Pair interactions	Explanation of pair potential
B-B ; A-B ; Surface-A	Lennard-Jones, Gromacs tail correction: $r = 1.9149\sigma$ to 2.5σ ; cutoff at 2.5σ
A-B ; Surface-B	Weeks-Chandler-Anderson; cutoff at $2^{1/6}\sigma$
Surface bead-Surface bead	Frozen state – no interactions

2.2.2 Thermostat

The thermostat used in this study is dissipative particle dynamics thermostat. The technique was first introduced by Hoogerbrugge and Koelman essentially introducing hydrodynamic behavior in meso-scale simulations^{16, 17}. As the thermostat effectively conserves momentum (local and global) and offers Galilean invariance, it has been popularly used to study soft matter MD systems¹⁸. Soddemann, *et al.*¹⁹ has systematically studied the effectiveness of the DPD thermostat highlighting its universality with respect to the pair potential employed (in particular repulsive LJ interactions) and accurate representation of the hydrodynamic correlations among others.

When using a DPD thermostat, the pairwise interaction is equal to the non-conservative portion of a DPD force field. The force on bead i due to bead j is given as a sum of the following terms:

$$\vec{f} = (F^D + F^R)\vec{r}_{ij} \quad r < r_c$$

$$F^D = -\gamma\omega^2(r)(\vec{r}_{ij} \cdot \vec{v}_{ij})$$

$$F^R = s\omega(r)\alpha(\Delta t)^{-\frac{1}{2}}$$

$$\omega(r) = 1 - \frac{r}{r_c}$$

$$s = \sqrt{2k_b T \gamma} \quad \text{- equations (2.4-2.8)}$$

Here F^D is the dissipative force (acts as heat source) and F^R is the random force (acts as a heat drain), r_{ij} is a unit vector joining bead i and bead j , v_{ij} is the vector difference in velocities of the two beads, T is the temperature parameter in simulation and k_b is the Boltzmann constant. α is a random number generated from a space of Gaussian numbers with mean at zero and variance (s) equal to unity. Δt is the time step size associated with each iteration. $\omega(r)$ is a weighing function whose value is 1 for all $r < r_c$ (cut off radius) or zero otherwise.

2.2.3 Confinement Templates

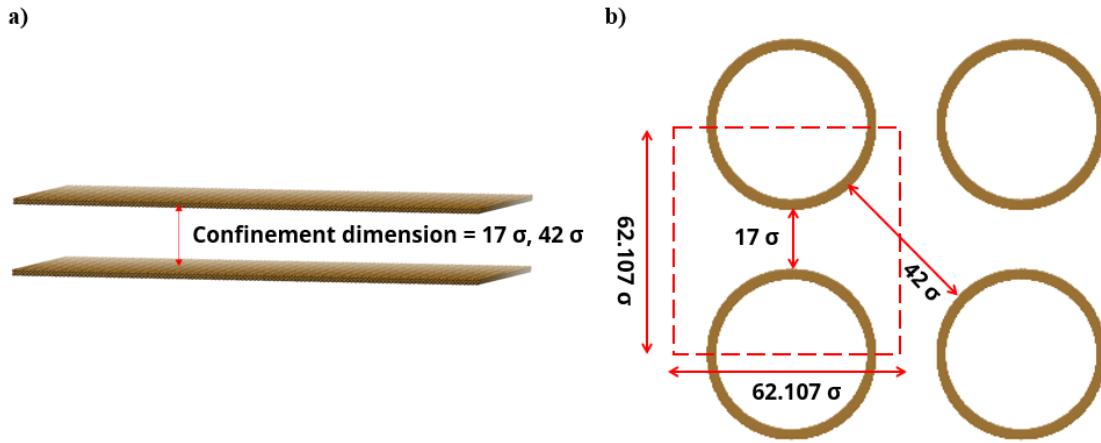


Figure 2.1: Geometric templates that confine the BCP. a) Flat plate geometry. The dimensions of the plates are $120\sigma \times 120\sigma \times 3\sigma$. b) xy projections of the simulation box for the pillars geometry. The height of the pillars is 62.107σ . A bottom substrate like a) adds an additional confinement in the third type of geometry.

As mentioned in the introduction, the BCP morphology formed is studied under three types of confinement. In the first template the BCP chains are confined between two flat plates (Figure 2.1a). Both the bottom and top substrate are biased attractive to the minor phase. The geometry has no topological features. The plate separation is fixed at 17σ (~ 30 nm) and 42σ (75.6 nm) corresponding to two levels of confinements experienced by the BCP. For the higher plate separation, we expect more fraction of the BCP to be present in the bulk as compared to the lower plate separation. The simulation box is periodic in x y direction and is fixed in the z direction (confinement dimension). The trials have probed long chain BCPs and for such chain lengths employed it is essential that the box size is sufficiently large in the non-confined periodic dimension. Using smaller box sizes, a BCP bead from one end of a chain that escapes from one side of a periodic boundary could interact with the beads from the other end of the same chain leading to erroneous results. As the longest chain probed are $N120$ for 17σ confinement and $N80$ for 42σ confinement, the default box dimension in the periodic x y direction was chosen to be $120\sigma \times 120\sigma$ and $100\sigma \times 100\sigma$ for 17σ and 42σ , respectively to ensure that one end of a fully stretched

chain does not interact with the other end owing to the limitations of the box size in the periodic conditions.

The second geometric template probed is that of ordered pillars which serve as a topographic feature and direct the BCP (Figure 2.1b). The BCP is confined in the region between the pillars in a simulation box periodic in all directions. Such pillars are generally made of Silica which may or may not be chemically treated. We assume that the minor phase, *A* has higher affinity towards the pillars. An experimental analogy being that of PMMA, that has higher affinity towards untreated as compared to PS. Hence justifiably, we employ an attractive form of LJ potentials (Eq. 2.3) for the pillar-minor phase interaction and a WCA potential (Eq. 2.2) for pillar-major phase interactions. Silica being a refractory material does not show any form of deformation at the prevailing experimental annealing conditions. The default dimensions chosen for the pillars are 44.44σ (80 nm) in diameter and about 62.107σ (~112 nm) in height with the surface bead size being the same as the BCP bead size ($\sigma = 1.8$ nm). The pillar diameter and pitch chosen in this study are quite similar to what one would encounter in the micro-electronics industry and well within the lithographic manufacturing capabilities to generate the pillars. The results obtained from the flat plate geometry studies have been used to design this lithographic template in a bid to form periodic arrays of minor phase cylinders. Accordingly, to have close resemblance to the flat plate confinement trials, the least and highest radial separation between adjacent pillars along the line joining the centers of the pillars has been fixed at 17σ and 42σ , respectively. The confinement effect experienced by the polymer will be governed by its location with respect to the least and highest radial pillar separation lengths as well as its collective domain size. The domain size can be related to the radius of gyration (R_g) of the polymer, analytically calculated as $\langle R_g^2 \rangle =$

$b^2N/6$ for an ideal homopolymer chain²⁰. Here b is the Kuhn length which is equal to our monomer bead size of 1σ (1.8 nm) and N is the chain length. Thus, polymers with higher chain lengths situated close to the least radial pillar separation are expected to experience higher confinement effects as compared to lower chain lengths situated by the highest radial pillar separations.

Along with the curvature-confinement effects of the pillars, an added complexity of a bottom substrate is introduced in the third geometric template analyzed. This bottom substrate can be thought of as a silicon base on which the silica pillars rest. Silicon, like silica has higher affinity towards PMMA and similar surface-BCP interaction are employed for the bottom substrate and pillars. An identical but neutral substrate bounds the box in the upper z direction. The box for this case is periodic in $x y$ direction and fixed in the z direction. All surfaces are three layers thick with a thickness of 3σ (5.4 nm). The surface beads are hexagonally closed packed with the separation between the centers of any two beads in the same layer equal to the monomer bead size σ . The comparison of the parameters used for different geometries has been made in Table 2.2.

2.2.4 Simulation Details

The initial co-ordinates of the BCP, substrate, and pillar beads were generated using MATLAB® such that the overall BCP site density is maintained 0.85 in the confined volume. This initial state of the system is highly biased with many of the beads in close proximity to one another. To rectify this bias, the system was first warmed with soft cosine potentials. This was followed by an equilibration run using non-selective Lenard-Jones potential for all pairwise interactions according to equation 2.3 for at least 1 million steps. The interaction between the pillar beads and substrate beads were frozen and set to zero to increase the computational efficiency. This ensures that the non-BCP beads remain stationary. The conditions of constant number of beads and simulation box size and the employed DPD thermostat produces an NVT ensemble. Thereafter, selective pairwise interactions were switched on and the simulations are run for sufficiently long time such that unit variables like pressure, potential energy, total energy remained constant within the fluctuation limits. For some trials that showed micro-bridging defects (kinetically trapped), the simulations had to be run for considerably higher amount of time to annihilate the defects. The comparison of the morphology for various parameters for each confinement is either made at the equilibrium state or for the same number of time-step providing useful kinetic evolution data. A timestep of 0.01 was employed for trials. These simulations have been carried out using LAMMPS²¹⁻²² and the morphology was visualized with VMD²³. The χ_N values have been calculated using a modified form of the equation adopted by Horsch, *et al*²⁴ as the chain lengths employed in this study is significantly higher as compared to Horsch *et. al*'s work.

Table 2.2: Parameters for the confinement studies

Simulation Parameter	Flat plate trails (17 σ confinement)	Flat plate trails (42 σ confinement)	Pillars template (no substrate)	Pillars template (with substrate)
Site density	0.85	0.85	0.85	0.85
Bead diameter (surface, BCP)	1 σ = 1.8 nm	1 σ = 1.8 nm	1 σ = 1.8 nm	1 σ = 1.8 nm
Polymer aspect ratio, N	10, 20, 40, 60, 80, 120	10, 20, 40, 60, 80	10, 20, 30, 40, 60	20, 40, 60
Minor phase Volume fraction	0.30, 0.35	0.30, 0.35	0.25, 0.30, 0.35	0.25, 0.30, 0.35
Temperature	1.22	1.22	1.22	1.22
Box size	$120\sigma \times 120\sigma \times 20.5\sigma$	$100\sigma \times 100\sigma \times 45.5\sigma$	$62.107\sigma \times 62.107\sigma \times 62.107\sigma$	$62.107\sigma \times 62.107\sigma \times 64.107\sigma$
Total number of beads	295682	418002	168920	190926
Number of BCP beads	208080	357000	118080	116400
Timestep	0.01	0.01	0.01	0.01

2.3 RESULTS AND DISCUSSIONS

2.3.1 Self-assembly under periodic conditions

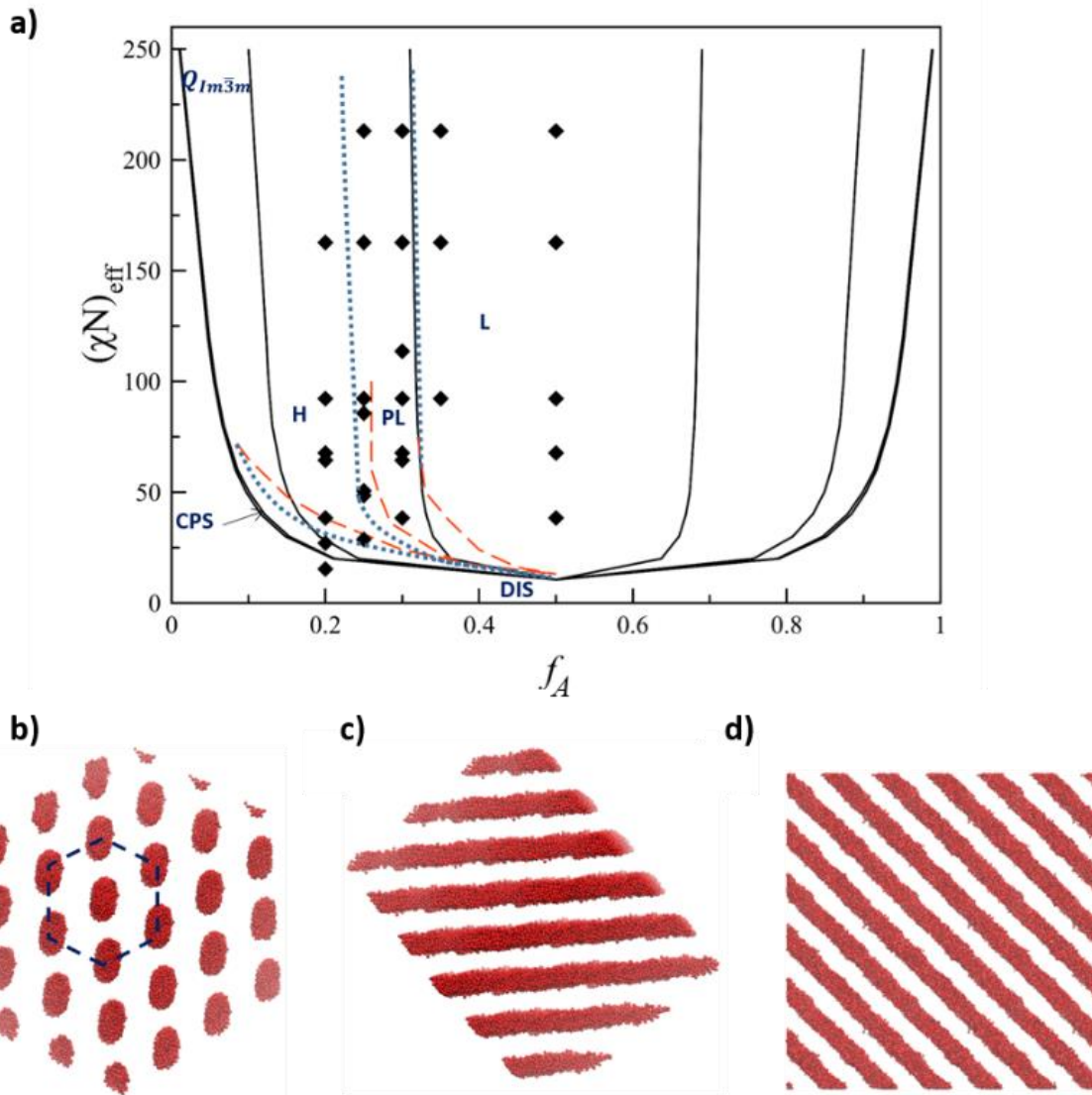


Figure 2.2: a) Phase diagram for a A - B type block copolymer. Black solid lines are the reconstructed phase-diagram as predicted by Bates and Matsen. Red dash lines represent the reconstructed phase boundaries by BD and MD work by Horsch *et al.* Blue dotted lines represent the predicted phase boundaries in this study with the current study. The black diamonds are the simulated points. Some sample phases observed include a) hexagonally packed cylinders b) perforated lamellae and c) lamellae

To authenticate the model employed, we first studied the morphology formed by the BCP under periodic conditions. The results obtained are consolidated in the bulk $(\chi N)_{eff}$ vs f_A phase diagram

in figure 2.2a. Matsen and Bates²⁵ has demonstrated the dependency of these factors on the type of BCP morphology formed for infinite length polymer chains (black lines, figure 2.2a). Phases observed in this study included L-lamellar, H-hexagonal cylinders, $Q_{Ia\bar{3}d}$ (bi-continuous $Ia\bar{3}d$ cubic), $Q_{Im\bar{3}m}$ (bcc spheres), CPS - close packed spheres and disordered (formed below $(\chi N)^{ODT}$). These BCP morphologies have subsequently been predicted using molecular dynamics (MD) and hard Brownian dynamics (BD) by Horsch *et al*²⁴. (red dash lines, figure 2.2a) showing some deviation in the predicted phase boundaries as compared to the earlier work which can be attributed to fluctuation effects. We have tested our model for a wide variety of chain lengths from $5N$ to $60N$, at two different temperatures (0.695, 1.22) to get χN values ranging from below the $(\chi N)^{ODT}$ to > 200 . Some of these values estimated correspond to high- χ BCPs that has gained considerable interests recently owing to their high degree of phase separation, low interfacial AB block widths and thus lower line-edge roughness values²⁶. Horsch *et al*, employ a R_g scaling of $R_g \sim N^\nu$ to estimate the MD χN values, where the scaling parameter ν was estimated to be 0.69 for $N5$ to $N10$. For the higher chain lengths employed in this study we have found the scaling parameter to be 0.63 for both perforated lamellae forming $f_A = 0.30$ and lamellae forming $f_A = 0.50$. Chain lengths higher than $N60$ required a much bigger simulation box to prevent box size effects, that would be computationally expensive. Using the new R_g scaling, the following modified form of $(\chi N)_{eff}$ correlation has been derived and used to generate the phase diagram in figure 2.2a (blue dotted lines). More details can be found in the supplementary information document.

$$(\chi N)_{eff} \approx \frac{[(9.48 \pm 0.11)^E / kT - 0.09]N}{1 + 3.9N^{-0.59}} \quad \text{- equation 2.9}$$

For the chain lengths attempted, the phase diagram is in good agreement to the one predicted by Horsh *et al.* For the three minor phase volume fractions of interest, away from the ODT line, 0.3 showed PL phase for both the studies. Horsch *et al* do not have simulated points for $f_A = 0.35$, but the predicted phase boundaries show L morphology, in agreement with the current work especially for high χN values. The main distinction arises for $f_A = 0.25$ wherein Horsch *et. al* predicts a cylinder morphology while this study shows a PL morphology especially at higher chain lengths. The minor distinction may be because Horsch and co-authors predominantly use hard BD framework along with some MD trials to estimate the phase boundary while we only use CGMD for this work.

2.3.2 Flat Plate Study

Plate separation of 17σ

These trials have both the substrates attractive to the minor phase as defined in Eq. 2.3. The reaction co-ordinate chosen here is the degree of polymerization, N . The surface-BCP interaction potential strength, ϵ_{S-BCP} is 1.0. For volume fractions = 0.30 (figure 2.3), chain lengths $\leq N20$, shows a continuous minor phase three-domain sandwich structure with alternating continuous major phase domains in between the minor phases. Two of the minor phase layers coat the surface while the third domain is seen formed in the bulk central region. Multiple layers of minor phase are present in the domains that coat the surface. The concentration plots show three peaks per surface, with the peak closest to the surface having the highest concentration. It is also noted that $N10$ has a higher concentration in the central domain as compared to $N20$. The frustration experienced by $N10$ is lower than that experienced by $N20$ for the confinement of 17σ . Thus, due to the lower entropic penalty imposed, a fraction of the minor phase beads self-assembles in the

central domains. For $N20$, the entropic penalty is higher than that experienced by $N10$ but not high enough to eliminate the central minor phase domain. It is also important to note that the middle domain layer although is thicker for $N20$, perforations are observed in the lamellae causing it to have a lower concentration as compared to $N10$ which is agreement to its bulk behavior. Beyond $N20$, the morphology formed is a continuous two-domain sandwich structure. Higher chain lengths ($N20 \leq$) form thicker coatings on the surfaces and all the minor phase beads are utilized in coating the surfaces. These trials show that the BCP has a critical molecular weight to form a morphology with the least number of continuous micro-domains (two) for a given confinement. Such multi-layered lamellar formation for BCPs confined between two surfaces attractive to the minor phase has been reported in other SCFT and Monte-Carlo studies.^{3,5,6,12}

More insights are gained by the polymer chain statistics (table 3). The chains show a lower value for R_g in the confinement as compared to bulk. This value significantly deviates from its bulk R_g as the chain length increases, thus indicating more constriction for higher N . It is also observed that the z component of the end-to-end vector, $\langle R_z \rangle$ has a higher magnitude than x y signifying that the chains prefer to align itself parallel to the confinement dimension. For lower N , $\langle R_z \rangle$ increases with N but beyond the transition from $N20$ - $N40$ the value remains more or less the same with the increase in size being compensated by higher $\langle R_x \rangle$ and $\langle R_y \rangle$.

If we increase the volume fractions to 0.35, the transition from the continuous three domain sandwich to a two-domain structure also occurs at $N20$ - $N40$, but the middle minor phase domain for $N20$ has a much lower concentration as compared to the lower volume fraction trials (refer S.I). As these trials have a lower major phase concentration, the effective screening effect caused by the major phase shielding the bulk minor phase domains from the surface domains is lower. Hence

the middle domains get redistributed among the two surface domains leading to the observed geometry.

The next set of trials performed were to study the effect of the strength of interaction potential of the surfaces with the BCPs for a finite annealing time of 2.5 million steps. Experimentally, this can be thought of as treating the surfaces with specific reactive ligands that differ in their interaction with the BCP phases. The strength of these interactions can be varied by the type of the ligands as well as by their surface density. The first set of trials were performed for $N20$ and $N40$ – the chain length transition at minor phase volume fraction 0.3. Figure 2.4c shows the surface-polymer interaction phase space, ϵ_{S-B} and ϵ_{S-A} for $N20$. While trials for $N40$ showed only three-domain structure irrespective of the surface-polymer interaction strengths for the values attempted, $N20$ showed a strong dependence on ϵ_{S-B} and ϵ_{S-A} .

Table 2.3: Polymer chain statistics for 17σ confinement. $\langle R_x \rangle$, $\langle R_y \rangle$, $\langle R_z \rangle$ are the average $x y z$ component of the end-to-end vector for the chains. $\langle R \rangle$ is the average end-to-end vector. $\langle R_g \rangle$ is the radius of gyration

Chain length	$\langle R_x \rangle$	$\langle R_y \rangle$	$\langle R_z \rangle$	$\langle R \rangle$	$\langle R_g \rangle$	$\langle R_g \rangle_{\text{bulk}}$
$N10$	1.50	1.49	3.13	4.12	1.65	1.74
$N20$	2.64	2.63	4.00	6.25	2.53	2.69
$N40$	3.54	3.54	6.13	8.70	3.63	4.17
$N60$	4.58	4.51	6.30	10.04	4.30	5.38
$N80$	5.34	5.34	6.47	11.21	4.84	6.45
$N120$	6.16	6.55	6.82	13.09	5.75	8.33

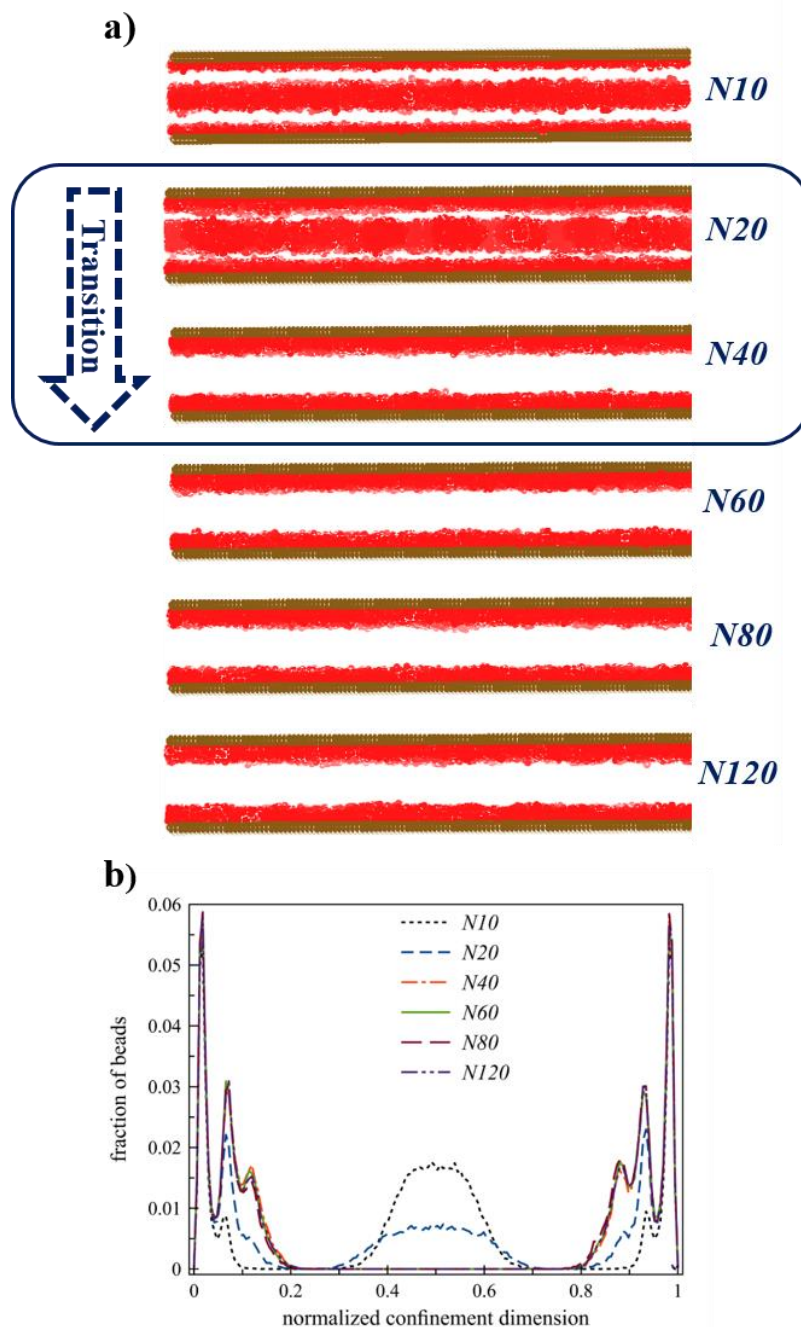


Figure 2.3 : a) Morphology formed for flat plate – 17σ confinement trials at minor phase volume fraction of 0.3. A transition from three-domain structure to a two-domain structure is observed at *N20*-*N40*. b) Concentration plots for a). Note: Only minor phase of the BCP is seen, major phase has been hidden for clarity in a).

For $\epsilon_{S-A} > 0.5$, a three-domain structure was formed for the values of ϵ_{S-B} attempted. For stronger surface-*A* interactions, we expect a smoother coating on the surfaces. *B* covalently bonded to the coated minor phase in turn is able to screen the *A* from the bulk, thus restricting it to the middle

region forming the continuous three domain morphology. For $\epsilon_{S-A} \leq 0.5$, sufficiently high values of ϵ_{S-B} form a two-domain structure. Lower values of ϵ_{S-A} lead to poorer coating, thus for effective screening of the bulk minor phase, the major phase covalently bonded to the surface requires a higher repulsive potential. If this repulsive potential is not high enough, anomalies in the form micro-bridging and diminutive middle domain (blob) are observed.

The significance of the minor phase coating and the screening offered by major phase is further strengthened by the trials seen in Figure 2.4. Figure 2.4a have trials performed at a constant, relatively low ϵ_{S-A} value of 0.1, while ϵ_{S-B} is varied. As the surface-*B* interaction strengths is increased from 0.9 to 1.5, the micro-bridging between the two surface minor phase domains is reduced. Stronger repulsion between the surface and *B* that is covalently bonded with the surface *A* leads to disruption of the micro-bridges as more *B* is moved to the bulk. It is noteworthy here that the micro-bridge morphology is not the least free energy state of the system. Since the morphology comparison is at the same time, the observation sheds light on the effect of surface-BCP interaction strength on the kinetics of the BCP self-assembly. Figure 2.4b, show trials at constant ϵ_{S-B} value of 1.0 while the ϵ_{S-A} is varied. As stated earlier, higher ϵ_{S-A} values lead to smoother coating and in turn more effective *A* screening effect leading to a continuous middle minor phase domain. Hence increasing the ϵ_{S-A} values transitions the morphology from two-domain to three-domain structure.

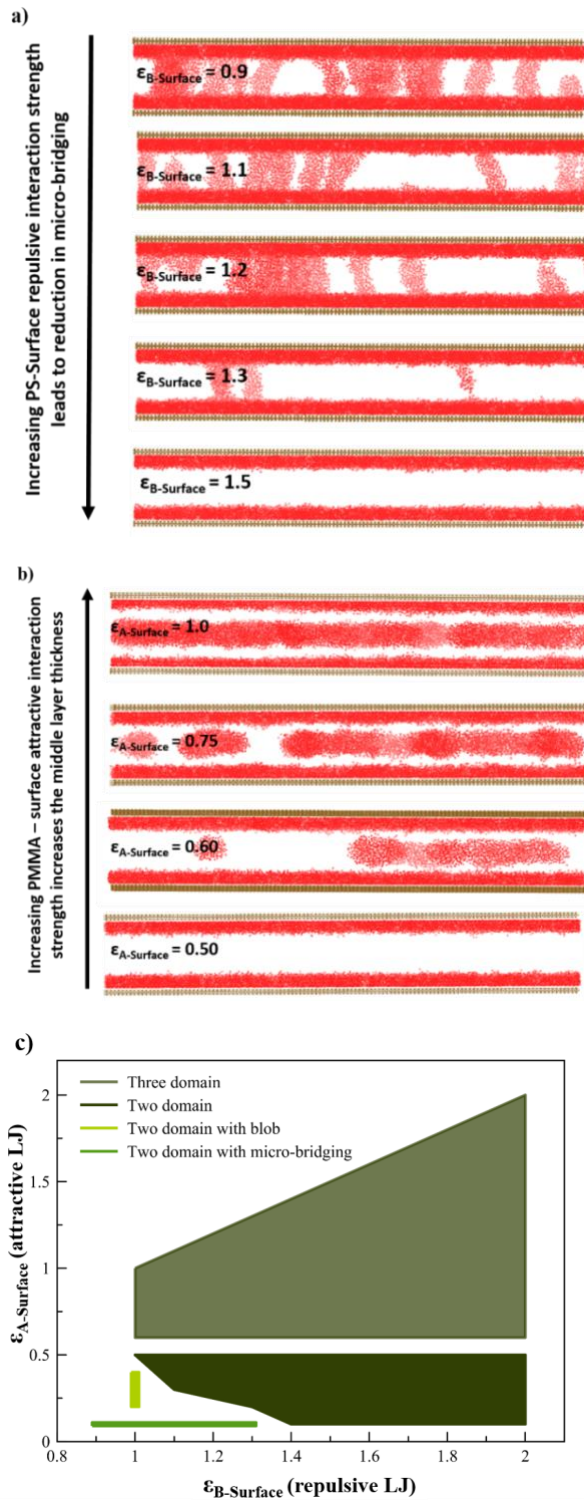


Figure 2.4: BCP-surface interaction pairwise potential phase-space for 17σ confinement after 2.5 million timesteps. a) ϵ_{S-B} at constant $\epsilon_{S-A} = 0.1$ and b) ϵ_{S-A} at constant $\epsilon_{S-B} = 1.0$. c) shows the phase-diagram at the current annealing time. A blob refers to a minuscule middle layer, not large enough to be termed a three-domain morphology.

Plate separation of 42 σ

These trials are similar to the 17 σ trials but with increased plate separation of 42 σ (~ 75 nm). As the plate separation in these trials is more, the confinement effect imposed by the surfaces is not as dominant. As observed in figure 2.5a, for lower chain lengths, *N10* and *N20* the thickness of the minor phase coating on the surface is much lesser as compared to the longer chain lengths – *N40* and *N60*. The number of continuous minor phase domains including those on the surfaces decreases from six for *N10* to four for *N20* and three each for *N40* and *N60*. We can thus consider *N40* to be the critical chain length, where we observe a transition from a multi-domain to a three-domain morphology. *N60* also form a three-domain structure but with some distinctive differences as evident from the concentration plots in figure 2.5b.

The middle domain is thicker for *N60* as compared to *N40* as observed in the wider spread for the concentration dome. This thicker domain has more perforation in order to conserve the total number of beads for the two chain lengths. The screening effect of the *B* phase is inadequate for the chain length *N60* leading to a certain degree of micro-bridging between the independent minor phase domains. The micro-bridging is kinetically trapped and was not annihilated even after annealing for 3 million steps more than the *N40* trials. Similar observations were made for *N80* trials (not seen in figure 2.5). It is expected that further increase in the BCP molecular weight will increase the surface BCP thickness as well as the middle domain thickness along with the perforations and micro-bridging. There will be a higher critical chain length at which the degree of confinement experienced will be strong enough for the middle domain to be absorbed by the surface domains. This hypothesis has been observed for trials performed for plate separation of 30 σ in which the average middle layer thickness for the three-domain morphology is reduced in

thickness from $N40$ to $N60$, and then to $N80$, eventually disappearing and forming a two-domain morphology for $N120$. The chain-statistics analysis (table 2.4) shows a lower value for R_g for all chain lengths as compared to its bulk values, but this reduction in values is not as stark as in the case of 17σ confinement. The higher z component of the end-to-end vector also shows a bias for the chains to align parallel to the confinement dimension.

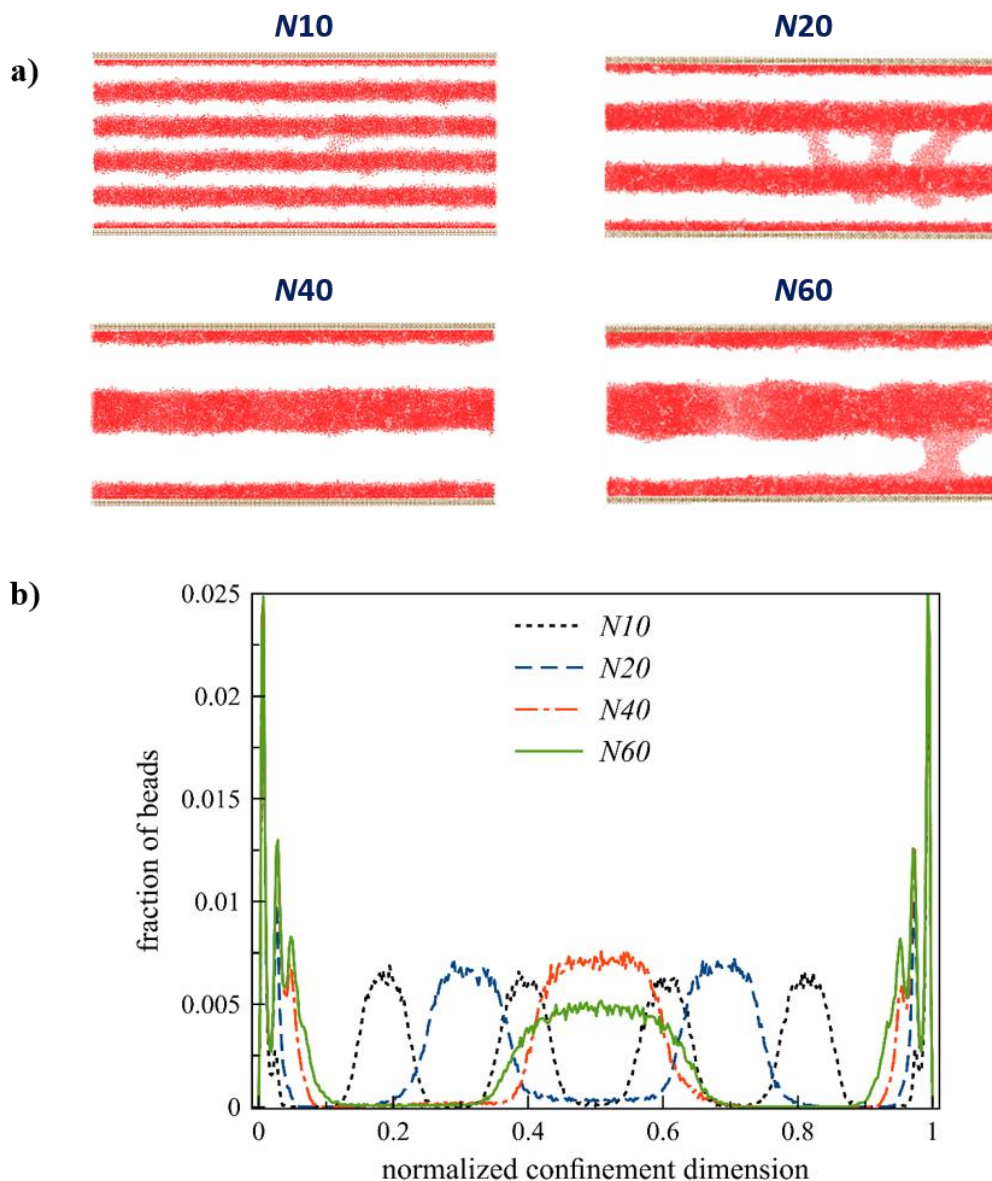


Figure 2.5: Morphology formed for flat plate – 42σ confinement trials at minor phase volume fraction of 0.3. The number of micro-domains reduces with increase in N . b) Concentration plot for a). Note: Major phase, PS has been hidden for clarity

Table 2.4: Polymer chain statistics for 42 σ confinement. $\langle R_x \rangle$, $\langle R_y \rangle$, $\langle R_z \rangle$ are the average $x y z$ component of the end-to-end vector for the chains. $\langle R \rangle$ is the average end-to-end vector. $\langle R_g \rangle$ is the radius of gyration

Chain length	$\langle R_x \rangle$	$\langle R_y \rangle$	$\langle R_z \rangle$	$\langle R \rangle$	$\langle R_g \rangle$	$\langle R_g \rangle_{\text{bulk}}$
N10	1.62	1.62	3.01	4.19	1.66	1.74
N20	2.34	2.35	5.35	6.84	2.67	2.69
N40	3.66	3.71	7.82	10.23	4.04	4.17
N60	5.60	5.11	7.43	12.06	4.86	5.38

2.3.3 Confinement using silica pillars with no substrate

One of the major findings of the previous geometry studied was that the morphology formed by the BCPs is dependent on the degree of polymerization N . This dependency can be accentuated in a confined system where the confinement dimensions are of the same order as the polymer chain length. There lies a critical chain length ($N40$) for which we see a transition from three-domain morphology to a two-domain morphology for the flat plate separation of 17 σ . Similarly, another transition from a multi-domain (> 3) structure to a three-domain structure was observed at the same critical chain length for the plate separation of 42 σ . For the length scale arguments to hold true, it was hypothesized that the ordered pillars template should also show a similar critical chain length transition as the BCP in this geometry is confined by surfaces separated between 17 σ (least separation, highest confinement) and 42 σ (highest separation, lowest confinement).

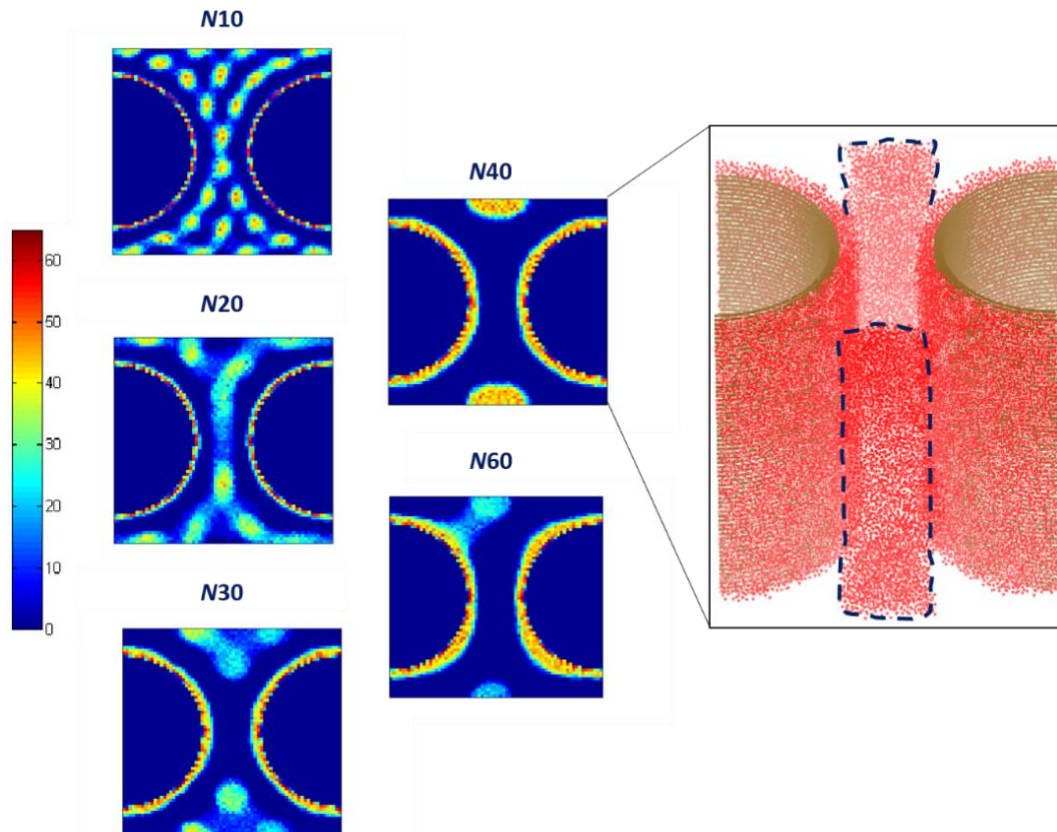


Figure 2.6: Minor phase density plots for BCP with a minor phase volume fraction of 0.3 under ordered pillars confinement. A part of the minor phase is seen deposited on the curved pillar surface while the rest remains in the bulk forming the characteristic morphology. The 3D representation of the minor phase pillars for $N40$ is also seen.

Effect of chain length and temperature

We employ chain lengths of $N10$, $N20$, $N30$, $N40$ and $N60$ and a minor phase volume fraction of 0.3. The pillars being attractive to the minor phase draw the minor phase beads to its surface. As seen in the density plots of the B phase (figure 2.6), an increase in the chain length, N leads to thicker deposition of the minor phase on the surfaces. $N10$ and $N20$ show bi-layer deposition of the beads while $N30$, $N40$, and $N60$ show a tri-layer deposition. The first layer that is in direct contact with the surfaces has the highest density which fades away for the layers following. For lower chain lengths ($N10$, $N20$), the morphology formed is a curved perforated lamella. The degree of perforation is higher for $N20$ as compared to $N10$. This can be attributed to the fact that longer

chains show more segregation, thus forming larger minor phase micro-domains. To accommodate for this local increase in the minor phase size, there is a depletion in the minor phase concentration in some places leading to the perforated morphology. As the deposition on the surfaces gets thicker (with N), the minor phase concentration in the bulk decreases. A transition is observed around $N30$ where the morphology shifts from curved perforated lamellae to cylinders. To minimize its free energy, with the available minor phase excluding the one on the surfaces, the BCP tries to micro-phase separate to minor phase cylinders that are about 20σ in diameter at these chain lengths. $N40$ is the optimum chain length for the parameters used in these set of trials wherein the fractional concentration of minor phase on the pillar surfaces is ideal (~ 0.75). The rest of the minor phase in the bulk form the cylinders and show long range order with complete formation along the pillar height that can be replicated to form the templated cylindrical arrays.

Increase in chain length from $N40$ to $N60$ leads to micro-bridging between the minor phase deposited on the surfaces and the bulk cylinders leading to defect formation for the annealing duration (2.5 million steps). For the confinement lengths in the template, the aspect ratios of $N60$ chains exceeds the highest separation of 42σ . The chains in this arrangement are frustrated and are unable to explore its entire energetic phase space. It is important to note that this micro-bridged state may not be its lowest free energy state, but a kinetically trapped meta-stable state. Free energy studies would be required to come to an appropriate conclusion in this regard.

Another crucial point here is that the minor phase A , consumed in coating the surfaces should not be regarded as a surplus of material. A on the surface is covalently bonded with the major phase, B . As B has an attractive interaction with other B beads, it attracts the major phase from the bulk.

This bulk *B* is covalently bonded with the bulk minor phase, *A*. As the bulk minor phase segregates to form the cylinders, a double screening layer of surface and bulk *B* chains is formed which not only drives the self-assembly but also prevent micro-bridging between the bulk and surface minor phase. The screening offered by the major phase is more effective for *N*40, but for *N*60 the higher entropic constraints overcome this screening.

Perturbation in BCP volume fraction

As observed in the last section, the amount of the minor phase beads on the surface and the bulk plays a crucial role in the type of morphology formed. A thicker surface deposition leads to scarcity of the minor phase in the bulk. A way to rectify this scarcity is to increase the minor phase concentration in a BCP chain. A shortcoming of increasing the volume fraction is the increase in probability for micro-bridging to be observed. Trials were performed at three degrees of polymerization corresponding to *N*20, *N*40 and *N*60 and minor phase volume fractions of 0.25, 0.30 and 0.35.

The trend of increased thickness of minor phase beads on the pillar surfaces with increase in *N* is seen for the three volume fractions attempted (figure 2.7). For lower chain lengths like *N*20, the same qualitative morphology of perforated curved lamellae is observed for the different volume fractions (figure 2.9 a, b and c). There is an increase in domain size (lesser number of individual domains) seen as the volume fraction is increased from 0.25 to 0.3 and 0.35. The main distinction in the three volume fractions and chain lengths attempted comes at the advent of the cylinder morphology. For volume fraction 0.25, the cylinder morphology is formed at *N*60 (figure 2.9 a-*N*60) as compared to *N*40 for volume fraction 0.3 (figure 2.9 b-*N*40) and 0.35 (figure 2.9 c-*N*40).

Higher volume fraction seems to favor micro-bridging between the minor phase beads on the pillar surface and the bulk for the prevailing annealing time of 2.5 million steps as evident in trials for volume fraction 0.3- $N60$ and volume fraction 0.35- $N40$, $N60$.

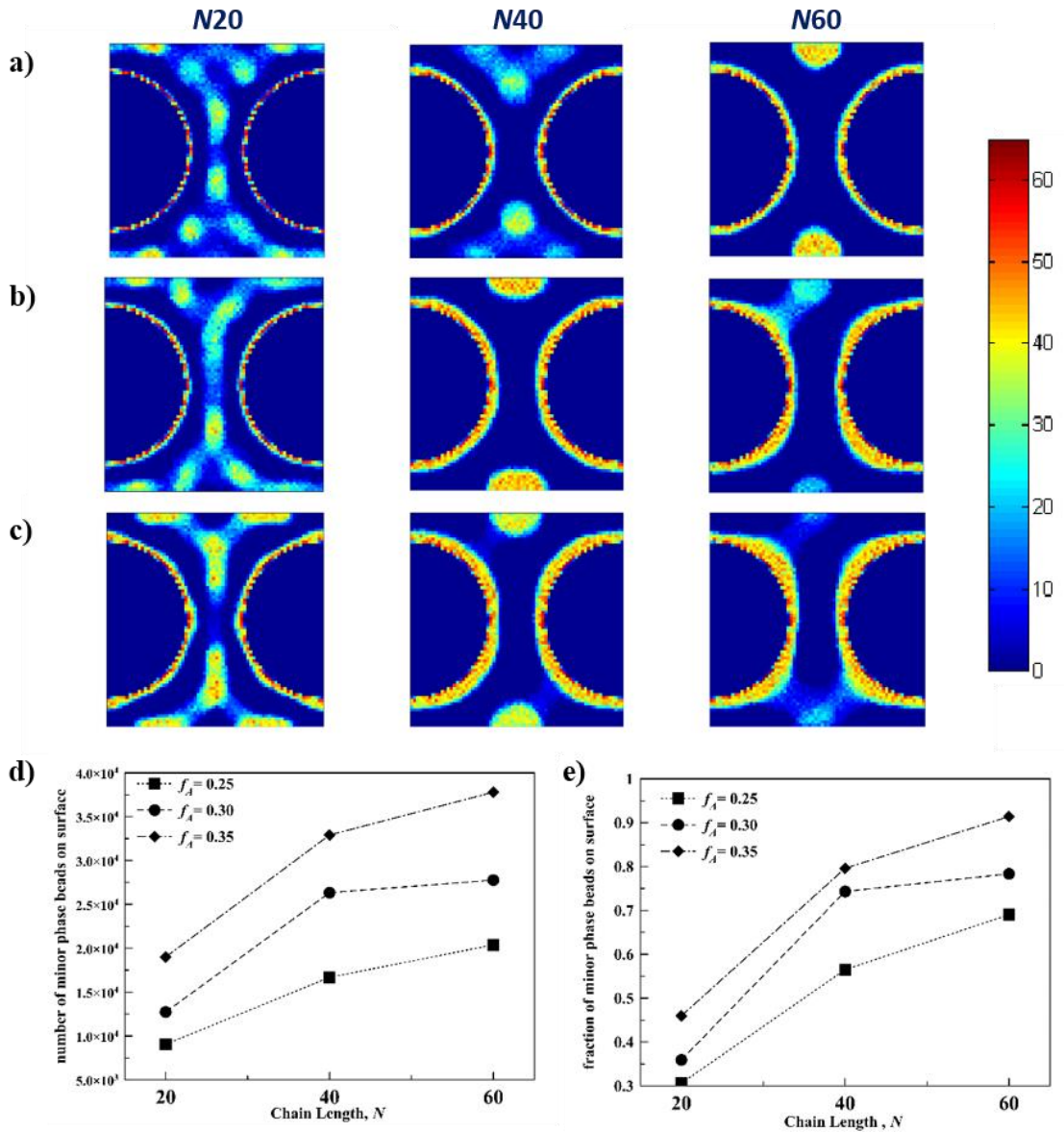


Figure 2.7: Minor phase density plots for three volume fractions: a) 0.25 b) 0.3 and c) 0.35. d) and e) show the effect of volume fraction on the fraction of the total minor phase beads and number of minor phase beads on the pillar surface respectively. The annealing time is 2.5 million timesteps.

These trials support the argument that the minor phase beads that are consumed to coat the pillar surfaces is replenished by adding more of the minor phase to the bulk (increasing minor phase volume fraction). This addition leads to a local surplus of the minor phase beads leading to micro-bridging at some points along the pillar height as the *B* phase screening effect is now inadequate for the prevailing concentrations. Another interesting observation made in these trials is the distribution of minor phase beads between the bulk and the surface for the volume fractions attempted. As the volume fraction increases from 0.25 to 0.30 and 0.35, the fraction of minor phase that prefers to coat the surfaces increases. Consequently, for the same chain lengths, increasing the minor phase volume fraction will favor lesser amount of minor phase in the bulk. Figure 2.9e also show that for a proportional increase in the number of minor phase beads from volume fraction 0.30 to 0.35 there is a disproportionate increase in the fraction of the minor phase beads that coat the surface for the three chain lengths. Our results show that about three quarters of the polymers is needed to coat the surface to form uniform cylinders ($\sim 0.70 - VF 0.25, N60$ and $\sim 0.78 - VF30, N40$). This knowledge can prove to be quite essential for the experimenter to decide the optimum polymer parameters to obtain the uniform cylinders.

Perturbation in BCP - surface interaction potential strength

In a bulk system the three types of interaction: *A-A*, *B-B* and *A-B* would solely govern the self-assembly of the system. For the confined system studied, there are added energetic consideration for the pair potentials of the surface beads with each of the polymers. Silica surface can be chemically treated to deposit ligands to tailor its interactions with the polymer. The density of these ligands can control the strength of the interactions. Two sets of trials (figure 2.8) have been performed for minor phase volume fractions 0.25-*N60* that formed uniform cylinders at default

surface-BCP interaction potentials ($\epsilon_{S-A} = \epsilon_{S-B} = 1.0$). The first set kept the ϵ_{S-A} constant at 1.0 while varying the ϵ_{S-B} interaction. The next set of trials had the ϵ_{S-A} perturbed keeping ϵ_{S-B} fixed at 1.0. The data has been analyzed by generating minor phase concentration plots for the 17σ and 42σ pillar separation regions. A region of thickness 1σ is considered along the minimum and maximum separation directions with the fractional minor phase concentration plotted on the y axis and the normalized distance on x axis for each of the separation. Additionally, the snapshots of the BCP morphology along the pillar height is also shown. The observations made by these trials was that the ideal morphology formed when the strength of the Surface-BCP interactions (attractive for A , repulsive for B) was the same as the BCP-BCP interactions ($\epsilon_{S-BCP} = \epsilon_{BCP-BCP} = 1.0$). For these optimum parameters we see a two-domain morphology (two distinct concentration peaks) seen in the 17σ region and a three-domain morphology (three distinct concentration peaks) for the 42σ region. Any deviations from this would lead to defects in the morphology. The variation of ϵ_{S-B} lead to disruption in the cylinders formed by breaking the axial symmetry. Many of the cylinder formed were incomplete, that would make them inviable for lithographic applications. Interestingly, the sphericity of the cylinders or the radial symmetry seemed to be intact (slight spreading in the middle domain for $\epsilon_{S-B} = 1.5$). Contrastingly, the variation in ϵ_{S-A} showed much more disruption in the cylinders. Not only were the cylinders incompletely formed, but some of them showed micro-bridging and disruption in the radial symmetry. These results further confirm the observations made by the flat plate 17σ surface-polymer interaction potential perturbation trials on the importance of surface coating to form the ordered morphology.

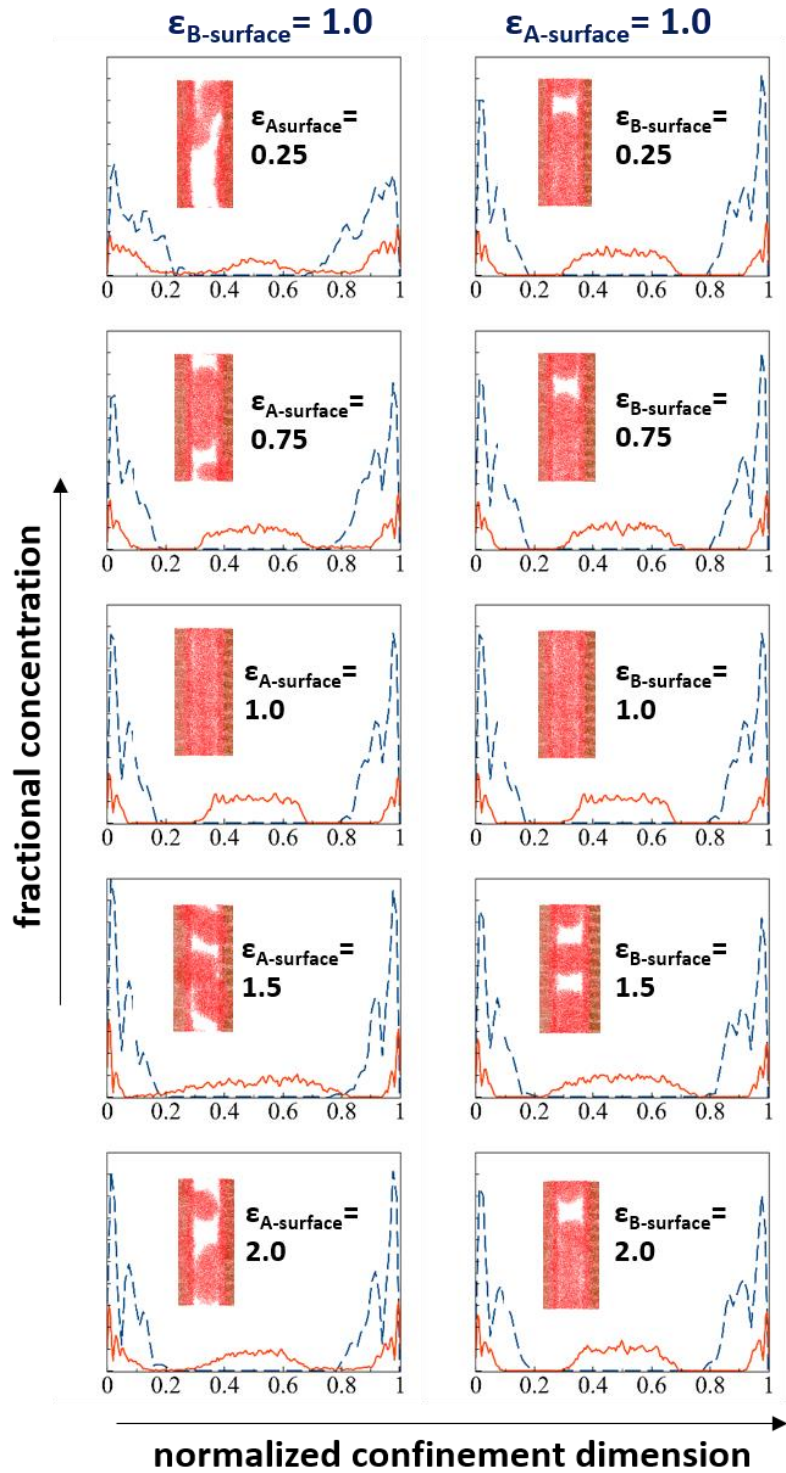


Figure 2.8: BCP-surface interaction pairwise potential perturbation for minor phase volume fraction of 0.25, N_{60} . The red line and blue dashed line represent the fractional minor phase concentration vs normalized confinement dimension plot for a 1σ thick region along the 42σ and 17σ confinement respectively. The insert plots show the snapshot of the cylinder formation along the pillar height. Note: Only minor phase of the BCP (red) is shown for clarity confined between pillars (brown).

2.3.4 Confinement using silica pillars with bottom substrate

The aim of these trials was to study the effect of added confinement of the bottom substrate to the pillars on the morphology formed by the BCP self-assembly. Trials were performed at three chain lengths $N20$, $N40$ and $N60$ and three minor phase volume fractions 0.25, 0.3 and 0.35. The results obtained from these trials show some similarities along with some significant deviation from the pillar confinement trials without the substrate.

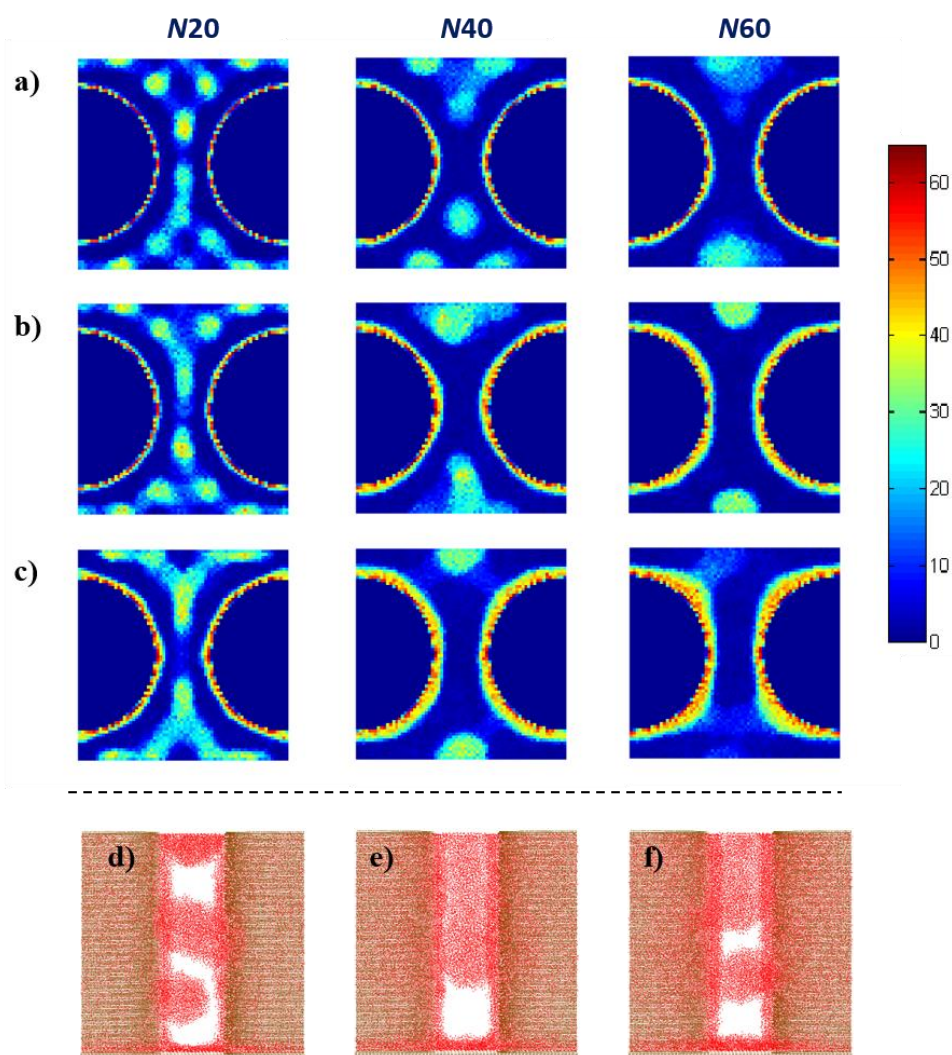


Figure 2.9: minor phase density xy plots of the morphology formed by pillars with bottom substrate at three volume fractions: a) 0.25 b) 0.3 and c) 0.35. Cylinder formation as directed by the pillars with the bottom substrate for d) volume fraction 0.25- $N60$ e) volume fraction 0.30 - $N60$ f) volume fraction 0.35- $N40$. Note: Only the minor phase (red) is shown for clarity. The pillars are shown in purple while the bottom substrate is shown in brown.

Increasing chain lengths from *N*20 to *N*60 form thicker deposition on the pillars as well as on the bottom substrate. The morphology changes from perforated lamellae to incompletely formed ordered cylinders for increased chain length as observed in Figure 2.9 b-*N*60 and c-*N*40. The main difference between the morphology seen in the above trials to the ideal morphology observed in Figure 2.7 is that the minor phase cylinders formed for the template with the substrate are incompletely formed. As part of the minor phase is utilized in coating the bottom surface, there is a deficiency of minor phase beads in the bulk leading to the defect. Increasing the volume fraction to 0.35 does not annihilate the defect observed, but instead forms thicker coating and leads to micro-bridging between the bulk minor phase and surface minor phase domains. Incomplete cylinder formation is a major hindrance for the processing of the templates. The *B* only layer formed in between the minor phase deposited on the bottom substrate and the minor phase cylinder will be left unaffected when the minor phase is etched away following the annealing phase of manufacturing. The device thus will be discarded as the cylindrical path for electron flow to the substrate has a blockade. Strategies for the annihilation of this defect include use of defectants like homopolymers which is outside the purview of this study.

2.3.5 Geometry Comparison

In this section, we compare the three geometries studied and propose a design protocol to form ordered cylindrical BCP arrays with the pillars template using the results obtained from the flat plate confinement studies. Firstly, we perform a qualitative comparison in the morphology formed by the flat plate geometry (at two confinements) and the template with pillars. Figure 2.10 shows the normalized minor phase concentration plots formed for four chain lengths $N10$, $N20$, $N40$ and $N60$ using the methodology adopted in figure 2.8. A direct correlation is observed with respect to the number of continuous minor phase micro-domains in the flat plate trials and the silica pillars template trials. Figure 2.10 compares the minor phase concentration plots of the flat plate 17σ confinement to its ordered pillar counter-part along the 17σ pillar separation (maximum confinement) region. For chain lengths $\leq N20$, along with the two surface peaks around normalized distance = 0.1, we also observe a middle concentration peak. This confirms the observation of a three-domain morphology for the flat plate geometry and the curved perforated three-domain morphology for the ordered pillar template. Higher chain lengths form a two-domain morphology for both the geometries.

Similarly, for the larger length scale of 42σ , we compare the number of concentration peaks or the number of continuous micro-domains for the 42σ flat plate and the minimum confinement region for the pillar geometry. Six and four perforated curved lamellae continuous micro-domains are formed for the minimum confinement region with the pillar template for chain lengths $N10$ and $N20$ respectively as evident from the number of peaks. This is in agreement with the 42σ flat plate trials which also form six and four continuous lamellae domains. As the chain length is increased to $N40$, the morphology formed by the pillar template are ordered cylindrical arrays. This

morphology shows a two-domain structure in the lowest confinement region and three domain structure with the cylinder as the middle domain in the highest confinement region. The flat plate trials for this critical chain length of $N40$ show a two domain and three domain structures for the 17σ and 42σ trials respectively. Further increasing the chain length to $N60$ leads to micro-bridging between the cylindrical domain and one of the surface domains for the pillar confinement trials. The flat plate 42σ trials also show a similar micro-bridging between the middle domain and one of the surface domains. There are some anomalies observed with the minor phase concentration plots normalized for the distance being out of phase for the two geometries. This could be due to the curvature effect imposed by the ordered pillar template. The observation strengthens the claim that a strong qualitative correlation can be made for the number of continuous micro-domains formed for a given confinement separation and chain length.

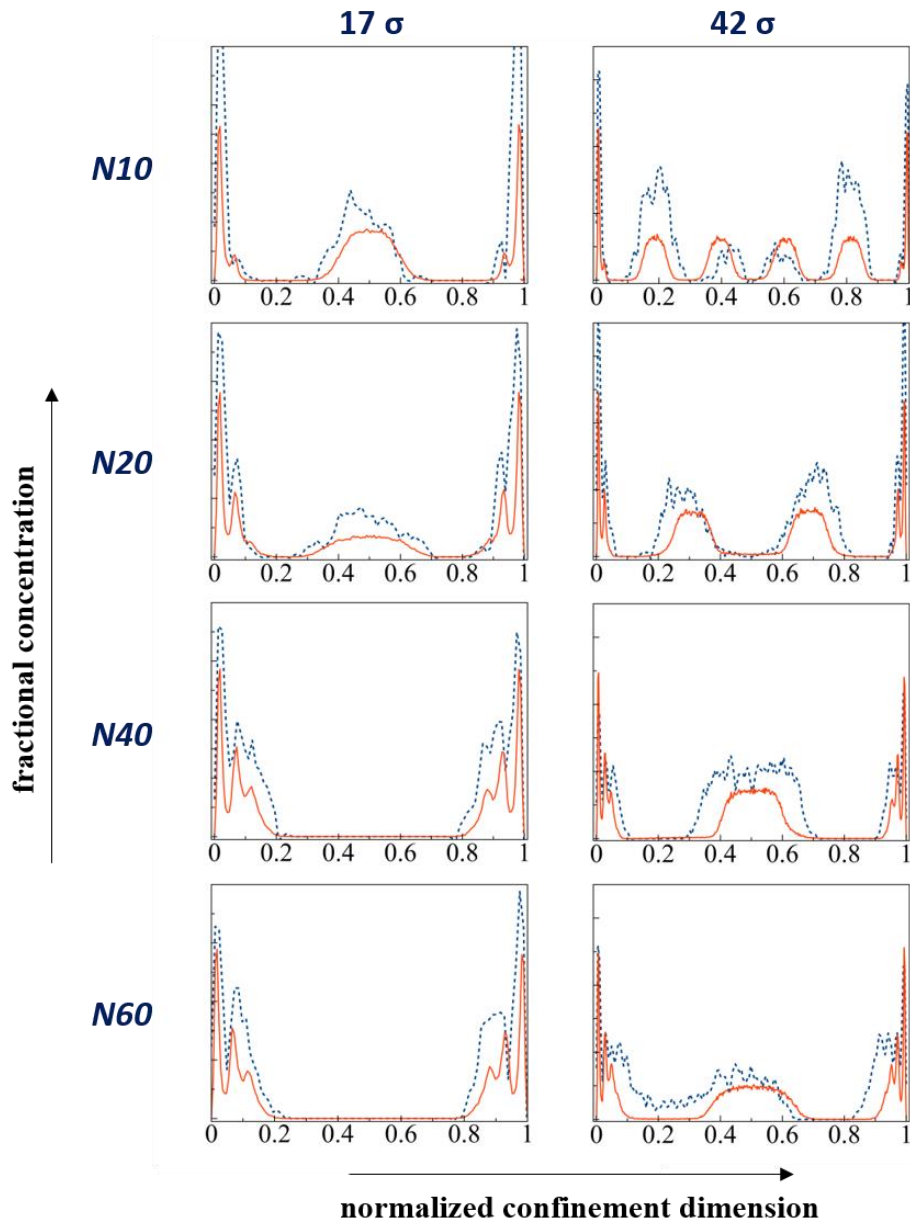


Figure 2.10: Comparison of the morphologies formed by the flat plate geometries at two confinements - 17σ and 42σ with the ordered pillars template at default conditions. The red lines represent the flat plate trials while the blue dotted lines represent the pillars template.

This correlation can be used to design a graphoepitaxial lithographic system like the ‘contact-hole’ cylindrical array template studied in this work. A simple geometric analysis of this cubical pillar

template gives the following relation between the least (L_l) and highest separation (L_h) of the pillars along the line joining their centers for a fixed pillar radius, R_p .

$$L_h = \sqrt{2}L_l + 2(\sqrt{2} - 1)R_p \quad \text{equation-2.10}$$

Using these two separations, the less intricate flat plate simulations for the two plate separations can be performed for a variety of molecular weights to generate plots like those in figure 2.11. For a fixed pillar dimension that is generally limited by the capabilities of the manufacturer, the pitch and the type of BCP can be optimized with these molecular dynamics studies. The results of these studies should lay down an operating regime for the experimenter with respect to the BCP molecular weights. Similar plots have also been generated by varying the volume fractions (figure 2.12). For lower volume fraction we see the operating regime shift to the right to $N60$. As the amount of minor phase is lesser than the default case of volume fraction 0.3, no micro-bridging regime is observed for the chain lengths attempted. For higher volume fractions of 0.35, the optimum regime is formed at $N40$ but this region overlaps with the micro-bridging region as evident from the morphology snapshots.

Design plots can also be generated by varying other process and device parameters like annealing temperature and surface-BCP interaction strengths to have a complete operating regime at the disposal of the manufacturer.

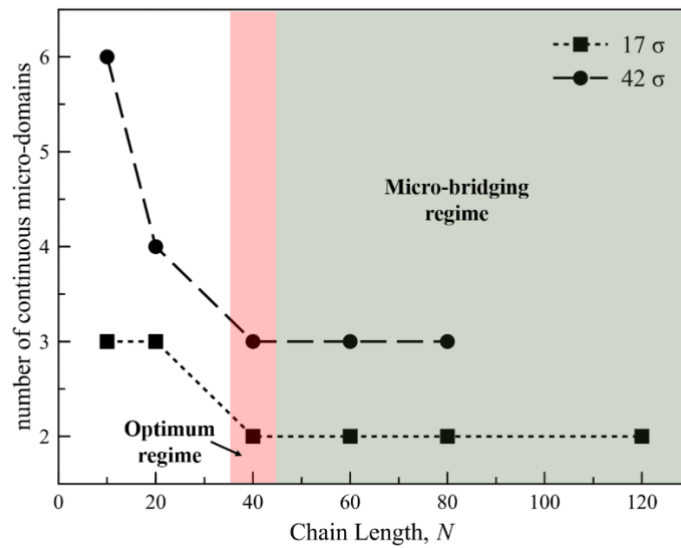


Figure 2.11: Design plots to form ordered cylindrical arrays with flat plate studies. Pink region is the optimum chain length regime while grey region shows the onset of micro-bridging.

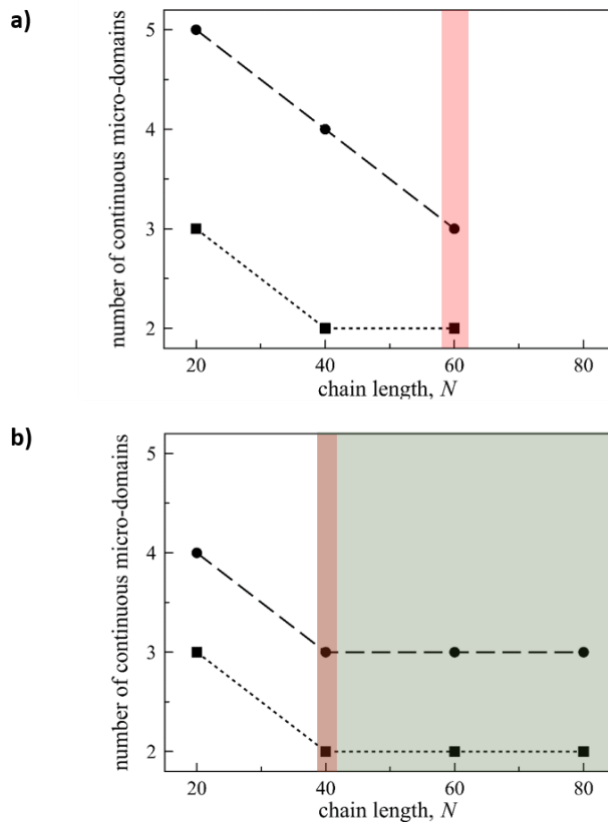


Figure 2.12: Design plots generated by varying minor phase volume fractions for a) volume fraction 0.25 and b) volume fraction 0.35. The pink region shows the optimum regime while grey shows micro-bridging. The 17σ trials are shown by the square points joined by the dotted line while the 42σ trials are shown by the filled circles joined by the dashed line.

2.4 CONCLUSIONS

The morphology formed by the directed self-assembly of block copolymers under flat plate geometry (two plate separations) and templated pillars geometry has been studied using coarse-grained molecular dynamics. For the lower plate separation of 17σ and minor phase volume fraction of 0.3, it was found that there exists a critical chain length, $N40$ where a transition is observed in the morphology formed from a three-domain structure to a two-domain structure. The large entropic penalty experienced by the higher chain lengths make it difficult for the BCP to self-assemble in the middle-bulk region thus leading to the two-domain structure. Perturbing the surface-BCP interaction potential strengths, a morphology-potential phase diagram was generated for a finite annealing time. For a fixed chain length of $N20$, increasing ε_{S-B} at a constant ε_{S-A} lead to a decrease in the micro-bridging between the two-surface continuous minor phase domains while increasing ε_{S-A} at a constant ε_{S-B} lead to a decrease in the middle domain thickness. For the higher plate separation of 42σ , a similar critical chain length was observed at $N40$ where the morphology formed changed from multi-domain (>3) to three-domain structure.

In the next geometry probed the BCP were confined with ordered pillars. To have a close resemblance to the flat plate trials, the separation of adjacent pillars along the lines joining the centers of the pillars was fixed at the plate separations of 17σ and 42σ . For the three volume fractions attempted (0.25, 0.3 and 0.35), increase in the BCP molecular weight lead to a thicker accumulation of the minor phase on the surfaces. The morphology formed changed from a perforated curved lamella to an ordered cylinder with increase in N . The higher chain lengths trials with finite annealing time, for volume fraction - 0.3 and 0.35 showed micro-bridging between the cylinders and the surface minor phase domains. The effect of temperature on the morphology and

surface deposition was also studied. Higher χ or lower temperatures formed thicker coating on the surfaces for chain length $\leq N40$ with not much change in the qualitative aspect of the geometry. Similar to the flat plate trials, the surface-BCP interaction potential strength were also varied. ϵ_{S-A} showed a much stronger effect on the morphology formed as deviation from the ideal values lead to disruption in the radial symmetry, micro-bridging as well as incomplete cylinder formation while the variation in ϵ_{S-B} only lead to incomplete cylinder formation maintaining the radial symmetry of the cylinders. Trials were also performed by increasing the height of the pillars that revealed inability of the cylinders to maintain axial symmetry throughout the height of the pillars (refer supplementary material). In addition to ordered pillars template an added confinement of a bottom substrate was imposed to the BCPs. These trials showed a deposition of the minor phase on the bottom substrate leading to a deficiency of the minor phase in the bulk causing incompletely formed cylinders.

Lastly, we have compared the morphology formed by the different geometries for the same BCP properties. A strong correlation was seen in the number of continuous micro domains formed in the 17σ , 42σ trials and the region surrounding the adjacent pillars separated at 17σ and 42σ . Thus, using simple length scales arguments, we were able to generate design plots by performing flat plate confinement studies to predict the BCP morphology formed for a more intricate geometry involving ordered curved surfaces like the pillars. This can be used as a powerful tool by the experimentalist to design their nano-lithographic template tailor-made for their applications.

2.5 REFERENCES

1. Lawson RA, Peters AJ, Ludovice PJ, Henderson CL. Coarse grained molecular dynamics model of block copolymer directed self-assembly. InSPIE Advanced Lithography 2013 Apr 5 (pp. 86801Y-86801Y). International Society for Optics and Photonics.
2. Srinivas G, Discher DE, Klein ML. Self-assembly and properties of diblock copolymers by coarse-grain molecular dynamics. *Nature materials*. 2004 Sep 1;3(9):638-44.
3. Chen P, Liang H, Shi AC. Origin of microstructures from confined asymmetric diblock copolymers. *Macromolecules*. 2007 Oct 2;40(20):7329-35.
4. Gronheid R, Nealey P, editors. *Directed Self-assembly of Block Co-polymers for Nano-manufacturing*. Woodhead Publishing; 2015 Jul 17.
5. Huinink HP, Van Dijk MA, Brokken-Zijp JC, Sevink GJ. Surface-induced transitions in thin films of asymmetric diblock copolymers. *Macromolecules*. 2001 Jul 17;34(15):5325-30.
6. Huinink HP, Brokken-Zijp JC, Van Dijk MA, Sevink GJ. Asymmetric block copolymers confined in a thin film. *The Journal of Chemical Physics*. 2000 Feb 1;112(5):2452-62.
7. Nikoubashman A, Register RA, Panagiotopoulos AZ. Self-assembly of cylinder-forming diblock copolymer thin films. *Macromolecules*. 2013 Aug 5;46(16):6651-8.

8. Nikoubashman A, Davis RL, Michal BT, Chaikin PM, Register RA, Panagiotopoulos AZ. Thin films of homopolymers and cylinder-forming diblock copolymers under shear. ACS nano. 2014 Aug 15;8(8):8015-26.
9. Pike DQ, Detcheverry FA, Müller M, de Pablo JJ. Theoretically informed coarse grain simulations of polymeric systems. The Journal of chemical physics. 2009 Aug 28;131(8):084903.
10. Turner MS. Equilibrium properties of a diblock copolymer lamellar phase confined between flat plates. Physical review letters. 1992 Sep 21;69(12):1788.
11. Walton DG, Kellogg GJ, Mayes AM, Lambooy P, Russell TP. A free energy model for confined diblock copolymers. Macromolecules;(United States). 1994 Oct 10;27(21).
12. Wang Q, Nealey PF, de Pablo JJ. Monte Carlo simulations of asymmetric diblock copolymer thin films confined between two homogeneous surfaces. Macromolecules. 2001 May 8;34(10):3458-70.
13. Chremos A, Nikoubashman A, Panagiotopoulos AZ. Flory-Huggins parameter χ from binary mixtures of Lennard-Jones particles to block copolymer melts. The Journal of chemical physics. 2014 Feb 7;140(5):054909.

14. Kremer K, Grest GS. Dynamics of entangled linear polymer melts: A molecular-dynamics simulation. *The Journal of Chemical Physics*. 1990 Apr 15;92(8):5057-86.
15. Weeks JD, Chandler D, Andersen HC. Role of repulsive forces in determining the equilibrium structure of simple liquids. *The Journal of chemical physics*. 1971 Jun 15;54(12):5237-47.
16. Hoogerbrugge PJ, Koelman JM. Simulating microscopic hydrodynamic phenomena with dissipative particle dynamics. *EPL (Europhysics Letters)*. 1992 Jun 1;19(3):155.
17. Koelman JM, Hoogerbrugge PJ. Dynamic simulations of hard-sphere suspensions under steady shear. *EPL (Europhysics Letters)*. 1993 Jan 20;21(3):363.
18. Pastorino C, Kreer T, Müller M, Binder K. Comparison of dissipative particle dynamics and Langevin thermostats for out-of-equilibrium simulations of polymeric systems. *Physical Review E*. 2007 Aug 24;76(2):026706.
19. Soddemann T, Dünweg B, Kremer K. Dissipative particle dynamics: A useful thermostat for equilibrium and nonequilibrium molecular dynamics simulations. *Physical Review E*. 2003 Oct 8;68(4):046702.
20. Rubinstein M, Colby RH. *Polymer physics*. New York: Oxford University Press; 2003 Feb.

21. Plimpton S. Fast parallel algorithms for short-range molecular dynamics. *Journal of computational physics*. 1995 Mar 1;117(1):1-9.
22. in't Veld PJ, Plimpton SJ, Grest GS. Accurate and efficient methods for modeling colloidal mixtures in an explicit solvent using molecular dynamics. *Computer Physics Communications*. 2008 Sep 1;179(5):320-9.
23. Humphrey W, Dalke A, Schulten K. VMD: visual molecular dynamics. *Journal of molecular graphics*. 1996 Feb 29;14(1):33-8.
24. Horsch MA, Zhang Z, Iacovella CR, Glotzer SC. Hydrodynamics and microphase ordering in block copolymers: Are hydrodynamics required for ordered phases with periodicity in more than one dimension?. *The Journal of chemical physics*. 2004 Dec 8;121(22):11455-62.
25. Matsen MW, Bates FS. Unifying weak-and strong-segregation block copolymer theories. *Macromolecules*. 1996 Feb 12;29(4):1091-8.
26. Bates CM, Maher MJ, Janes DW, Ellison CJ, Willson CG. Block copolymer lithography. *Macromolecules*. 2014;47(1):2-12.

CHAPTER 3

THREE-DIMENSIONAL LINE EDGE ROUGHNESS IN PRE-AND POST-WET-ETCH LINE AND SPACE PATTERNS OF BLOCK COPOLYMER LITHOGRAPHY

3.1 INTRODUCTION

Over the past decade, with the ever-increasing demand for miniaturization of micro-electronic devices, directed self-assembly (DSA) of block copolymers (BCPs) has attracted the interest of both academia and industry to develop optimal, defect free nanolithographic patterns.¹⁻³ DSA is not restricted by inherent diffraction-based limitations of conventional optical lithography⁴ and has a much lower cost of ownership compared to the competing alternatives⁵. The periodic spatial arrangement of the micro-phase separated bulk BCP⁶ is seldom perfectly achieved with uniformity without it being directed. Hence DSA via external driving force like shear⁷, electric field, magnetic field are used to improve the BCP alignment fitting the desired technological applications.⁸ In the semi-conductor industry, two of the popular techniques include graphoepitaxy⁹⁻¹¹, that uses surface features and confinement to direct the BCP and chemoepitaxy^{3, 12-15}, that uses enthalpic interactions via chemical patterning to control the BCP ordering. Among chemoepitaxial technologies to form line space patterns, Liu-Nealey (LiNe) flow with near symmetric polystyrene-*block*-polymethyl methacrylate (PS-*b*-PMMA) has been widely considered as a prospective DSA candidate for commercialization.¹⁴⁻¹⁵ Using this technique, chemically patterned Si based substrates can effectively direct dense arrays of features with long-range order over wide areas. The BCP thin film is guided using a part of a substrate that has chemical affinity towards PS

domain. The PS-pinned region is patterned with cross-linked PS mat film while the rest of the substrate is brushed with a random hydroxyl terminated PS-*co*-PMMA chain (neutral layer) usually of a lower chain length than the PS mat. PS-*b*-PMMA BCP is then spin coated on top of this chemically patterned substrate and annealed at elevated temperatures (250-300°C) to obtain defect-free BCP lamellae.

Once this ideal lamella morphology is formed, PMMA is selectively etched-off forming a nanolithographic pattern template of the resist, PS. This exercise leaves the patterned substrate exposed and can be further processed for semiconductor applications. The etching process can either be performed with a selective solvent like acetic acid (wet-etching) or using a variety of plasma etches (dry-etching) O₂ / Ar being the most popular etch chemistry.¹⁶⁻¹⁹ While wet-etching is more selective than dry-etching, it has a tendency for the pattern to collapse especially for high BCP film thicknesses due to the diverging surface forces during solvent evaporation. Dry-etching occurs vertically and laterally due to spontaneous etching reactions between etch radicals and PS.

The anisotropic imperfections caused by the etching process coupled with the inherent BCP interfacial width leads to line-edge roughness (LER) and line-width roughness (LWR) in the line space patterns. LER is defined as 3σ deviation of a line-edge from the mean straight line. High LER values in the features leads to hindrance in the flow of electrons leading to anomalies in the device resistance and capacitances making the device inviable.²⁰⁻²¹ The International Technology Roadmap for Semiconductors has listed DSA among one of the top prospective next-generation lithographic alternatives, but along with defectivity, the current high 3σ LER values need further improvements for its commercialization²². To keep up with the Moore's Law²³ in forming smaller,

sleeker micro-electronic devices, it is important to detect the causes of high LER and devise effective strategies to mitigate it. To optimize the strategies, it is important to characterize and quantify the roughness along the film thickness as opposed to the approximated top-down values obtained from SEM images.

Modeling and simulations can aid the manufacturer in this regard. A wide range of DSA modeling work has been achieved using a Self-Consistent Field (SCF) or Theoretically Informed Coarse-Grained (TICG) framework²⁴⁻²⁵. While SCFT has been prevalently used over the years to predict the theoretical BCP phase diagrams, interfacial width cannot be accurately measured if the fluctuations are not accounted for. TICG with its improvised strategies considers fluctuations and has been popularly used in recent years to study chemoepitaxial DSA, especially to predict the energetics of defect annihilation.²⁶⁻²⁷ Owing to the higher degree of coarse-graining, the roughness values computed using TICG or allied methodology like Single-Chain-in-Mean-Field (SCMF) simulations is limited to low frequency estimation in the frequency domain. Dauloas, Stoykovich and co-authors have studied the effect of roughness of the patterned substrate and its propagation through the film thickness, for undulated and peristaltic low frequency variation using a SCMF approach with successful comparison with experiments.²⁸⁻²⁹ Recently, Segal-Peretz *et al.* have demonstrated the implementation of TICG in conjunction with scanning transmission electron microscopy to characterize the three-dimensional structure of DSA with high- χ BCP, P2VP-*b*-PS-*b*-P2VP.³⁰ Coarse-grained polymer field-theoretic simulations have also been employed by Bosse and co-authors to predict the interfacial fluctuations for BCP resists with a peak in the spectral plots at the BCP interdomain spacing.²² Although these simulations are computationally economical, the authors categorically state their limitations in characterizing high frequency

roughness and suggest the need for intensive particle based molecular dynamics (MD) approach for a more complete understanding. Among the few available MD literature on the subject, there is a lack of matching of the BCP chain length to the actual molecular weight and the corresponding experimental BCP pitch (L_0^{exp}).³¹⁻³²

More importantly, none of the above stated works study the resist morphology evaluation after etching one of the BCP phases. While characterizing the interfacial deviations is crucial, the actual pattern transfer to the underlying Silicon substrate takes place with the removal of the non-resist BCP phase. In this work, we have used large-scale coarse-grained molecular dynamics (CGMD) simulations with close matching of experimental BCP chain length, L^0 and substrate dimensions to study the 3-dimensional BCP morphologies of DSA with LiNe flow over three process stages: after annealing, after quenching below glass transition of resist (*pre-etch*) and after selective wet-etching of the non-resist BCP phase (*post-etch*).

3.2 MODEL AND METHODS

The polymer chain is modeled as an AB block with both monomer radii (σ') equal to 1nm. Block A contains 4 molecules of PS while block B contains 4.5 molecules of PMMA to account for the difference in bulk densities of the two monomers. Each polymer chain comprises of 63 beads of PS ($\sim 26,000 \text{ g mol}^{-1}$) and 58 beads of PMMA ($\sim 26,000 \text{ g mol}^{-1}$). The reduced mass of each bead is adjusted according to the respective coarsening for PS and PMMA. The interaction between bonded BCP beads is given by the FENE bond potential, $U_{fene}(r) = -0.5KR_{max}^2 \ln[1-(r/R_{max})^2]$ where $K = 30 \epsilon \sigma'^{-2}$ is the spring constant of the BCP bond while $R_{max} = 1.5\sigma'$ is the maximum bond extensibility.³⁴ The favorable long-range interactions are governed by a tail-corrected Lennard-Jones interaction given by $U_{attractive}(r) = 4\epsilon[(\sigma'/r)^{12} - (\sigma'/r)^6] + S_{LJ}(r)$ for $r < 2.5 \sigma'$ while the repulsive interaction is in accordance to Weeks-Chandler-Anderson (WCA) potential, $U_{repulsive}(r) = 4\epsilon[(\sigma'/r)^{12} - (\sigma'/r)^6]$ for $r < 2^{1/6} \sigma'$.³⁵ A global BCP site density of $0.85 \text{ beads nm}^{-3}$ is maintained and the thermostat employed is Nosé-Hoover.

The BCP in the study corresponds to PS-b-PMMA with $L_0^{exp} = 28 \text{ nm}$. Bulk trials were performed varying the Lennard-Jones interaction parameters $\epsilon_{BCP-BCP}$ to elucidate parameters for $L_0^{sim} \sim L_0^{exp}$ for various chain lengths. The optimized parameters from the bulk study, $\epsilon_{PS-PS, attractive} = 0.15$, $\epsilon_{PMMA-PMMA, attractive} = 0.15$ and $\epsilon_{PS-PMMA, repulsive} = 0.15$ were used for the main simulations. The simulation box is periodic in x and y and fixed in z with a BCP film thickness of $L_0 = 28 \text{ nm}$. The substrate is three layered thick ($3 \sigma'$) with hexagonal packing. As the maximum cut-off radii for any interaction is $2.5\sigma'$, any thickness greater than $2.5\sigma'$ will not affect the BCP morphology. The neutral substrate beads interact with the BCP with $U_{attractive}(r)$. The pinned substrate interacts with

PS beads by $U_{\text{attractive}}(r)$ and with PMMA beads by $U_{\text{repulsive}}(r)$. The default interaction strength of the neutral brush with the BCP, $\epsilon_{\text{BCP-neutral}} = 0.15kT$.

Substrate details

The experimental trials were performed with the LiNe flow process using EMD's block copolymer, PME-7001 on NLD-128 (PS mat pinning) and NLD-127 (neutral brush) prepattern. The pattern multiplication is 3X with a patterning pitch of 84 nm and a pinning width of 18 nm (optimum for experimental trials). The film thickness is about $1.2L_0 \sim 35$ nm to offer higher tolerance for pattern for post PMMA-etch pattern transfer. Substrate fabrication and annealing conditions have been kept similar to Liu et al.¹⁴⁻¹⁵ The PMMA phase is etched with Ar/O₂ plasma etch with selectivity close to 2.5.

Two types of patterned chemoepitaxial substrate were used for the LiNe flow process. The first substrate has a flat geometry (figure 3.1a) with part of the substrate being selective to PS. The selectively patterned substrate that corresponds to the cross-linked PS mat has a pinning width (pw) = 16 nm ($\sim 0.57 L_0$) and a density multiplication of 3X, indicating 3 domains each of PS and PMMA per patterning. The non-patterned part of the substrate that mimics the neutral brush in experiments is non-selective towards either of the phase with $\epsilon_{\text{neutral-BCP}} = 0.15$ at annealing conditions. In the second substrate type (figure 3.1b), the PS mat has a topography with the pinned region raised at a height of 3nm with respect to the neutral brush. The molecular weight of the cross-linked PS is usually higher compared to the neutral brush which induces topography in the substrate.

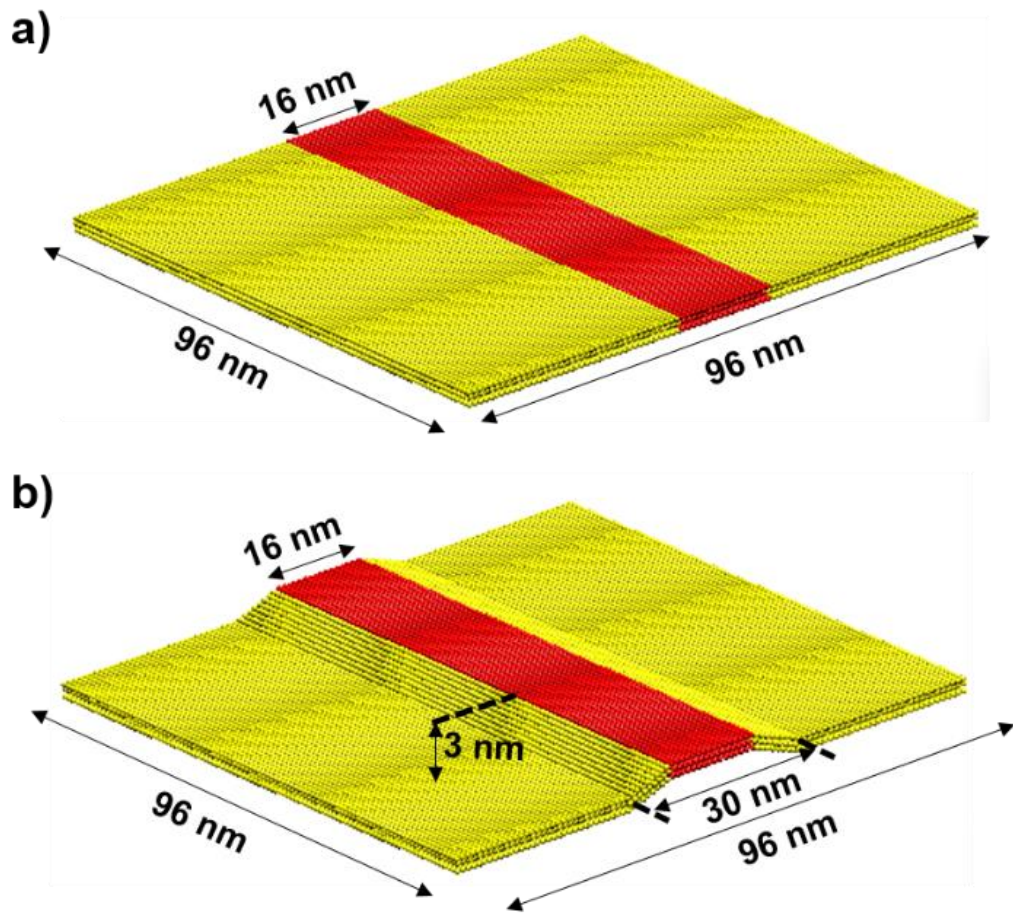


Figure 3.1: Substrate for LiNe CGMD simulations with a) flat substrate and b) substrate with topography. PS mat shown in red and neutral brush in yellow.

3.3 RESULTS AND DISCUSSIONS

3.3.1 *Lamellae formation*

In the first stage of the process, the system is annealed at $T_{\text{anneal}} = 1.2$ to form defect free lamellae structures. The lamellae morphology profile formed by using the two types of substrate is shown in figure 3.2. For the flat plate substrate, an interaction strength $\epsilon_{\text{PS_mat-PS, attractive}} = 0.15$ and $\epsilon_{\text{PS_mat-PS, repulsive}} = 0.15$ was sufficient to form defect free structures in ~ 7 million steps (refer to methods for model details). The confinement effect imposed by the substrate topography required stronger pinning of $\epsilon_{\text{PS_mat-PS, attractive}} = 1.0$ and $\epsilon_{\text{PS_mat-PS, repulsive}} = 1.0$ to annihilate the defects with slower kinetics of ~ 20 million steps. The defects observed in both substrate types and interactions strengths included micro-bridge and dislocation defects. The structures were then cooled to T_{etch} , below the glass transition temperature, T_g of PS in the second process stage. Independent bulk trials were performed with only the PS part of the BCP (N63) and the mean squared displacement of the equilibrated melt was plotted for temperatures ranging from 0.1 to 1.2.³³ The point of change in slope of the curve thus generated denoted the $T_g \sim 0.3$.

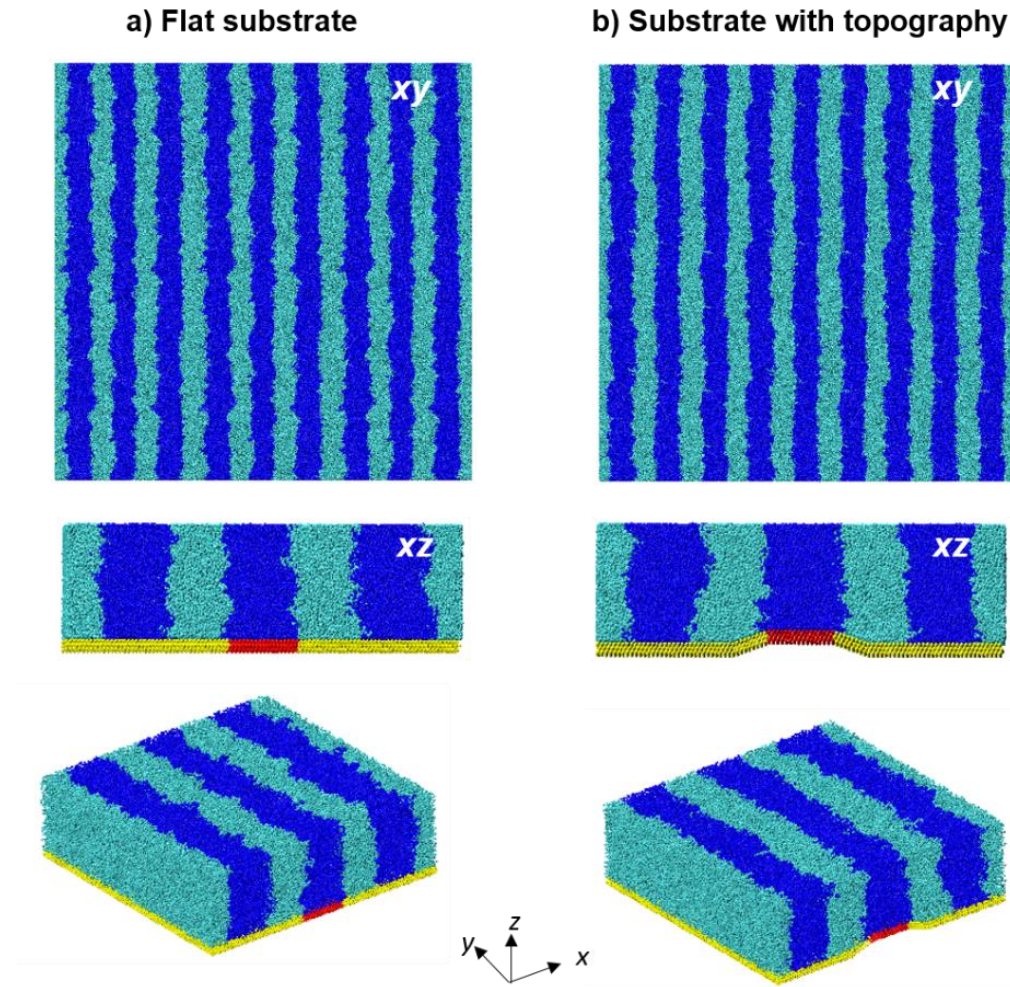


Figure 3.2: Morphology profiles after annealing ($T_{\text{anneal}} = 1.2$). for a) flat substrate and b) substrate with topography. PS is shown in blue and PMMA in cyan.

At temperatures below T_g , the brushes are in a collapsed state with lower kinetic energy and effective surface area. Thus, to accurately capture the brush dynamics with stationary substrate beads, the $\epsilon_{\text{neutral-BCP}}$ is lowered to 0.1 at lower temperatures as opposed to $\epsilon_{\text{neutral-BCP}} = 0.15$ at elevated temperatures when the brushes have higher kinetic energies and more exposed surface areas to interact with the BCP.

3.3.2 Morphology evaluation with solvent etching

After the system is equilibrated below T_g , in the third process stage, the PMMA phase is selectively etched off under wet-etching conditions. The experimental annealing time is much greater than the etching time-scale (~ 30 s). We thus simulate the etching process under the following simultaneous conditions: instantaneous breakage of PS-PMMA bonds and removal of PMMA beads followed by addition of etching solvent beads to replace the PMMA beads. The PS domains are thereafter equilibrated along with the etching solvent for the domain morphology to evolve. The etching solvent is ideally poor with respect to PS for high etch selectivity with the solvent quality being governed by the cross-interaction LJ parameter in the WCA potential, $\epsilon_{PS-solvent}$. Figure 3.3a shows the effect of three solvent types I (blue circle), II (black diamond) and III (red squares) at a reduced temperature of $T_{etch} = 0.15, 0.2$ and 0.25 on the morphologies of the three PS domains every 2 nm along the film thickness for the flat patterned substrate. Higher the $\epsilon_{PS-solvent}$, poorer is the solvent, better is the quality of the etching solvent. Solvent type I and II are poor with respect to PS with $\epsilon_{PS-solvent-I,rep} = 0.25$ and $\epsilon_{PS-solvent-II,rep} = 0.1$ respectively. $\epsilon_{solvent-solvent, att} = 0.2$ for I and II. Solvent type three approaches the behavior of a good solvent with $\epsilon_{PS-solvent-III,rep} = 0.05$ and $\epsilon_{solvent-solvent, att} = 0.1$. The pinned domain rests above the PS mat patterning while the other two domains are identified as unpinned-left and right respectively.

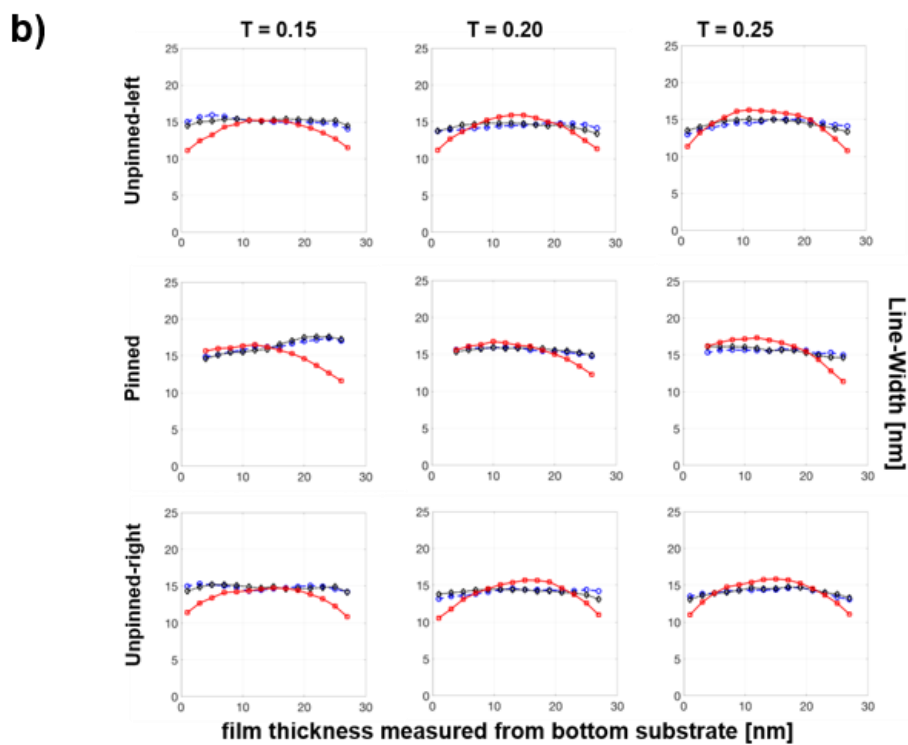
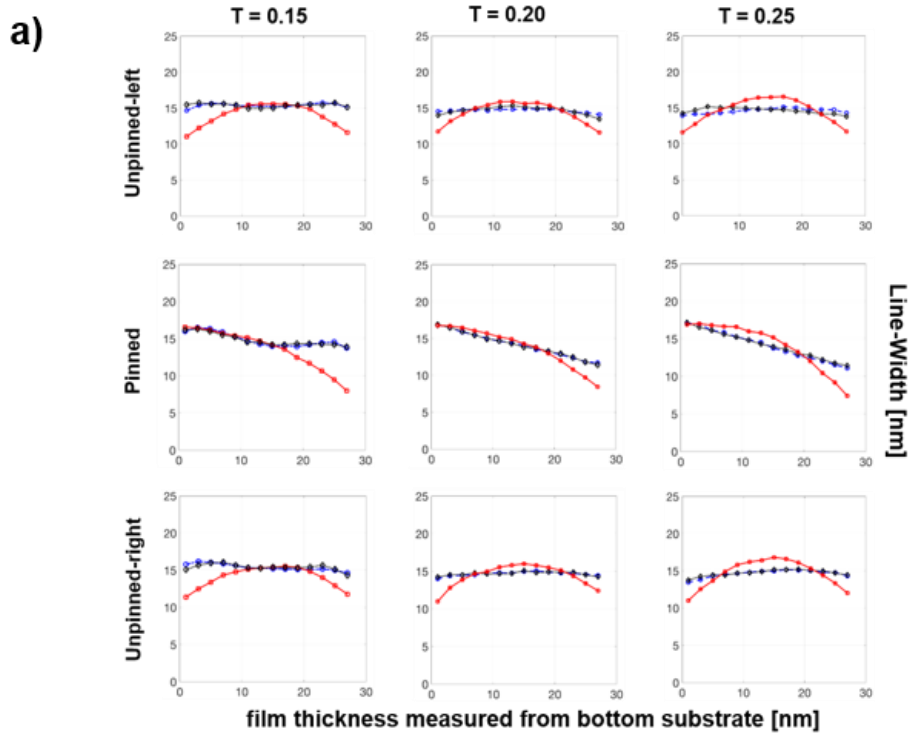


Figure 3.3: PS Line-Width vs film thickness plots for three solvent types. Type I and type II are poor solvents for PS denoted in blue circle and red diamonds respectively. Type III approaches good solvent regime shown in red squares. The PS domain above the PS-mat is pinned.

a) flat substrate b) substrate with topography

The results show that etching with solvent III leads to significant pattern collapse for the three temperatures. The pinned domain has a gradient for the Line-Width that tapers away from the bottom substrate. The favorable enthalpic interaction offered by the PS-mat can hold the domain intact close to the bottom substrate but as the interactions fades away from the bottom substrates, the PS-solvent interactions lead to a gradient that spreads at the base and tapers parallel to the film thickness. For the unpinned domains, solvent III bulges close to the middle of the film height caused by the absence of favorable bottom substrate interactions along with the favorable $\epsilon_{\text{neutral-solvent}}$ interactions. For the poor solvents I and II, the unpinned domains remain constant in line-width along the film height for the three T_{etch} . The pinned domain shows a gradient along the film height for $T_{\text{etch}} = 0.2, 0.25$. As the temperature approaches T_g , PS beads have higher kinetic energy to move and coupled with the favorable PS mat interactions, the line-width tapers away from the substrate. Figure 3.3b shows similar plots generated for substrate with topography. The main difference in the morphology for the two substrate geometries for the good solvents is that the flat substrate results in more resist Line-Width gradient for the pinned domain for temperatures closer to T_g . The effect of solvent drying and the subsequent structure disruption owing to high surface forces under low solvent condition is outside the purview of the study.

3.3.3 *Multi-stage LER evaluation*

The three-dimensional morphology and LER is evaluated along the film thickness and at each stage of the process for the flat substrate in figure 3.4a and substrate with topography in figure 3.4b. The PS edge for the post-etch stage has contribution from BCP interfacial width and etching process while pre-etch have contribution only from BCP interface fluctuations. For the three PS domains, the general trend shows higher LER for the annealing stage over pre-etch and post-etch stage. At elevated temperatures, as the melt has higher kinetic energy to move, higher fluctuations are seen at the interface. The roughness data also shows a qualitative change in LER profile along the film thickness. But, as seen in figure 3.4c-d, the values for average LER over the entire film thickness for right and left edges is practically same for the pre-and post-etch stages. The unpinned domains have slightly higher values for the post-etch stage while pinned domains are a little higher for the pre-etch stage for the flat substrate. For the substrate with topography, the post-etch roughness is only incrementally higher than the pre-etch. For both these stages for the two substrate geometries, the $\langle \text{LER} \rangle_{\text{ht}}$ are substantially lower as compared to the annealing values indicating that temperature to be more dominant factor over solvation caused by the poor etching solvent.

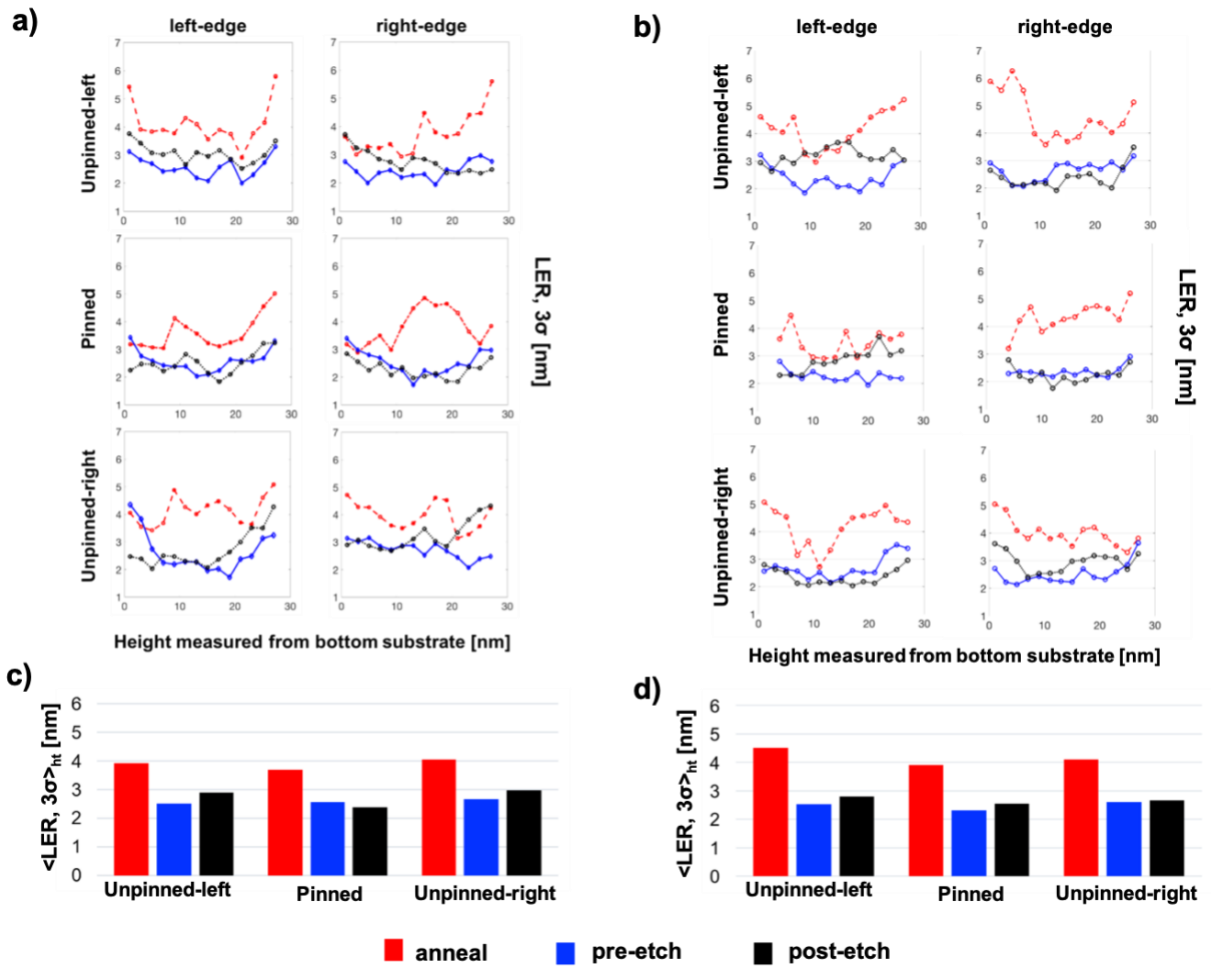


Figure 3.4: a) LER vs film thickness plots for the three process stages: anneal (red dash line), pre-etch (blue line) and post-etch (black dotted line) for a) flat substrate and b) substrate with topography. Height/left and right edge averaged LER comparison for c) flat substrate and d) substrate with topography

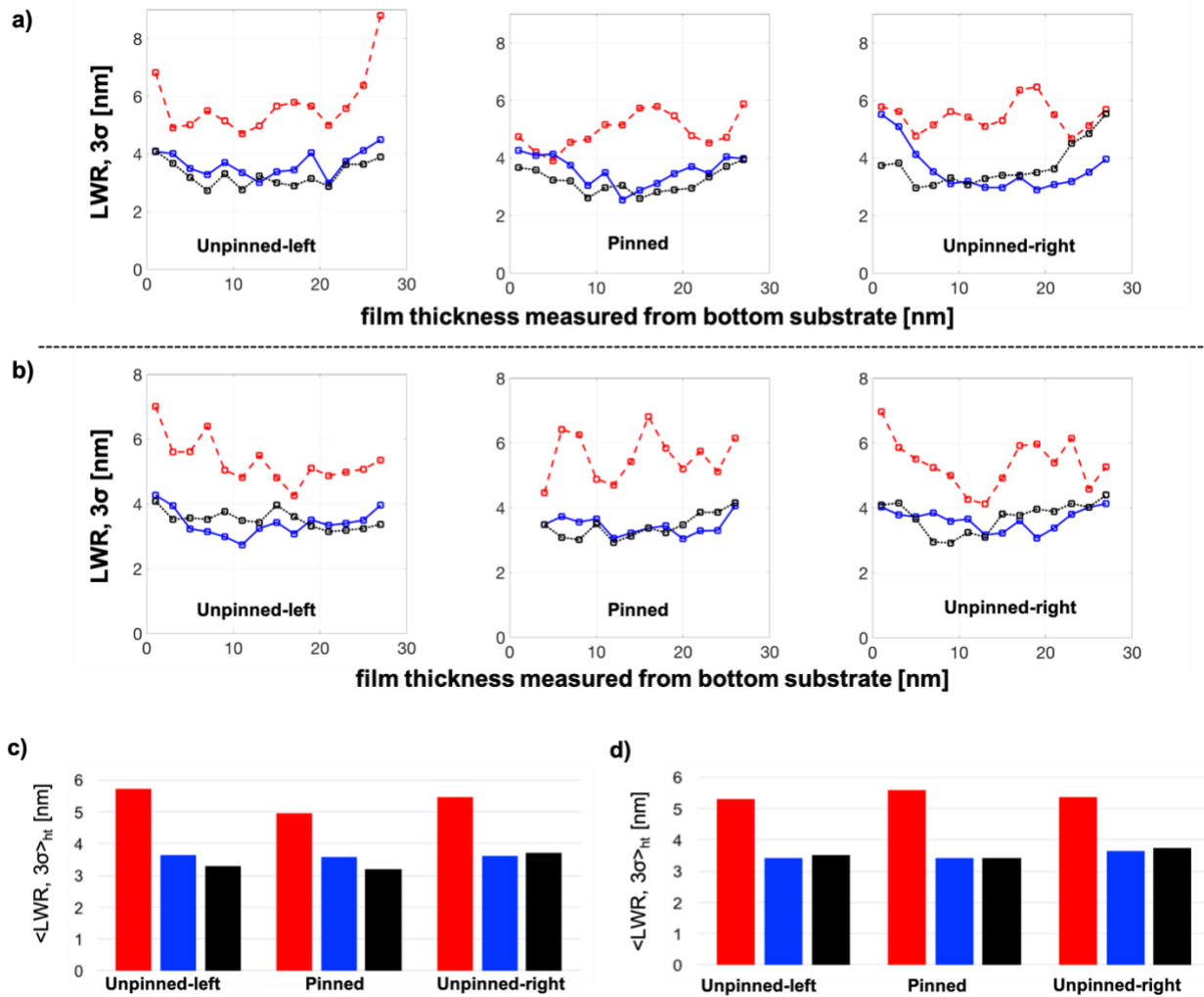


Figure 3.5: LWR as a function of film thickness for the three PS domains for a) flat substrate and b) substrate with topography. Height averaged LWR for c) flat substrate and d) substrate with topography. The anneal stage is shown in red, pre-etch in blue and post-etch in black.

A similar observation is seen for the LWR variation with the film height. In figure 3.5a-b, the LWR variation is seen for flat substrate and substrate with topography respectively and the average height LWR profiles in figure 3.5c-d. The Line-Width Roughness is higher for the anneal stage than the other two stages. The pre-and post-etch LWR have very similar values with the post-etch values only incrementally higher for substrate with topography.

To understand the contributions of the low and high frequency roughness, we plot the power spectral density (PSD) for both the edges of the three domains. We treat each of the planar PSD for the film thickness (separated at every 2 nm) as similar and study the average PSD profile to generate 6 plots at the three process stages as seen in figure 3.6. As expected, comparisons between the anneal stage to the cooled stages (pre-and post-etch) shows trend similar to the space domains with the anneal having significantly higher magnitude for the entire spectrum. For lower frequencies, post-etch on average has higher contribution compared to the pre-etch spectrum while for middle (close to correlation frequency) and high frequencies the post-etch spectrum on average is slightly lower than pre-etch. This is especially interesting as the average LER for pre-and post-etch is very close in magnitude in the space domain. This observation in the frequency domain was also observed for simulations with substrate with topography.

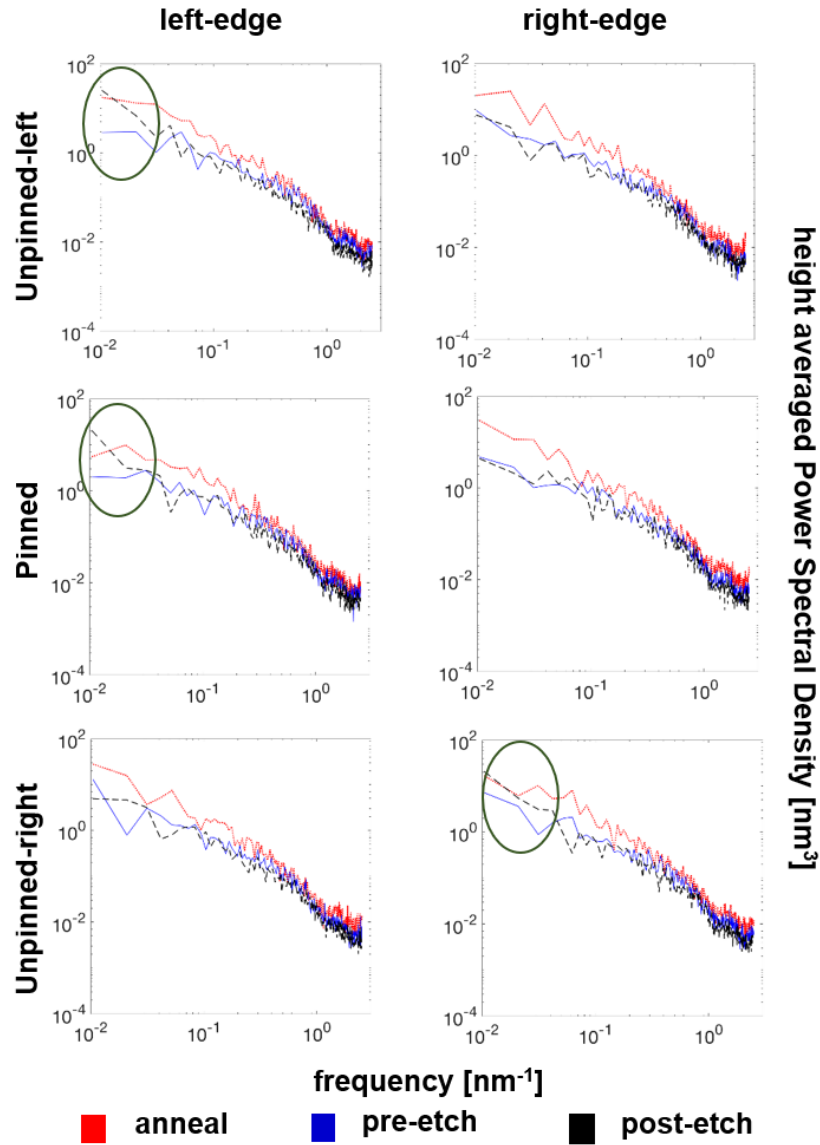


Figure 3.6: Height averaged power spectral density for PS domains for the three process stage for flat substrate geometry. PSD_{anneal} always has the highest contribution. On an average, post-etch has higher lower frequency contribution than pre-etch.

3.3.4 Experimental comparison

The simulation values are compared to experimental results obtained from an SEM image of a self-assembled PS-*b*-PMMA with L_0 close to 28 nm. The PMMA phase of the self-assembled BCP is etched off with O_2 / Ar based plasma. Assuming high PMMA selectivity for the O_2 / Ar plasma, the conditions of poor solvent wet-etch below T_g would be a fair approximation for the process.

As evident from figure 3.4, the solvent employed does not significantly alter the average roughness values. The experimental SEM image corresponds to a pixel size of ~ 1.25 nm. The image is processed using Median and Gaussian filters after which the edges are detected using a Canny edge detection algorithm (figure 3.7a). For the 62 clean lines captured, the $\langle \text{LER} \rangle_{\text{exp}} = 2.98 \pm 0.28$ nm (figure 3.7b). This is in close agreement with the simulations for the height averaged (every 2 nm) roughness value for the 6 edges, $\langle \text{LER} \rangle_{\text{ht, flat}} = 2.75$ nm and $\langle \text{LER} \rangle_{\text{ht, topography}} = 2.69$ nm (figure 3.7c). The $\langle \text{LWR} \rangle_{\text{ht, flat}} = 3.39$ nm and $\langle \text{LWR} \rangle_{\text{ht, topography}} = 3.57$ nm values predicted from the CGMD simulation show a slight deviation from the SEM image of $\langle \text{LWR} \rangle_{\text{exp}} = 2.66 \pm 0.16$ nm.

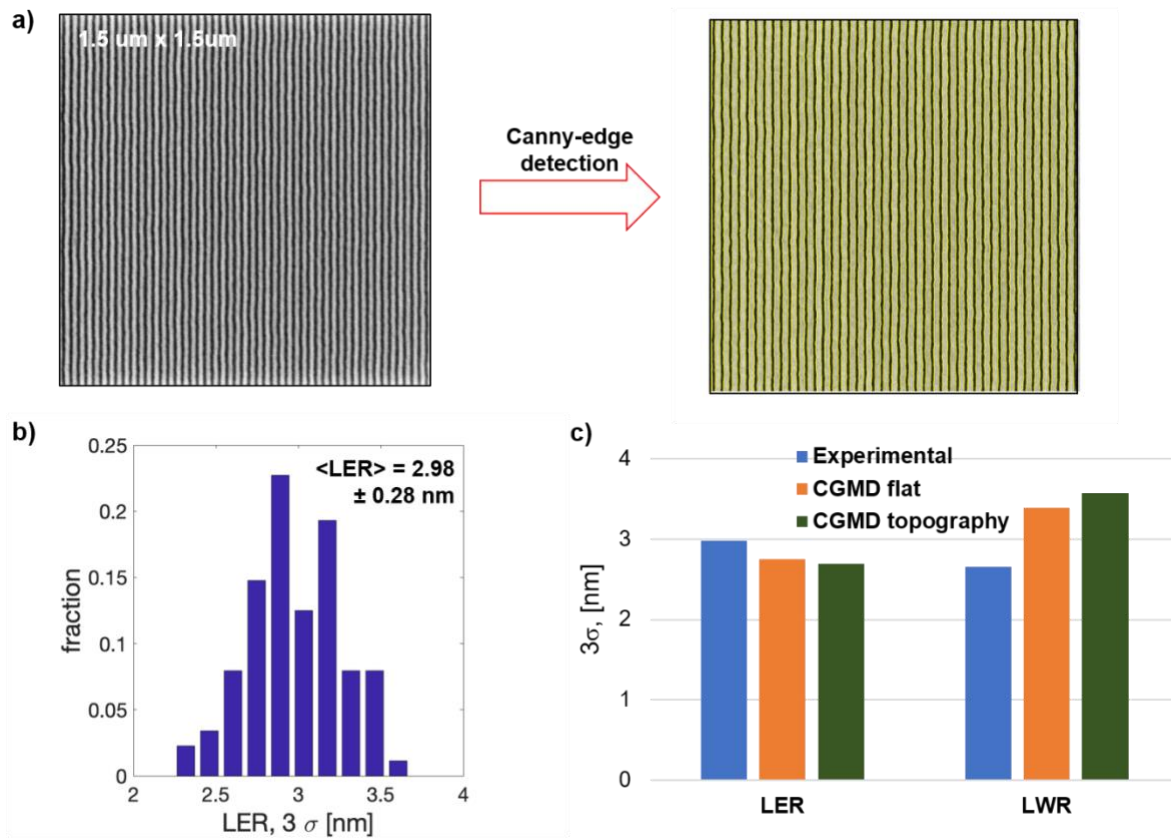


Figure 3.7: a) Edge detected SEM image for PMMA etched line space pattern obtained via LiNe flow. b) Histogram for LER for a). c) Comparison between experimental roughness and height averaged CGMD results for the two substrate geometries.

The deviations in line-edges obtained for each line in the SEM image is treated as a signal in length which is low-pass filtered to remove spatial aliasing and subsequently windowed using a 4-term Blackman-Harris window to reduce emphasis on the edge points in the series. The cut-off frequency chosen was 0.9 times the Nyquist frequency. The processed signal is then Fourier transformed to generate a surface PSD of the 62 lines as shown in figure 3.8a. Beyond the correlation frequency, the high frequency contribution is further resolved by fitting a straight line for each of the 62 signals. The slope obtained from this fit denotes the fractal dimension, D (figure 3.8b) with $\langle D \rangle = 1.77 \pm 0.1016$. The fractal dimension for a self-similar series can be related to the Hurst or roughness exponent (H) by $D = 2 - H$, with higher H indicating a less volatile trend. $\langle H \rangle$ between 0 - 0.5 in general and $\langle H \rangle = 0.23$ for the current image signifies a long-term switching between high and low edge deviations in adjacent pixels lasting for a substantially long length across the line edge.

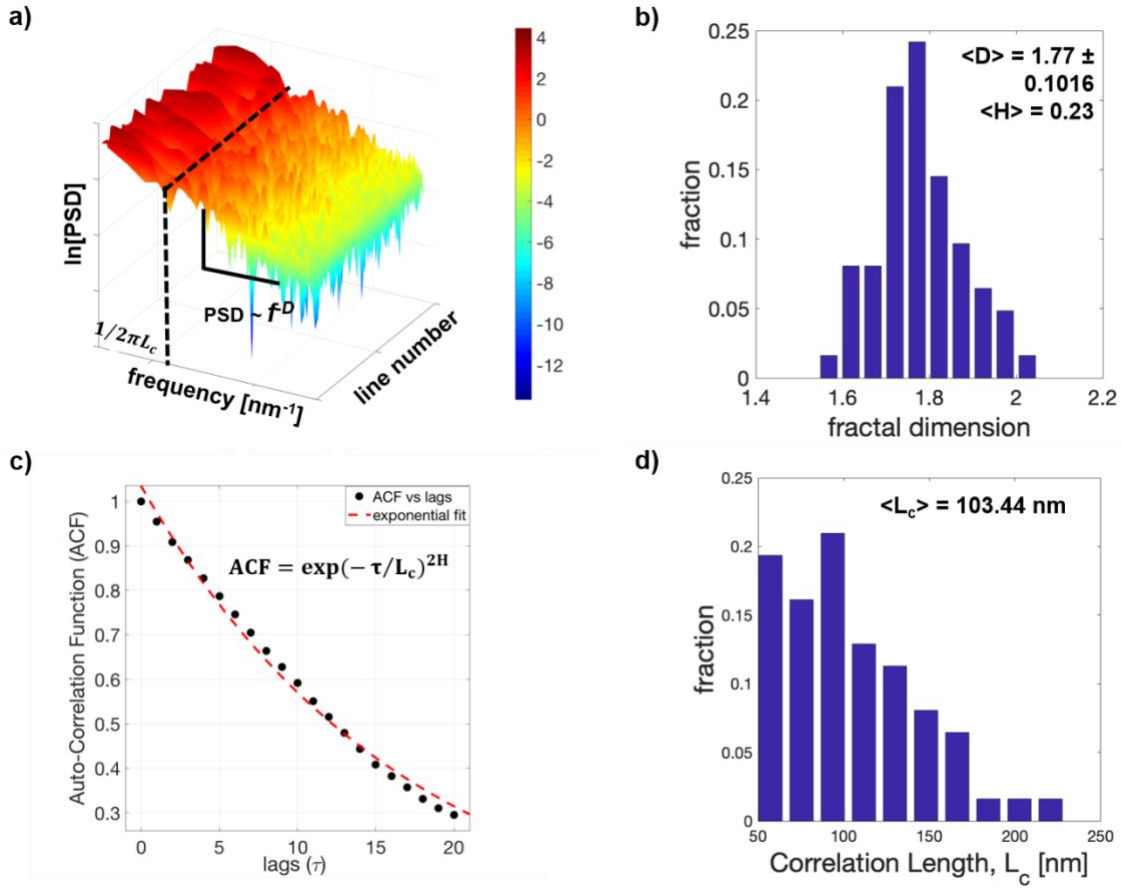


Figure 3.8: a) Surface power spectral density example plot. Beyond the correlation length, the PSD is fit to f^D . b) fractal dimension histogram for the 62 defect free lines captured through image analysis. c) exponential fit for the auto-correlation function for a sample line. The roughness exponent, H is obtained from figure 3.8b for each of the line. d) histogram for correlation length L_c , obtained from fitting the exponential auto-correlation function

As figure 3.8a shows, the PSD for each of the individual line is noisy. The exact point of distinction between the low and high frequencies to obtain the correlation length can be tricky using only the PSD curves. Alternatively, the auto-correlation function (ACF) can be generated for each of the line as a function of the lags (τ). This ACF is fit to an exponential fall model, $\text{ACF} = \exp(-\tau/L_c)^{2H}$. The H being the roughness or Hurst exponent obtained in figure 3.8b for each of the line and L_c is the correlation length. The histogram for L_c is shown in figure 3.8d with $\langle L_c \rangle = 103.44 \text{ nm}$ indicating significant contribution from low frequency roughness. As we are limited with our

simulation box size with ~100 nm line length as opposed to 1500 nm for experimental line length, comparison in the frequency domains are not made for the two.

Next, we perform a 3D comparison of the solvent etched simulation morphology with a cross-sectional PMMA etched SEM image. A qualitative comparison can be made between the experimental image in figure 3.9c with a simulation image etched with a poor solvent in figure 3.9a and good solvent in figure 3.9b (for flat substrate geometry). Each of the three domains of the simulations is averaged to generate the line-width as a function of the film thickness measured from the bottom substrate. The cross-sectional image is processed to isolate individual domains and averaged out over the optimally detected resist domains. The results show that the experimental SEM images have a higher gradient for the line-width as compared to the wet-etching with a poor/good solvent. The good solvent has stronger interactions with the PS resist domains leading to slight bulging of the domains at the center. Figure 3.9d also suggests that the current images show a higher resist mass at the bottom substrate leading to a higher gradient. It is likely that the excess mass is caused by incomplete PMMA removal and similar PS-PMMA phase densities leads to a poor interface distinction for the BCP edge. Correction for this overestimation will lead to a closer agreement. Moreover, O_2/Ar plasma with its higher anisotropy is expected to consume more of PS especially away from the bottom substrate. A dry-etching simulation methodology to model ion-bombardment has simultaneously been developed which will be addressed in a subsequent publication.

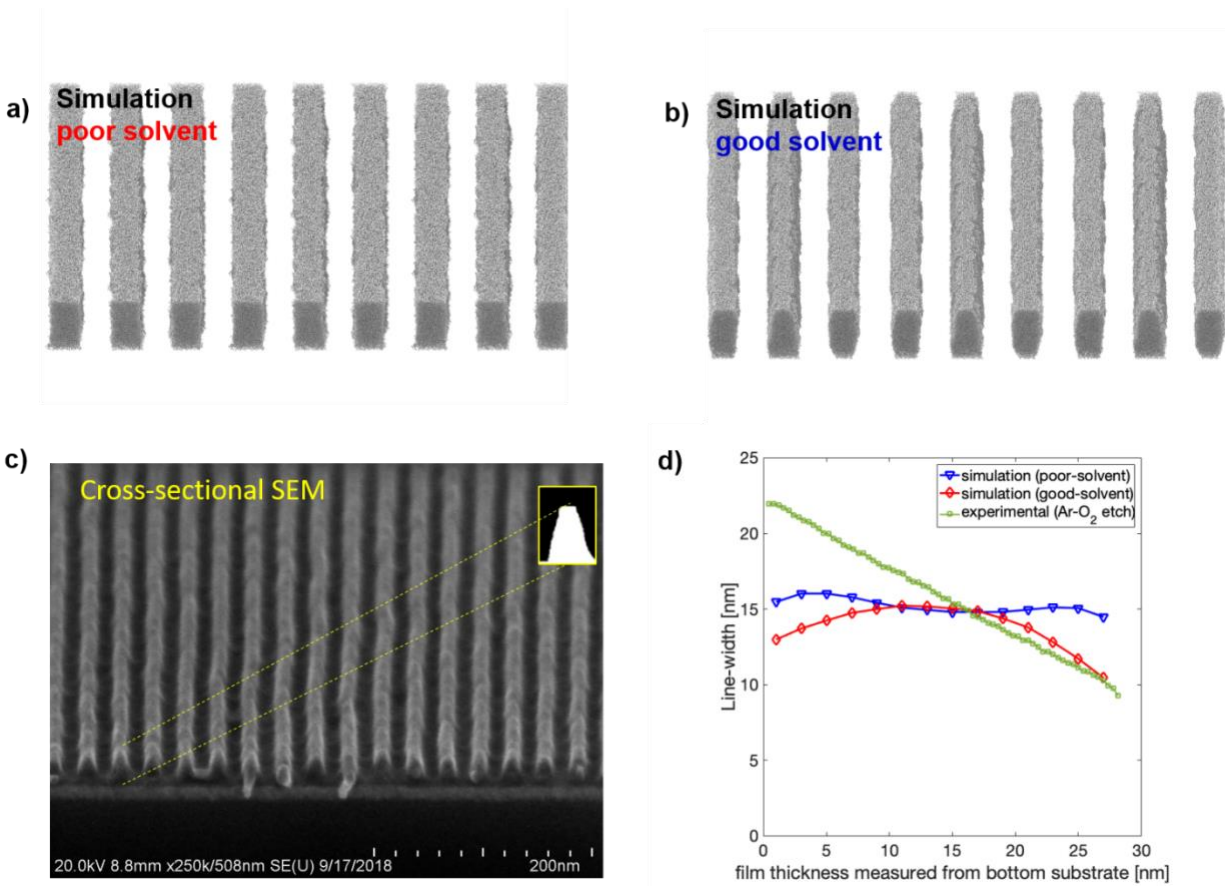


Figure 3.9: a) repeated patterns generated for the poor solvent etched CGMD simulations for flat substrate geometry. b) repeated patterns generated for the good solvent etched CGMD simulations for flat substrate geometry. c) Cross-sectional SEM image for PMMA etched line and space patterns.

3.4 SUMMARY

Using a large-scale CGMD model, we have studied the three-dimensional profiles of line and space patterns formed from symmetric BCPs at three process stages: anneal, pre-and post-etch. The etching is studied using a novel modeling approach for a DSA wet-etching schematic. The effect of solvent quality at different etching temperatures showed least pattern collapse for poor solvents at the lowest T_{etch} value attempted. The $\langle \text{LER} \rangle_{\text{ht}}$ were substantially higher for the annealing stage of the process as compared to the cooling and etching stage. Although, there was not a substantial difference in the height averaged LER and LWR values for the pre-and post-etch edges, the power spectral density showed a qualitative difference in the distribution of the roughness. A pre-etch edge with larger high frequency contribution would likely increase in its relative low frequency contribution post-etch. Comparison with equivalent Liu-Nealey flow experiments show close matching in the average roughness values obtained by image processing the SEM images and the etched CGMD results for the flat substrate and the substrate with topography.

3.5 REFERENCES

1. Jeong SJ, Kim JY, Kim BH, Moon HS, Kim SO. Directed self-assembly of block copolymers for next generation nanolithography. *Materials Today*. 2013 Dec 31;16(12):468-76.
2. Liu CC, Ramírez-Hernández A, Han E, Craig GS, Tada Y, Yoshida H, Kang H, Ji S, Gopalan P, de Pablo JJ, Nealey PF. Chemical patterns for directed self-assembly of lamellae-forming block copolymers with density multiplication of features. *Macromolecules*. 2013 Feb 11;46(4):1415-24.
3. Ruiz R, Kang H, Detcheverry FA, Dobisz E, Kercher DS, Albrecht TR, de Pablo JJ, Nealey PF. Density multiplication and improved lithography by directed block copolymer assembly. *Science*. 2008 Aug 15;321(5891):936-9.
4. Mack CA. *Field guide to optical lithography*. Bellingham, Washington, USA: SPIE Press; 2006 Jan 24.
5. Wu B, Kumar A. Extreme ultraviolet lithography: a review. *Journal of Vacuum Science & Technology B*. 2007 Nov 1;25(6):1743-61.
6. Bates FS, Fredrickson GH. *Block copolymers-designer soft materials*. *Physics today*. 2000.

7. Kalra V, Mendez S, Escobedo F, Joo YL. Coarse-grained molecular dynamics simulation on the placement of nanoparticles within symmetric diblock copolymers under shear flow. *The Journal of chemical physics*. 2008 Apr 28;128(16):164909.
8. Hu H, Gopinadhan M, Osuji CO. Directed self-assembly of block copolymers: a tutorial review of strategies for enabling nanotechnology with soft matter. *Soft matter*. 2014;10(22):3867-89.
9. Segalman RA, Schaefer KE, Fredrickson GH, Kramer EJ, Magonov S. Topographic templating of islands and holes in highly asymmetric block copolymer films. *Macromolecules*. 2003 Jun 17;36(12):4498-506.
10. KG AT, Gotrik KW, Hannon AF, Alexander-Katz A, Ross CA, Berggren KK. Templating three-dimensional self-assembled structures in bilayer block copolymer films. *Science*. 2012 Jun 8;336(6086):1294-8.
11. Pinge S, Lin G, Padmanaban M, Baskaran D, Joo YL. Designing an Ordered Template of Cylindrical Arrays based on a Simple Flat Plate Confinement of Block Copolymers: A Coarse-Grained Molecular Dynamics Study. *Soft Matter*. 2017. DOI: 10.1039/C7SM02015E.
12. Cheng JY, Rettner CT, Sanders DP, Kim HC, Hinsberg WD. Dense self-assembly on sparse chemical patterns: Rectifying and multiplying lithographic patterns using block copolymers. *Advanced Materials*. 2008 Aug 18;20(16):3155-8.

13. Kim SO, Solak HH, Stoykovich MP, Ferrier NJ, de Pablo JJ, Nealey PF. Epitaxial self-assembly of block copolymers on lithographically defined nanopatterned substrates. *Nature*. 2003 Jul 24;424(6947):411-4.
14. Liu CC, Han E, Onses MS, Thode CJ, Ji S, Gopalan P, Nealey PF. Fabrication of lithographically defined chemically patterned polymer brushes and mats. *Macromolecules*. 2011 Mar 18;44(7):1876-85.
15. Liu CC, Ramírez-Hernández A, Han E, Craig GS, Tada Y, Yoshida H, Kang H, Ji S, Gopalan P, de Pablo JJ, Nealey PF. Chemical patterns for directed self-assembly of lamellae-forming block copolymers with density multiplication of features. *Macromolecules*. 2013 Feb 11;46(4):1415-24.
16. Liu CC, Nealey PF, Ting YH, Wendt AE. Pattern transfer using poly (styrene-block-methyl methacrylate) copolymer films and reactive ion etching. *Journal of Vacuum Science & Technology B: Microelectronics and Nanometer Structures Processing, Measurement, and Phenomena*. 2007 Nov;25(6):1963-8.
17. Muramatsu M, Iwashita M, Kitano T, Toshima T, Somervell M, Seino Y, Kawamura D, Kanno M, Kobayashi K, Azuma T. Nanopatterning of diblock copolymer directed self-assembly lithography with wet development. *Journal of Micro/Nanolithography, MEMS, and MOEMS*. 2012 Jul 1;11(3):031305-1.

18. Black CT, Guarini KW, Milkove KR, Baker SM, Russell TP, Tuominen MT. Integration of self-assembled diblock copolymers for semiconductor capacitor fabrication. *Applied Physics Letters*. 2001 Jul 16;79(3):409-11.
19. Gharbi A, Tiron R, Pimenta Barros P, Argoud M, Servin I, Chevalier X, Nicolet C, Navarro C. PMMA removal options by wet development in PS-b-PMMA block copolymer for nanolithographic mask fabrication. *Journal of Vacuum Science & Technology B, Nanotechnology and Microelectronics: Materials, Processing, Measurement, and Phenomena*. 2015 Sep;33(5):051602.
20. Baravelli E, Dixit A, Rooyackers R, Jurczak M, Speciale N, De Meyer K. Impact of line-edge roughness on FinFET matching performance. *IEEE Transactions on Electron Devices*. 2007 Sep;54(9):2466-74.
21. Leung G, Lai L, Gupta P, Chui CO. Device-and circuit-level variability caused by line edge roughness for sub-32-nm FinFET technologies. *IEEE Transactions on Electron Devices*. 2012 Aug;59(8):2057-63.
22. Bosse AW, Lin EK, Jones RL, Karim A. Interfacial fluctuations in an ideal block copolymer resist. *Soft Matter*. 2009;5(21):4266-71.
23. Moore GE. Cramming more components onto integrated circuits. *Proceedings of the IEEE*. 1998 Jan;86(1):82-5.

24. Matsen MW, Bates FS. Unifying weak-and strong-segregation block copolymer theories. *Macromolecules*. 1996 Feb 12;29(4):1091-8.
25. Detcheverry FA, Pike DQ, Nagpal U, Nealey PF, de Pablo JJ. Theoretically informed coarse grain simulations of block copolymer melts: method and applications. *Soft Matter*. 2009;5(24):4858-65.
26. Hur SM, Thapar V, Ramírez-Hernández A, Khaira G, Segal-Peretz T, Rincon-Delgadillo PA, Li W, Müller M, Nealey PF, de Pablo JJ. Molecular pathways for defect annihilation in directed self-assembly. *Proceedings of the National Academy of Sciences*. 2015 Nov 17;112(46):14144-9.
27. Hur SM, Khaira GS, Ramírez-Hernández A, Müller M, Nealey PF, de Pablo JJ. Simulation of defect reduction in block copolymer thin films by solvent annealing. *ACS Macro Letters*. 2014 Dec 11;4(1):11-5.
28. Daoulas KC, Müller M, Stoykovich MP, Kang H, de Pablo JJ, Nealey PF. Directed copolymer assembly on chemical substrate patterns: A phenomenological and single-chain-in-mean-field simulations study of the influence of roughness in the substrate pattern. *Langmuir*. 2008 Feb 19;24(4):1284-95.

29. Stoykovich MP, Daoulas KC, Müller M, Kang H, de Pablo JJ, Nealey PF. Remediation of line edge roughness in chemical nanopatterns by the directed assembly of overlying block copolymer films. *Macromolecules*. 2010 Feb 10;43(5):2334-42.
30. Segal-Peretz T, Ren J, Xiong S, Khaira G, Bowen A, Ocola LE, Divan R, Doxastakis M, Ferrier NJ, de Pablo J, Nealey PF. Quantitative three-dimensional characterization of block copolymer directed self-assembly on combined chemical and topographical prepatterned templates. *ACS nano*. 2017 Jan 17;11(2):1307-19.
31. Peters AJ, Lawson RA, Ludovice PJ, Henderson CL. Detailed molecular dynamics studies of block copolymer directed self-assembly: Effect of guiding layer properties. *Journal of Vacuum Science & Technology B, Nanotechnology and Microelectronics: Materials, Processing, Measurement, and Phenomena*. 2013 Nov;31(6):06F302.
32. Peters AJ, Lawson RA, Ludovice PJ, Henderson CL. Effects of block copolymer polydispersity and χ_N on pattern line edge roughness and line width roughness from directed self-assembly of diblock copolymers. *InProc SPIE* 2013 Mar 26 (Vol. 8680, pp. 868020-1).
33. Morita H, Tanaka K, Kajiyama T, Nishi T, Doi M. Study of the glass transition temperature of polymer surface by coarse-grained molecular dynamics simulation. *Macromolecules*. 2006 Sep 5;39(18):6233-7.

34. Kremer K, Grest GS. Dynamics of entangled linear polymer melts: A molecular-dynamics simulation. *The Journal of Chemical Physics*. 1990 Apr 15;92(8):5057-86.
35. Weeks JD, Chandler D, Andersen HC. Role of repulsive forces in determining the equilibrium structure of simple liquids. *The Journal of chemical physics*. 1971 Jun 15;54(12):5237-47.
36. in't Veld PJ, Plimpton SJ, Grest GS. Accurate and efficient methods for modeling colloidal mixtures in an explicit solvent using molecular dynamics. *Computer Physics Communications*. 2008 Sep 1;179(5):320-9
37. Plimpton S. Fast parallel algorithms for short-range molecular dynamics. *Journal of computational physics*. 1995 Mar 1;117(1):1-9.
38. Towns J, Cockerill T, Dahan M, Foster I, Gaither K, Grimshaw A, Hazlewood V, Lathrop S, Lifka D, Peterson GD, Roskies R. XSEDE: accelerating scientific discovery. *Computing in Science & Engineering*. 2014 Sep 1;16(5):62-74

CHAPTER 4

MESOSCALE MODELING OF DIRECTED SELF-ASSEMBLY OF LINE AND SPACE PATTERNS VIA ION-BOMBARDMENT DRY-ETCHING

4.1 INTRODUCTION

In the previous chapter, Liu-Nealey^{1,2} was studied, from the self-assembly phase to subsequent etching using a selective solvent. Etching using a selective etch like acetic acid does offer extremely high selectivity and the consumption of PS is minimal³. It has been more popularly used to remove PMMA for contact hole patterns described in chapter 2 using solvents like acetic acid. For line and space patterns, experiments have observed pattern collapse after solvent evaporation, especially at low solvent conditions due to diverging surface forces³. This leaves the resist unviable for further use to transfer the pattern to the underlying silicon. Moreover, the limited use of wet-etching for contact hole PMMA removal also requires an initial exposure step (193nm or UV) to first degrade the PMMA to prevent redistribution on the PS resist^{4,5}.

Even though dry-etching has substantially lower selectivity, using plasma ions has been preferred over the more economical wet-etching for line and space patterns. This selectivity is ensured from the difference in functional group with styrene having higher amount of carbon content along with an aromatic carbon ring as compared to methylmethacrylate which has an aliphatic base with oxygen functional groups^{6,7}.

Plasma etching involves ion bombardment with a plasma driven gas chemistry⁸. Various plasma etch-chemistries have been tried over the years, but the most popular remain Ar, O₂ and Ar/O₂

chemistries. Recent work has seen CO etch chemistries with higher selectivities than conventional plasma being attempted with good results⁹. The newer etch tools provide the experimentalist with flexibility with the chemistry of the gases as the devices are versatile with lots of functionality. From an academic perspective Ar, O₂, and Ar/O₂ systems remain the best candidates as a model system and these etch chemistries typifies the two popular etching chemistries: ion-bombardment removal for Ar and reactive-ion etching for O₂. The mixtures of these gases will thus follow both these mechanisms depending on the material that is causing the removal. As the optimum ratio of Ar:O₂ in Ar/O₂ is about 10:1 along with a high biased voltage, the dominant mechanism for the mixed etch will still be ion-bombardment⁸.

Lower ion to radical ratio leads to rougher surfaces. Ion bombardment removes PMMA by striking the material with high energy etch ions forming volatile products like CO and CO₂. These volatile products are enhanced by the presence of Ar ions. These ions break bonds on the surface and depolymerizes PMMA leading to high etch rates¹⁰⁻¹². This removal of materials also causes the formation of dangling bonds which has the ability to recombine with newly exposed surface or residual material forming a cross-linked polymer mini-network increasing the etch-resistance to subsequent ion-bombardment. This tendency to cross-link is higher for PS than PMMA and play a crucial role in affecting the surface morphology of the etched material¹²⁻¹⁶. On the other hand, oxygen radical (and ions) reacts with the oxygen groups to chemically remove PMMA. These radicals are often known to form passive inhibition layer as a byproduct. The presence of Ar ion in addition to O₂ radicals help in removal of this inhibition layer¹². Apart from that, these ions also contribute to activation energy of RIE reactions. This difference in mechanism causes reactive-ion etching to have a faster etching rate and with lower selectivity and more isotropy in the etch. Apart

from these reactive mechanisms, roughness amplification effects can also alter the roughness characteristics of the resists. These include: ‘shadowing effect’^{17,18} wherein a disparity exists between the radical and ion concentration in the ‘valleys’ and ‘peaks’ of the surface topography, ‘flux-remission’,^{17,19,20} wherein the ion/radical flux gets deflected by striking on the sidewalls of the resists leading to accumulation on the bottoms, and ‘micro-masking’ which leads to inhomogeneity in the resistance of the surface due to sputtering and subsequent redeposition of materials on the resist surface²¹.

Table 4.1: Comparison of Ar and O₂ etch chemistry

	Ar etching	O₂ etching
Etch bead	Charged Ar ions	O ₂ radicals (and may be Oxygen ions)
Dominant mechanism	Ion bombardment	Reactive-ion etching
Etch rate	Low	High
Selectivity	High	Low
Anisotropy	Lower anisotropic etching	Induces more anisotropic etching

Experimentally, a simplified setup for the etch tool is described in figure 4.1. The substrate is maintained at temperatures lower than ambient (~5 °C) by using a water-cooling system in combination with Helium cryogenics. Ions are accelerated towards substrate in the electric fields of thin ‘sheath’ between the substrate and a radio frequency plasma source. Low pressure conditions are maintained ~ 10 mTorr⁸. The sheath can be thus considered near-collisionless and

the energetic ion can be assumed to strike the surface at a near perpendicular angle. As there are various electronics components involved in the etch-tool there are various transient effects and timing uncertainties. Hence for precise control parameters are optimized so as to achieve fast rate kinetics.

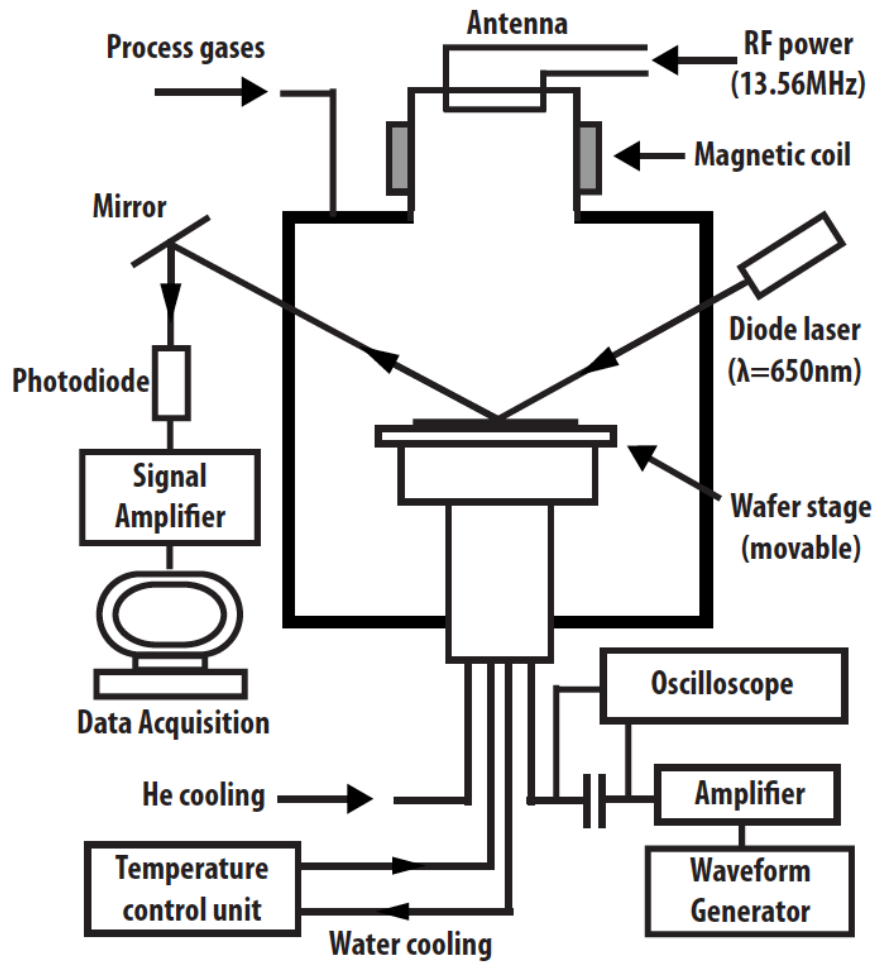


Figure 4.1: Schematic of plasma etcher with interferometry system for etch measurement adapted from Ting *et. al.*

4.2 MODELS AND METHODS

In Chapter 2, the BCP annealing and subsequent cooling has been described in the two process stages *anneal* and *pre-etch*. The BCP trajectory after the *pre-etch* stage is the equilibrium morphology after cooling the system below the glass transition temperature. This morphology is the starting trajectory which is etched via ion-bombardment. Hence, the coarse-graining for the BCP remains the same as described in chapter 3. One coarse-grained PS bead will have 4 PS molecules while PMMA coarse-grained bead has 4.5 PMMA molecules. The reduced mass of these beads is 1 and 1.08 respectively for PS and PMMA. The BCP site density of 0.85 beads / nm³ is maintained which is equivalent to real BCP density of ~ 1.1 g/cc (average of PS and PMMA densities). For model simplicity, the etch bead is assumed to have a same size of 1 nm as the BCP bead. Future version of this model can have added complexity with specific coarse-graining. For a etch gas with fixed chemistry and at a constant temp, the site density is expressed in terms of gas pressure.

$$\frac{PM}{RT} = \rho \quad \text{equation-4.1}$$

P = pressure in mTorr; M = molecular weight of the etch gas; T =temperature in Kelvin.
For ambient temperatures, assuming Argon gas chemistry we have,

$$\rho = 0.00214 P \text{ gcm}^{-3}$$

Scaling with the BCP site density of 0.85 beads/nm³, equivalent to 1.1 g/cc we get a etch gas bead density of 0.00165 P beads /nm³. For the current study, $P = 10, 20,$ and 30 mTorr have been explored.

Two types of etch beads are defined.: PS selective etch bead and PMMA selective etch bead. A bead selective to a BCP block will etch only BCP beads of the particular block and will be immune to the other BCP block beads. Post *pre-etch* process stage, the BCP beads are frozen and the top-

substrate beads are deleted. The box is then re-scaled to increase in size in the positive z direction. Subsequently, in the space above the BCP thin film PS and PMMA selective etch beads are generated. (figure 4.2) These etch beads are provided with a velocity in the z-direction, V_z and they approach the BCP beads. Any BCP bead within a certain etch radii (R_{etch}) of the etch bead can be removed from the simulation box simulating ion-bombardment etching. With increasing time, more of the BCP beads are consumed and lower film thicknesses close to the bottom substrate is exposed to the incoming etch beads. The etching process is stopped when all of the PMMA phase (non-resist) is consumed resulting in a *post-etch* PS resist domains resting on the bottom substrate.

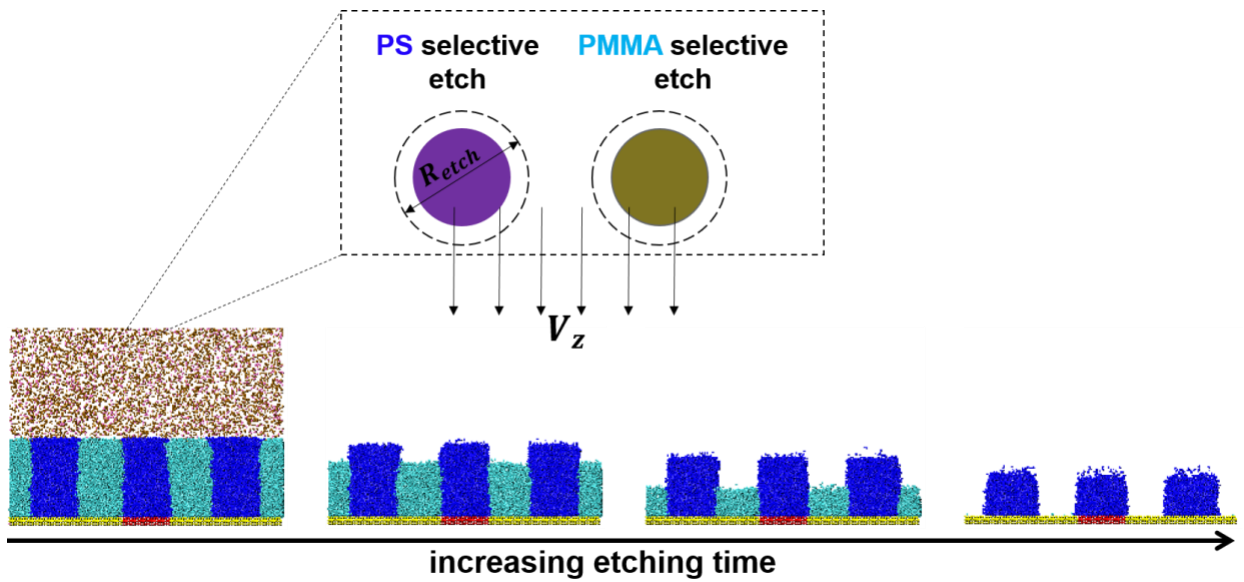


Figure 4.2: Kinetic evolution of resist morphology with PS selective and PMMA selective etch beads. PS selective beads removes PS beads while PMMA selective beads remove PMMA.

4.2.1 Process and simulation parameters

- **Z-Velocity (V_z):** The z-component of the etch velocity is controlled by the ion bombardment energy. The ions are generated by the RF powered etch source and the bias voltage between the source and the substrate. Higher power source will generate etch beads with higher V_z and thus simulations with a higher V_z will correspond to experimental trials with higher bias voltage. It is important to note that the imposed velocity is not equal to the etching rate.
- **Etch rate, r_{etch} :** Nanometers of BCP film removed per unit time.
- **Etch selectivity (S):** The ratio of the etch rate of material A to the etch rate of material B is said to have a selectivity of ‘S’ for material A over material B. It depends on the chemistry of the etch particles, the BCP and the power source. For our study, it is the ratio of the etch rates of non-resist (PMMA) to resist material (PS). For the simulation, we define the etch selectivity as the ratio of number of PMMA-selective etch beads to the PS-selective etch beads.

$$selectivity (S) = \frac{r_{etch-PMMA}}{r_{etch-PS}} = \frac{N_{PMMA-selective\ etch}}{N_{PS-selective\ etch}} \quad \text{equation 4.2}$$

- **Site density (ρ_{etch}):** Etch bead site density expressed in terms of gas. Under constant temperature assumption, it will be proportional to the etch gas pressure.
- **Etch radii (R_{etch}):** extent of etch bead vicinity for BCP removal. Any BCP bead within this radius from the center of mass of the etch bead will be in the list for nearest neighbors.

Although various values have been optimized, the default value chosen is 1.1σ (1.1nm).

- **Frequency of BCP bead removal (f):** A simulation parameter that decides how often nearest neighbor list are built to remove BCP beads in the vicinity of etch beds. The default value chosen is 10 timesteps with each timestep of 0.01 LJ units.
- **Frequency of etch bead removal (Xf):** A simulation parameter that denotes the residence time of the etch bead in the vicinity of BCP beads. It decides how often the etch bead is removed in the vicinity of the R_{etch} . Xf is mechanism dependent. Ion-bombardment will have lower Xf value and reactive ion etching will have a higher value. $Xf=10, 20,$ and 40 timesteps have been attempted with 20 timesteps being the default value.

4.2.2 Interaction potential between etch beads

Etch beads possess high energy and move as near collisionless sheath. As the pressures in the system are in the range of tens of mTorr, this assumption of collisionless sheath is fair. As described in the earlier chapter, we define BCP interactions with hard LJ interactions. For etch beads, a soft cosine potential with a substantially lower energy prefactor is described. The etch beads do not interact as per Van der Waal's interactions and hence are not appropriately defined by LJ potentials. The soft potential essentially prevents any etch bead overlap while maintaining the superimposed V_z .

$$E(r) = \varepsilon \left[1 + \cos \left(\frac{\pi r}{r_c} \right) \right] \quad \text{equation-4.3}$$

$r_c = \text{cutoff radius}$

$\varepsilon = \text{energy prefactor}$

4.3 RESULTS

4.3.1 *Optimizing simulation parameters*

For a fixed V_z , we want V_x and V_y to be of the similar order and have a narrow spread. Higher V_x and V_y will lead to more isotropy in the etching possibly leading to higher roughness. Some of the parameters varied to achieve this narrow velocity spread in x - y include the energy prefactor, ϵ and V_z . In figure 4.3 we see the effect of varying the energy prefactor on the x - y component of the velocity. These trials were performed at $P=10$ mTorr, $f=10$ timesteps and $Xf=20$ timesteps and a fixed $V_z=0.025 \sigma/\tau$ (σ is the reduced distance and τ is the reduced time). The selectivity chosen was substantially high at $S=75$ approaching an ideal etch. For these trials, lower values of ϵ lead to a narrower velocity spread around zero in the x - y direction. This would imply higher anisotropy in the etch possible leading to better roughness values. This is also in line with the general behavior of ion-bombardment etch mechanisms which are known to have higher anisotropy compared to reactive-ion etching mechanisms. These trials were repeated for other V_z and P in the working regime and the same conclusions were drawn as in figure 4.3. $\epsilon = 0.05$ LJ units were chosen as the default value for subsequent trials. Flat plate geometry was the default geometry chosen for the dry-etching trials.

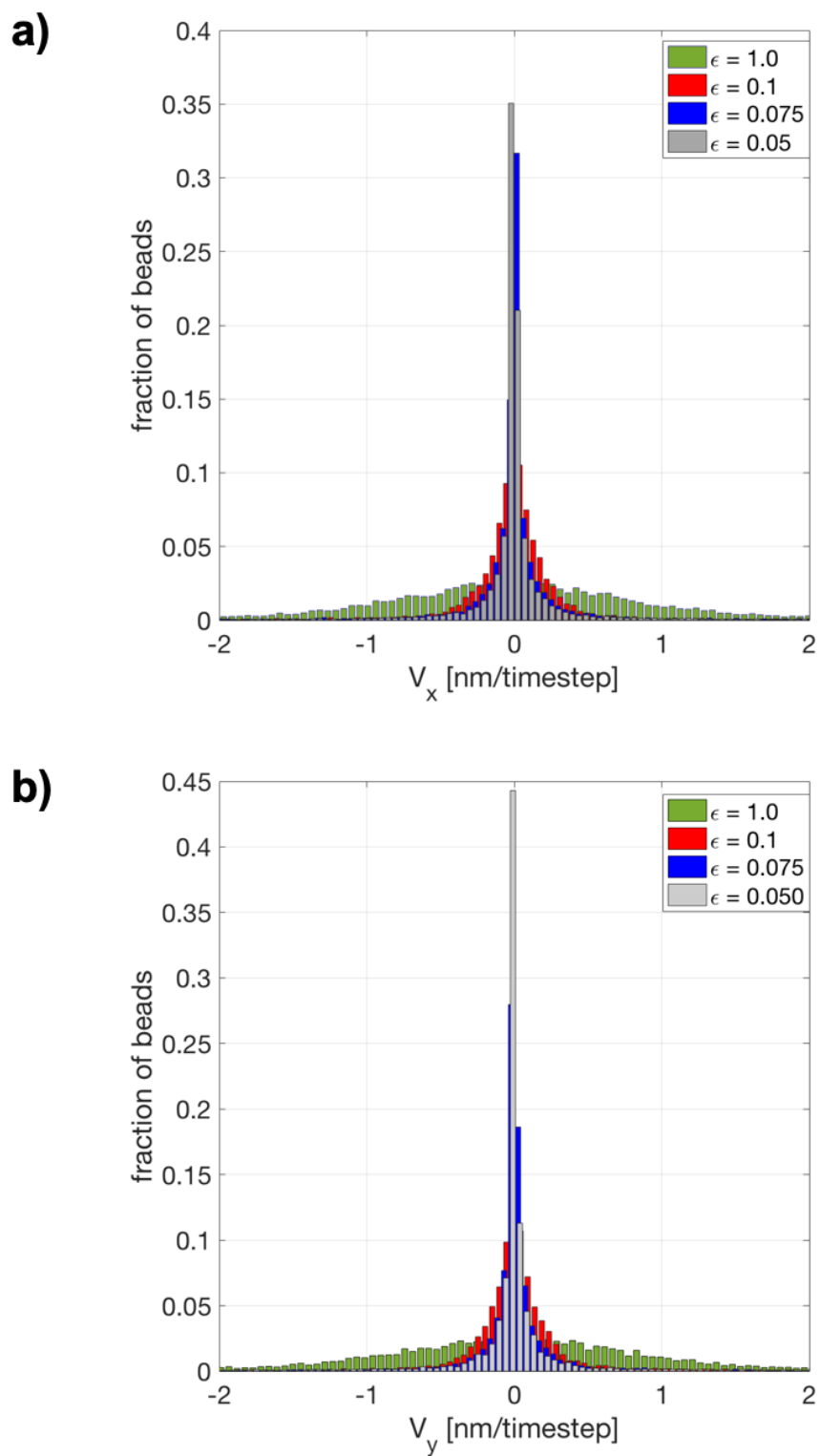


Figure 4.3: Early time velocity distribution for the etch beads for various interaction strengths for the soft-potential. A) x -velocity distribution. B) y -velocity distribution. Z -velocity is constant at $V_z=0.025 \sigma/\tau$.

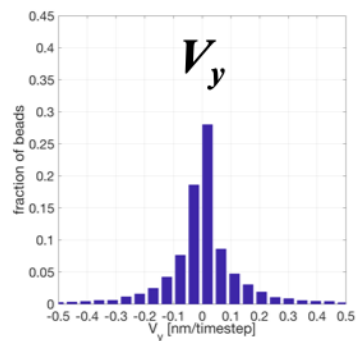
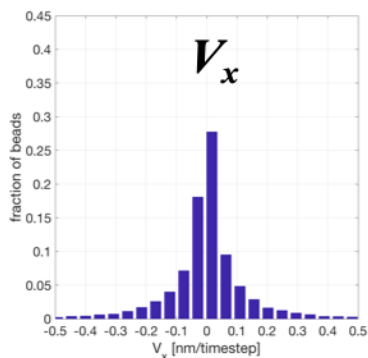
A question that arises from these trials is that what if the interaction between the etch beads were completely turned off by setting $V_x=V_y=0$ for a fixed V_z . This would correspond to a system that moves as a focused sheath of particles generated by a plasma source that are completely collisionless. Although, the x - y velocity spread of these trials were close to a delta function at $V_x=V_y=0$, closer inspection of the BCP trajectory showed deficiencies in the assumption. The bead removal for these trials is not appropriate. The etching is uneven through the film thickness which is unphysical. The resist domains also have holes formed leading to porosity issues. The hole formation was more predominant at higher etch pressure. Hence, we can conclude that completely collisionless etch beads are not ideal but weak interactions between etch beads is desired.

Next, we study the effect of the magnitude of V_z on the x - y velocity spread. The following parameters were kept constant:

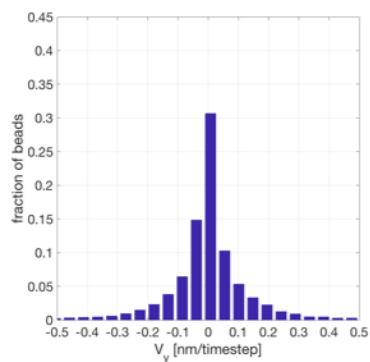
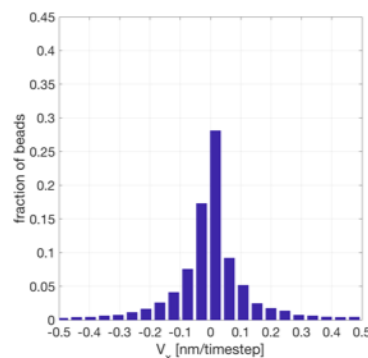
$\epsilon = 0.05$ reduced units ; $P = 10$ mTorr ; $S = 75$ (near ideal etch) ; $Xf = 20$ and $f = 10$

As seen in figure 4.4, higher V_z leads to a narrower spread in the V_x and V_y . This would imply that higher RF power source that results in faster etch beads could possibly lead to lower isotropy in the etch and thus lower roughness.

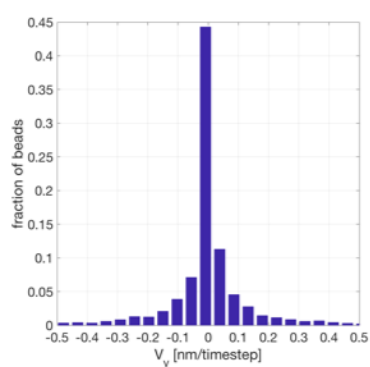
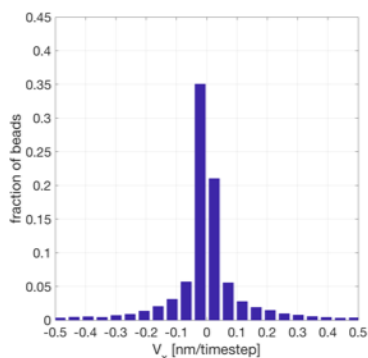
$$V_z = 0.01 \sigma/\tau$$



$$V_z = 0.015 \sigma/\tau$$



$$V_z = 0.025 \sigma/\tau$$



$$V_z = 0.035 \sigma/\tau$$

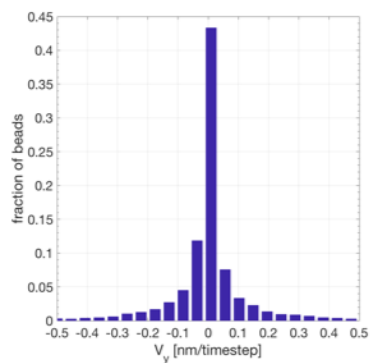
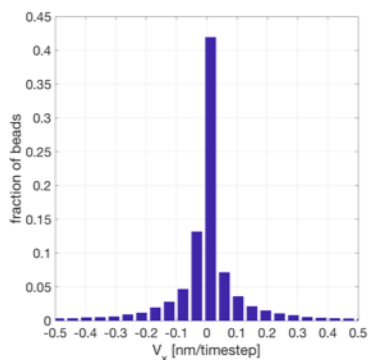


Figure 4.4: Early time x,y -velocity distribution for a constant V_z . Higher velocity spread leads to narrower distribution.

4.3.2 Effect of etch gas pressure

For the optimized V_z and the soft cosine interaction parameters, the effect of etch gas pressure was studied. For a constant $V_z = 0.0075 \sigma/\tau$, default energy prefactor, f and Xf three system pressures ($P=10, 20$, and 30 mTorr) were studied at a realistic etch selectivity of $S=3.5$. The system morphologies at complete PMMA removal is shown in figure 4.5. At higher etch gas pressures ($P=20$ and 30 mTorr) owing to higher etch bead densities, the resist morphology is more porous than at $P=10$ mTorr. A porous etch resist will lead to discrepancies when the pattern is subsequently transferred to the Silicon substrate underneath.

This issue with resist porosity was also observed for these pressures for $S = 1.5$ and 2.5 . $P = 10$ mTorr was chosen as the default pressure for subsequent trials.

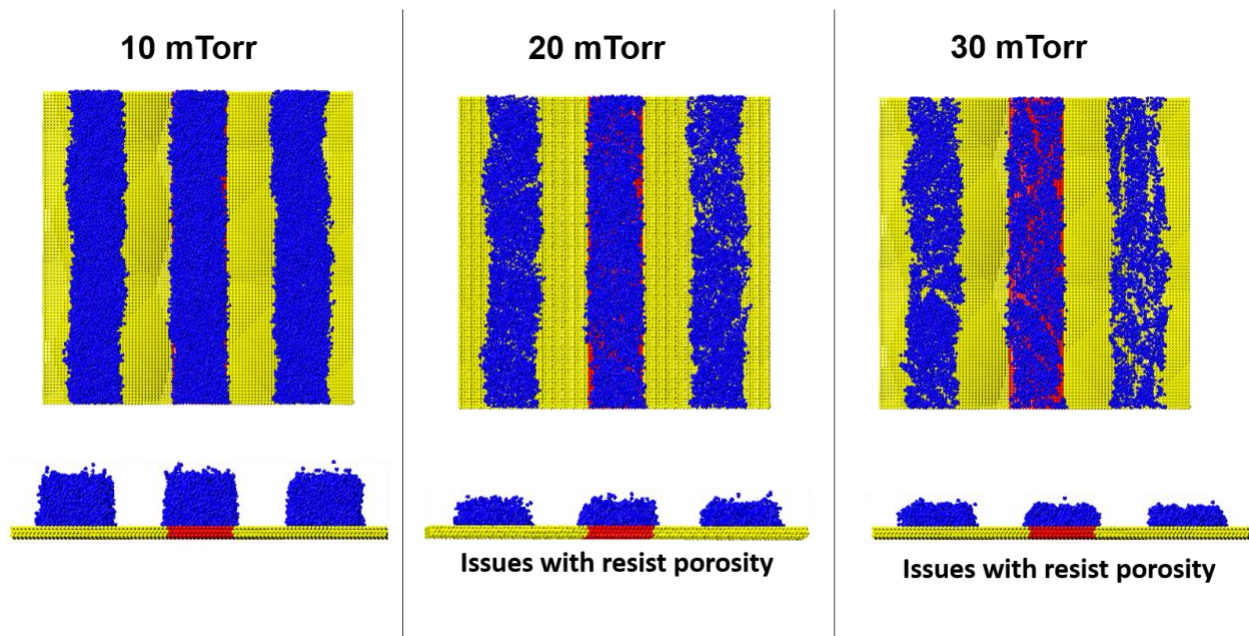


Figure 4.5: Resist morphology at three different etch pressures at a constant $V_z = 0.0075 \sigma/\tau$ and $S=3.5$.

4.3.3 Effect of etch gas selectivity

The selectivity of the etch gas depends on parameters like etch-chemistry, bias voltage source among others. Choosing, the appropriate etch-gas with the optimum selectivity requires a thorough investigation of the *post-etch* chemistry. The *post-etch* resist morphology is evaluated for its effective selectivity, resist height, line-width roughness and line-edge roughness (in space and frequency domains). As we define the simulation selectivity parameter as the ratio of number of PMMA-selective etch beads to PS-selective beads, it is important to find the effective selectivity by measuring the post-etch resist heights after complete PMMA removal. As the film thickness is 28 nm, the effective selectivity can be defined as:

$$S_{eff} = \frac{28 - PMMA_{ht}}{28 - PS_{ht}} \quad \text{equation 4.4}$$

Here, $PMMA_{ht}$ and PS_{ht} are the heights of the two domains at any particular time. In figure 4.6, we explore the kinetic evolution of the system morphology and the effective selectivity associated for the morphology for three different realistic selectivities. The pressure is kept constant at $P=10$ mTorr and $V_z = 0.01 \sigma/\tau$ (default for subsequent trials).

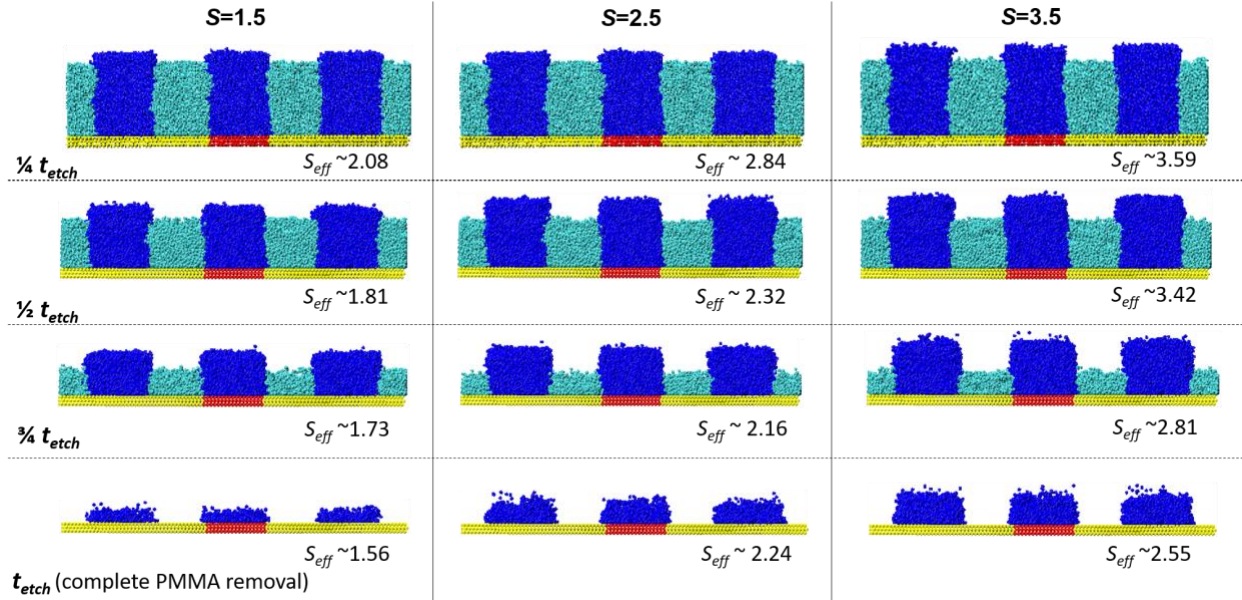


Figure 4.6: Kinetic evolution of resist profile at constant $P=10\text{mTorr}$ and $V_z = 0.01 \sigma/\tau$ at three different selectivities, $S=1.5, 2.5$, and 3.5 . The effective selectivity is calculated by measuring the PS and PMMA domain heights

For the same time, higher initial selectivities, S leads to taller final resist heights at complete PMMA removal. This is expected as the system as a greater number of PMMA-selective beads at the same pressure as compared to PS-selective beads at higher selectivities. The morphology also gives us evidence of the top substrate being abrasive which will be analyzed in subsequent morphology evolution sections. The final effective selectivity, S_{eff} is also lower than initially defined simulation selectivity parameter, S as the ratio of two types of selective etch beads. The instantaneous S_{eff} also decreases with increasing etch time. For lower etch times, $S_{eff} > S$ and as time increases, the effective selectivity falls below initial selectivity for $S = 2.5$ and $S=3.5$ while remain incrementally above initial selectivity for $S=1.5$ (figure 4.7).

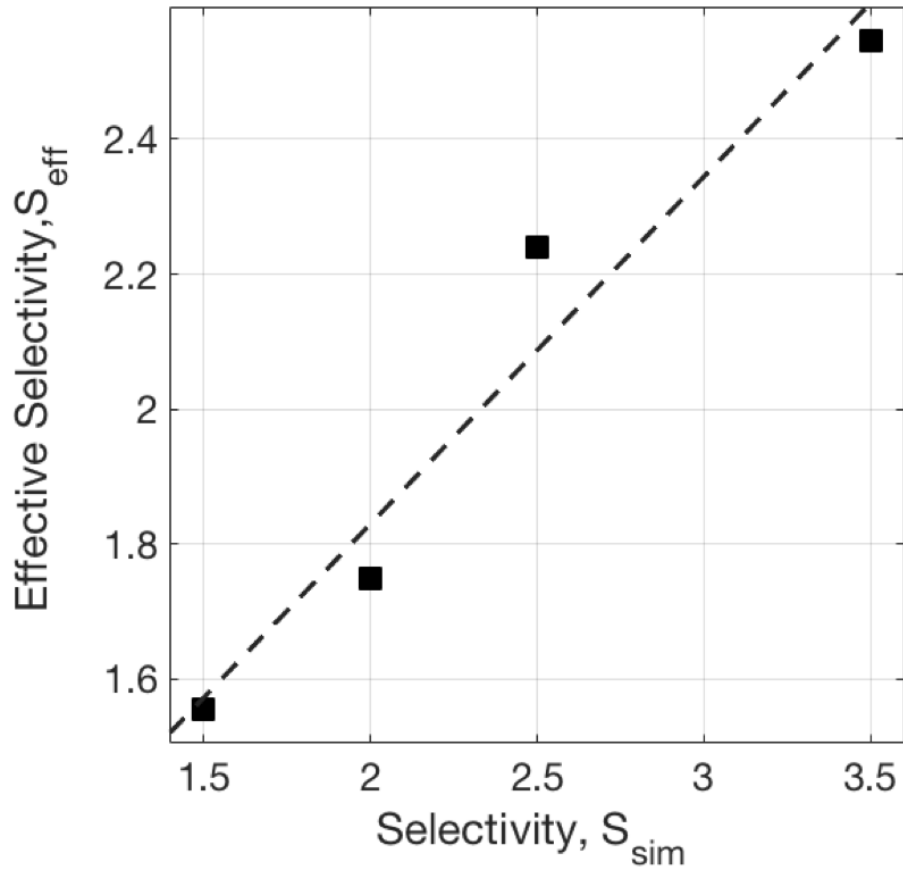


Figure 4.7: Effective selectivity (S_{eff}) calculated at complete PMMA removal as a function of imposed simulation selectivity (S_{sim})

4.3.4 Effect of selectivity on resist morphology

For the realistic selectivities for Ar/O₂ type etches defined earlier, the post etch resist morphology is evaluated at complete PMMA removal. The Line-Width (figure 4.8) and the Line-Edge Roughness (figure 4.9) are plotted as a function of the resist height.

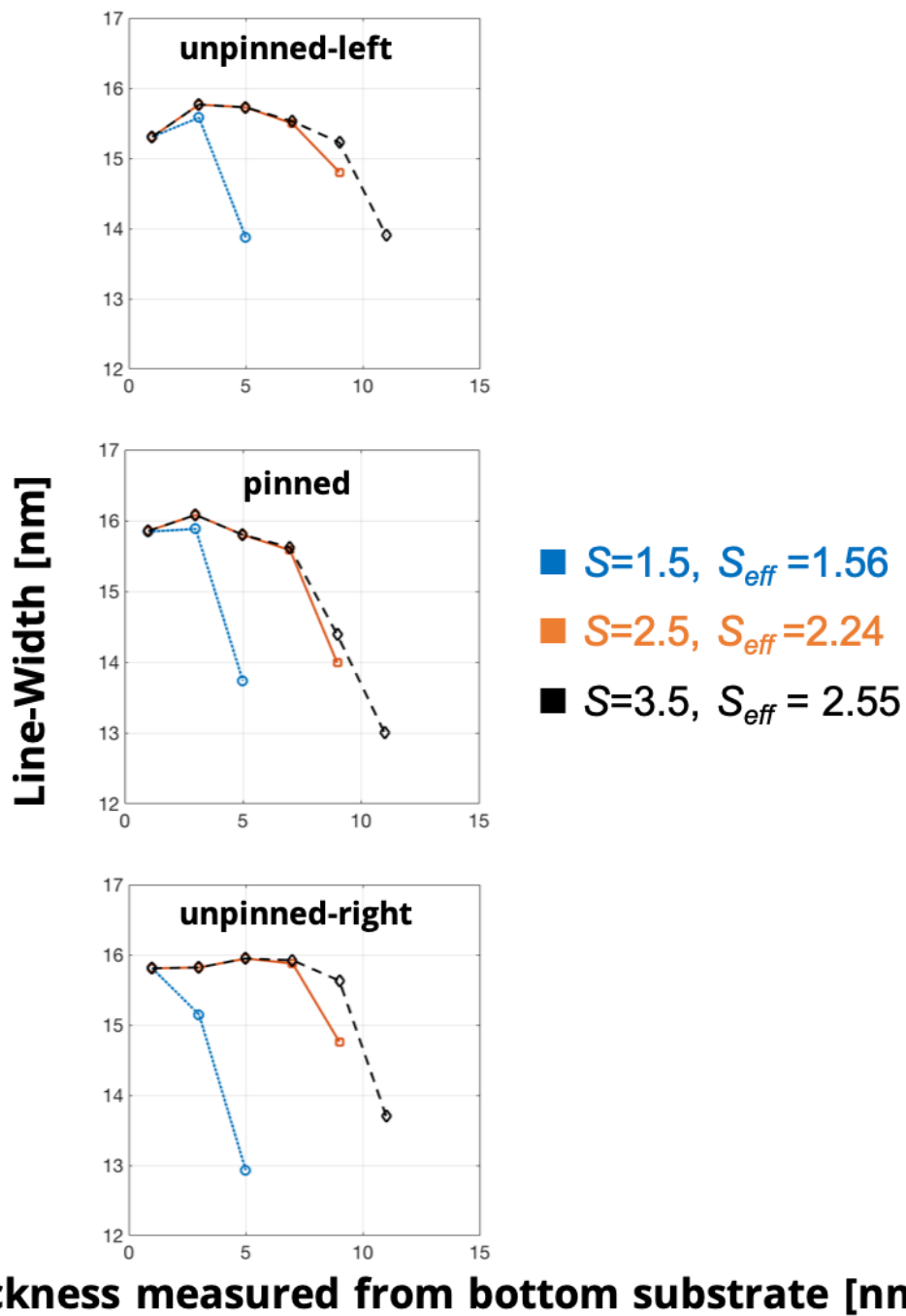


Figure 4.8: Line-Width variation for different etch selectivities. Higher selectivities formed taller resist at complete PMMA removal

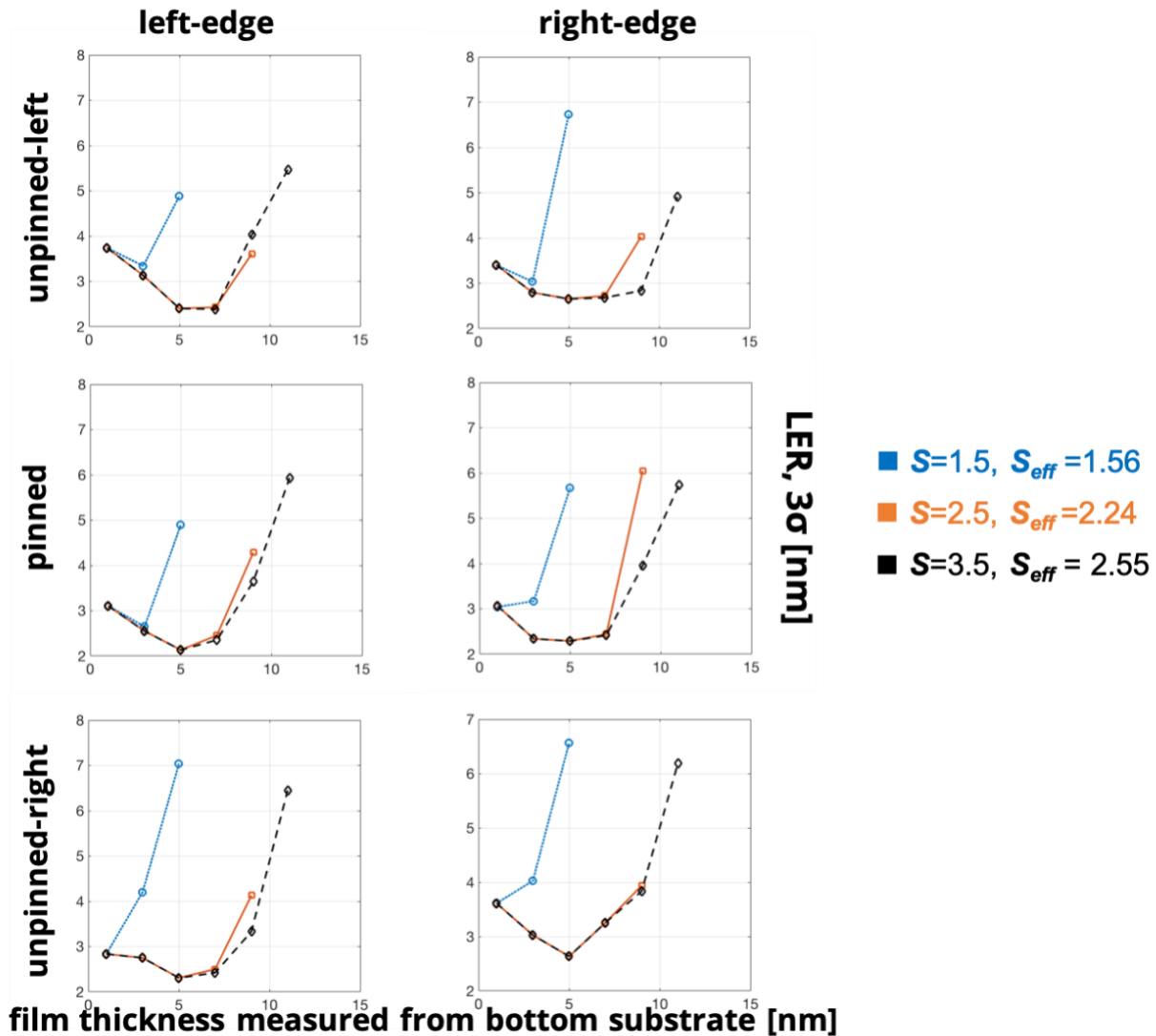


Figure 4.9: LER variation for different etch selectivities for the left and right edge of the three domains. Top surface is abrasive for all selectivities.

Away from the bottom substrate, for higher film thicknesses, the line-width gets lower leading to a gradient in the resist morphology. As seen in the LER vs film thickness plots, the lower line-widths at higher film thicknesses are also rougher. This observation is true for the three selectivities, albeit lower selectivities have lower resist heights. Higher the resist height, greater will be the tolerance for the subsequent pattern transfer to Silicon. It is also important to note that resist morphology of the top-substrate for lower line-widths will not contribute to the subsequent pattern transfers, but the sidewall roughness below the top resist gradient will strongly affect the

Silicon pattern transfer. Thus, for the height averaged LER calculation, the top abrasive substrate is not considered. As $S = 3.5$ leads to a final $S_{eff} = 2.55$, a selectivity reported for the popular Ar/O₂ etch chemistry, we employ $S = 3.5$ for subsequent multi-stage LER comparisons.

4.3.5 Multi-stage LER comparisons

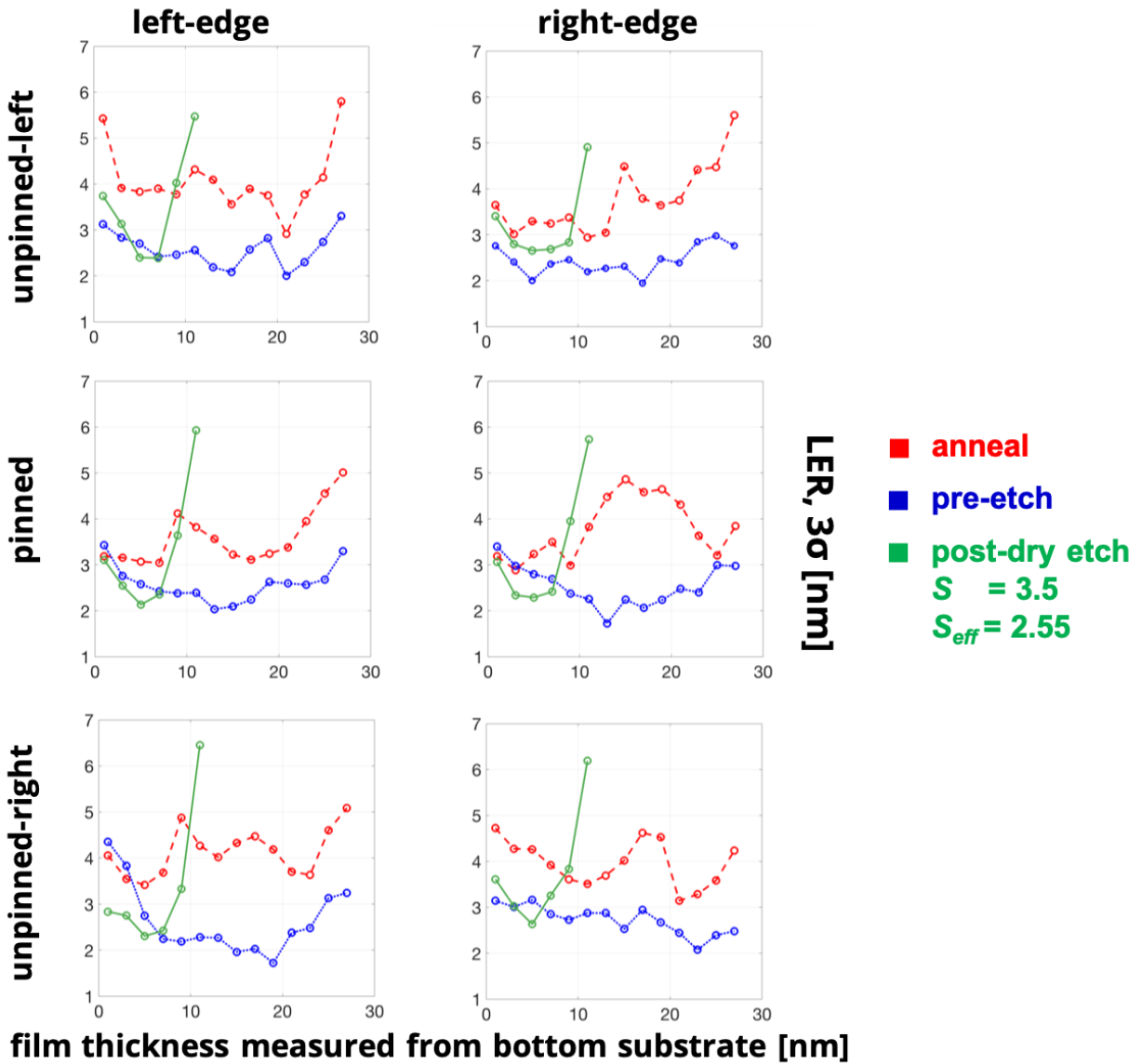


Figure 4.10: LER variation for the three process stages: *anneal*, *pre-etch* and *post-etch* for the left and right edge of the three domains. Top surface is abrasive for the dry-etched resists.

The pre-etch and anneal morphology are the same from chapter 3. As expected from earlier section, the top surface is abrasive as compared to the *anneal* and *pre-etch* morphologies. The resist height is also lower *post-etch*. As evident from figure 4.10 and figure 4.11, the height averaged LER is highest for the *anneal* stage. Dry-etching after cooling the system below glass transition lowers the LER. The sidewall roughness *post-dry etch* leads to increase in the roughness with a $\langle \text{LER} \rangle_{ht} = 2.93$ nm. This is in contrast to the solvent etching $\langle \text{LER} \rangle$ in the previous trial which was almost same in magnitude with the *pre-etch* value.

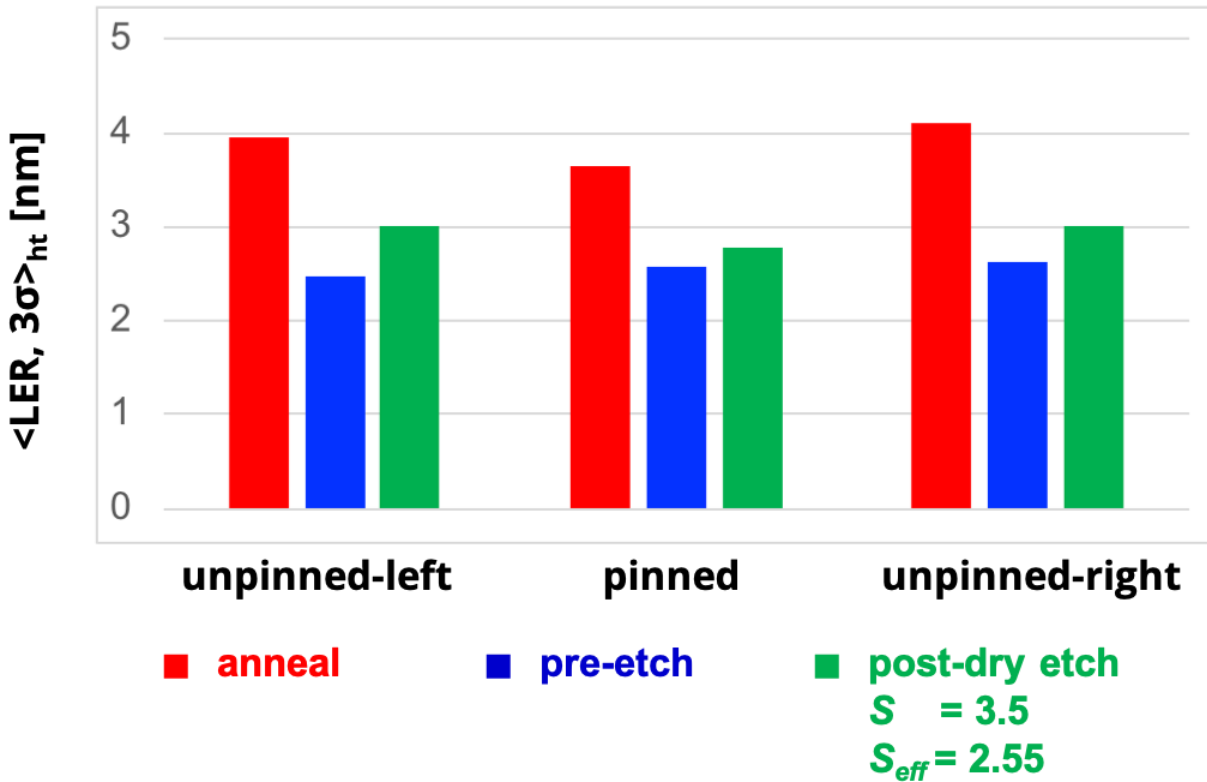


Figure 4.11: Height averaged LER comparison for the three domains for the three process stages: *anneal*, *pre-etch* and *post-dry etch*. *Anneal* phase has the highest average LER followed by *post-dry etch* and then *pre-etch*.

Even though this magnitude was similar in magnitude, the power spectral density showed higher contribution for low frequencies for post-solvent etch and higher contribution for high frequencies for pre-etch morphologies. This observation is not true for the post-dry etch morphology power

spectral density as seen in figure 4.12. The order followed in the space domain holds true in the frequency domain. On average, $PSD_{\text{anneal}} > PSD_{\text{post-etch}} > PSD_{\text{pre-etch}}$.

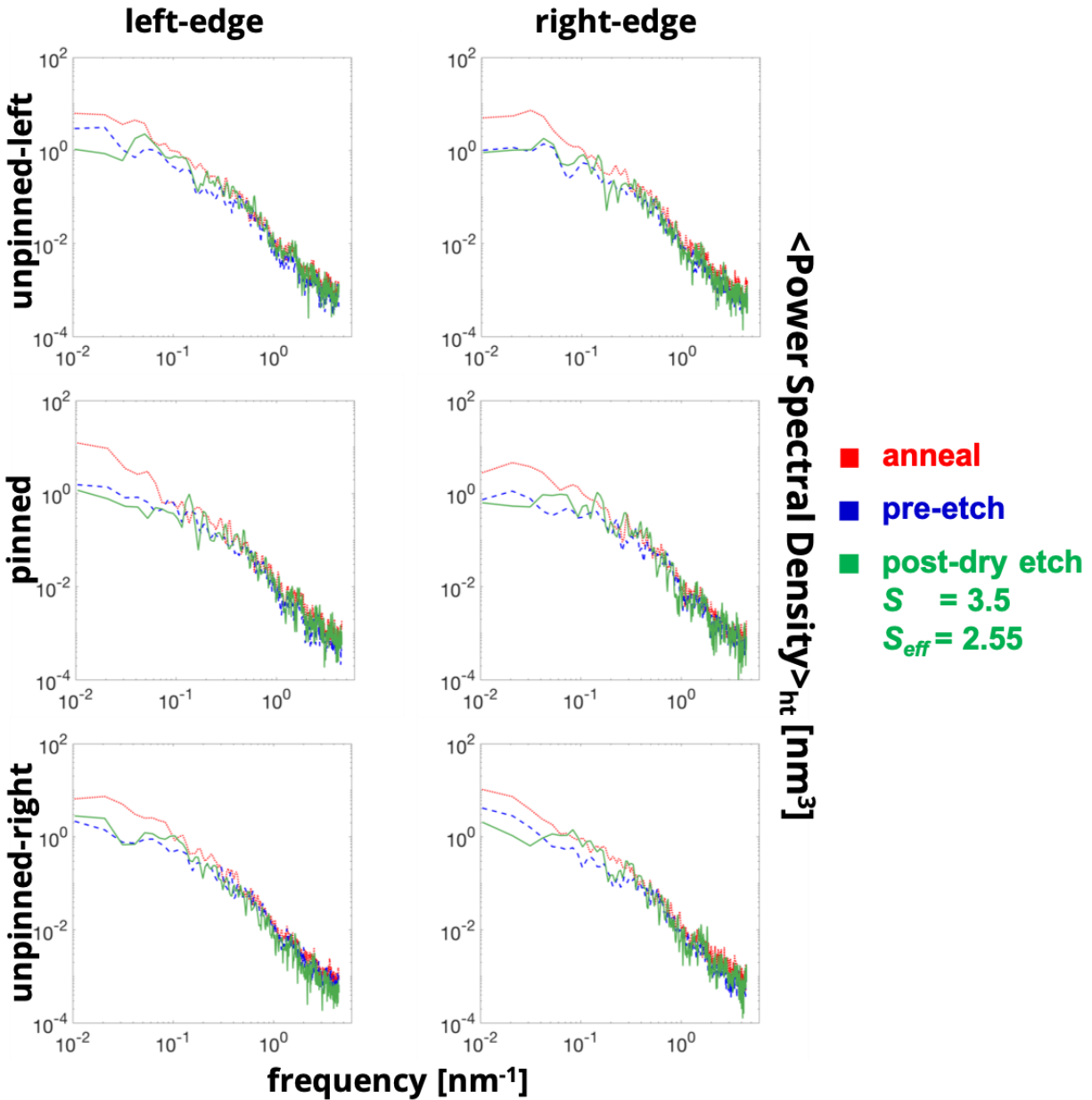


Figure 4.12: Power-spectral density plots for the three process stages. PSD follows the same order as the average LER magnitude with $PSD_{\text{anneal}} > PSD_{\text{post-etch}} > PSD_{\text{pre-etch}}$.

4.3.6 *Dry-etching for substrate with topography*

The dry-etching trials described in the earlier section have been performed on a flat substrate. These trials were repeated for a substrate with topography at $V_z = 0.01 \sigma/\tau$ and $P = 10$ mTorr and $S = 2.5$. The morphology at five different times is seen in figure 4.13. At higher etch times, the topography caused by the pinning leads to incomplete PMMA removal. The etching is assumed to be completed in figure 4.13, $t_{etch} \sim 100\%$. If the etching is carried out further, the residual PMMA will be removed but it will also lead to further depletion in the final resist height. This is especially an issue for the pinned domain. Experimentally, the etching tool has a sensor for the outgassed material. When the sensor detects any Si material, the etching is stopped. To reach the Si compounded substrate, the etch will first have to remove the neutral brushing leading to further loss in resist height. Hence, as an experimentalist calibration of the etch tool and the BCP system is essential to optimize the etching time so as to stop the etching prior to consumption of the neutral brushing. The removal of the substrate (neutral brush) is outside the purview of this study and is not explored leading to issues near substrate gradient.

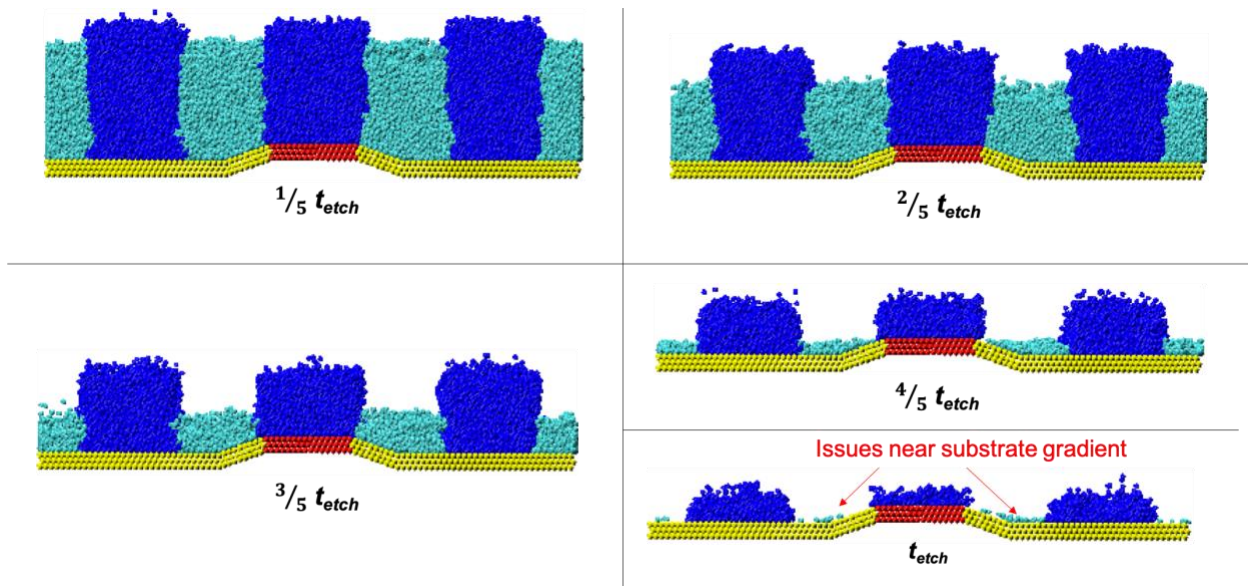


Figure 4.13: Kinetic evolution of a resist for a substrate with topography. $P=10\text{m Torr}$, $V_z = 0.01 \sigma/\tau$ and $S=2.5$. Close to t_{etch} , PMMA is not completely removed near patterned line gradient.

4.3.7 Model validation

Lastly, as in the previous chapter the height averaged roughness values are compared with the experimental SEM images from equivalent trials. The SEM image used, the methodology for image processing and edge detection has been described in chapter 3. The dry-etch model holds in close agreement with the LER values obtained from the experiments. Although the LWR values are slightly higher, it performs slightly better than the solvent etching model. Considering the fact that these simulations are Coarse-Grained with a coarse-graining of 1 nm, under the various assumption of dry-etching, the sufficiently close agreement are encouraging results. This model can be further improved upon by accounting for cross-linking of the PS surface upon interaction with the etch-beads. This will especially help in smoothening out the abrasive top surface. Other possible improvements in the model include account for Oxygen radicals by incorporating reactive-ion etching in addition to the current ion-bombardment mechanism.

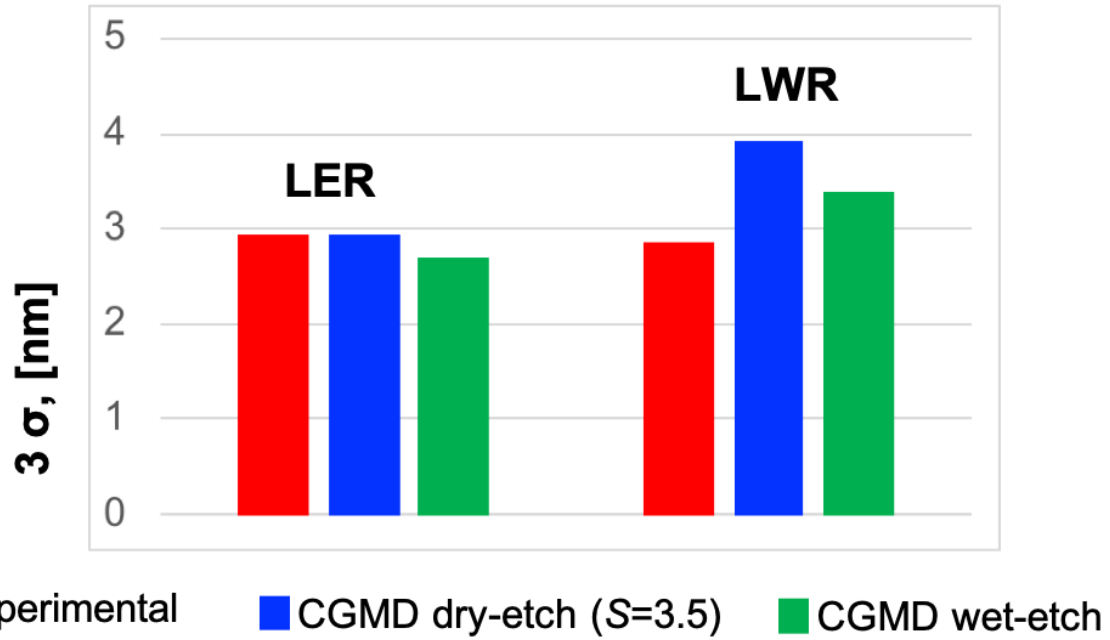


Figure 4.14: Model validation by comparing the experimental SEM image roughness values with CGMD dry-etch and CGMD wet-etch from chapter 3.

4.4 SUMMARY

A dry-etching model has been developed to study the removal of PMMA. Two types of etch beads are defined that consumes each of the BCP phases. Parameters like etch bead z-velocity, etch selectivity, etch gas pressure, etch bead interaction strength, frequency of BCP/etch bead removal are optimized. A soft cosine pair-wise potential defines the inter-etch bead interaction. Stronger the energy prefactor higher was the spread in the V_x and V_y , possibly leading to a more isotropic etch. Making the etch completely anisotropic by reducing the V_x and V_y to zero leads to defective etching with incomplete PMMA removal. For the different etch gas pressures attempted, $P = 20$ and 30 mTorr lead to issues with etch porosity. Hence, $P=10$ mTorr was chosen for subsequent trials. Three etch gas selectivities were studied and the kinetic evolution and instantaneous effective selectivity was assessed. For the three selectivities, the resist morphology was studied by evaluating the line-width and line edge roughness over the film thickness. Subsequently, a multi-stage roughness evaluation was performed at *anneal*, *pre-etch* and *post-etch* stages of the process. The roughness magnitude was highest in the *anneal* stage followed by *post-etch* and *pre-etch*. This observation was also true on average in the frequency domain for both low and high frequencies. The trials were also performed on a substrate with topography highlighting issues near the substrate gradient close to $t_{etch} = 100\%$. Finally, the height averaged sidewall roughness was compared to values obtained from experimental SEM images.

4.5 REFERENCES

1. Liu CC, Han E, Onses MS, Thode CJ, Ji S, Gopalan P, Nealey PF. Fabrication of lithographically defined chemically patterned polymer brushes and mats. *Macromolecules*. 2011 Mar 18;44(7):1876-85.
2. Liu CC, Ramírez-Hernández A, Han E, Craig GS, Tada Y, Yoshida H, Kang H, Ji S, Gopalan P, de Pablo JJ, Nealey PF. Chemical patterns for directed self-assembly of lamellae-forming block copolymers with density multiplication of features. *Macromolecules*. 2013 Feb 11;46(4):1415-24.
3. Barros PP, Barnola S, Gharbi A, Argoud M, Servin I, Tiron R, Chevalier X, Navarro C, Nicolet C, Lapeyre C, Monget C. Etch challenges for DSA implementation in CMOS via patterning. In *Advanced Etch Technology for Nanopatterning III* 2014 Mar 28 (Vol. 9054, p. 90540G). International Society for Optics and Photonics.
4. Tiron R, Gharbi A, Argoud M, Chevalier X, Belledent J, Barros PP, Servin I, Navarro C, Cunge G, Barnola S, Pain L. The potential of block copolymer's directed self-assembly for contact hole shrink and contact multiplication. In *Alternative Lithographic Technologies V* 2013 Mar 26 (Vol. 8680, p. 868012). International Society for Optics and Photonics.
5. Chevolleau T, Cunge G, Delalande M, Chevalier X, Tiron R, David S, Darnon M, Navarro C. Self-assembly patterning using block copolymer for advanced CMOS technology: optimisation of plasma etching process. In *Advanced Etch Technology for Nanopatterning 2012* Mar 17 (Vol. 8328, p. 83280M). International Society for Optics and Photonics.

6. Gokan H, Esho S, Ohnishi Y. Dry etch resistance of organic materials. *Journal of the electrochemical Society*. 1983 Jan 1;130(1):143-6.
7. Oehrlein GS, Phaneuf RJ, Graves DB. Plasma-polymer interactions: A review of progress in understanding polymer resist mask durability during plasma etching for nanoscale fabrication. *Journal of Vacuum Science & Technology B, Nanotechnology and Microelectronics: Materials, Processing, Measurement, and Phenomena*. 2011 Jan 14;29(1):010801.
8. Ting YH, Park SM, Liu CC, Liu X, Himpfel FJ, Nealey PF, Wendt AE. Plasma etch removal of poly (methyl methacrylate) in block copolymer lithography. *Journal of Vacuum Science & Technology B: Microelectronics and Nanometer Structures Processing, Measurement, and Phenomena*. 2008 Sep;26(5):1684-9.
9. Omura M, Imamura T, Yamamoto H, Sakai I, Hayashi H. Highly selective etch gas chemistry design for precise DSAL dry development process. In *Advanced Etch Technology for Nanopatterning III* 2014 Mar 28 (Vol. 9054, p. 905409). International Society for Optics and Photonics.
10. Chung TY, Nest D, Graves DB, Weirnboeck F, Bruce RL, Oehrlein GS, Wang D, Li M, Hudson EA. Electron, ion and vacuum ultraviolet photon effects in 193 nm photoresist surface roughening. *Journal of physics D: Applied physics*. 2010 Jun 21;43(27):272001.

11. Nest D, Chung TY, Vegh JJ, Graves DB, Bruce RL, Lin T, Phaneuf RJ, Oehrlein GS, Long BK, Willson CG. Role of polymer structure and ceiling temperature in polymer roughening and degradation during plasma processing: a beam system study of P4MS and P α MS. *Journal of Physics D: Applied Physics*. 2010 Feb 12;43(8):085204.
12. Ting YH, Liu CC, Park SM, Jiang H, Nealey PF, Wendt AE. Surface roughening of polystyrene and poly (methyl methacrylate) in Ar/O₂ plasma etching. *Polymers*. 2010 Dec 2;2(4):649-63.
13. Zekonyte J, Zaporojtchenko V, Faupel F. Investigation of the drastic change in the sputter rate of polymers at low ion fluence. *Nuclear Instruments and Methods in Physics Research Section B: Beam Interactions with Materials and Atoms*. 2005 Jul 1;236(1-4):241-8.
14. Zaporojtchenko V, Zekonyte J, Faupel F. Effects of ion beam treatment on atomic and macroscopic adhesion of copper to different polymer materials. *Nuclear Instruments and Methods in Physics Research Section B: Beam Interactions with Materials and Atoms*. 2007 Dec 1;265(1):139-45.
15. Sumiya M, Bruce R, Engelmann S, Weilnboeck F, Oehrlein GS. Study of 193 nm photoresist degradation during short time fluorocarbon plasma exposure. I. Studies of modified layer formation. *Journal of Vacuum Science & Technology B: Microelectronics and Nanometer Structures Processing, Measurement, and Phenomena*. 2008 Sep;26(5):1637-46.

16. Sumiya M, Bruce R, Engelmann S, Weilnboeck F, Oehrlein GS. Study of 193 nm photoresist degradation during short time fluorocarbon plasma exposures. II. Plasma parameter trends for photoresist degradation. *Journal of Vacuum Science & Technology B: Microelectronics and Nanometer Structures Processing, Measurement, and Phenomena*. 2008 Sep;26(5):1647-53.
17. Drotar JT, Zhao YP, Lu TM, Wang GC. Surface roughening in shadowing growth and etching in 2+ 1 dimensions. *Physical Review B*. 2000 Jul 15;62(3):2118.
18. Hunt AW, Orme C, Williams DR, Orr BG, Sander LM. Instabilities in MBE growth. *EPL (Europhysics Letters)*. 1994 Sep 10;27(8):611.
19. Drotar JT, Zhao YP, Lu TM, Wang GC. Mechanisms for plasma and reactive ion etch-front roughening. *Physical Review B*. 2000 Jan 15;61(4):3012.
20. Zhao YP, Drotar JT, Wang GC, Lu TM. Roughening in plasma etch fronts of Si (100). *Physical review letters*. 1999 Jun 14;82(24):4882.
21. Gogolides E, Boukouras C, Kokkoris G, Brani O, Tserepi A, Constantoudis V. Si etching in high-density SF₆ plasmas for microfabrication: surface roughness formation. *Microelectronic engineering*. 2004 Jun 1;73:312-8.

CHAPTER 5

BCP FORMULATION VARIATION: EFFECT ON ROUGHNESS AND DEFECTIVITY

In this chapter, simulations were performed to optimize the line and space patterns formed in chapter 3 and chapter 4. Two of the main issues for DSA with LiNe flow are high defectivity and LER values higher than competing technologies. In chapter 3-4, DSA LiNe flow for a monodispersed PS-*b*-PMMA of molecular weight 26,000-*b*-26,000 gmol⁻¹ was studied. Subsequently, the edge roughness analysis *pre-and-post* wet/dry etch was evaluated. In the first part of this chapter we study the effect of using a BCP with a bimodal distribution for the molecular weight, essentially a blend of two BCPs with the same average molecular weight as the BCP in chapter 3 and chapter 4. The blend morphology is evaluated for LiNe edge roughness as well as its tendency form defects as compared to a single BCP system. Next, systems that form defects are studied further by incorporating small fractions of homopolymers in the monodispersed BCP mixture. The effect of dry-etching on the defects are also analyzed. In the last part of this chapter, the effect of addition of oligomeric additives is studied.

5.1 BCP BLENDS: EFFECT ON EDGE ROUGHNESS

One of the most popular methods used for BCP synthesis by polymer chemists is anionic polymerization. Although, the control on polydispersity is substantially better than competing methods, obtaining completely monodispersed polymers is quite rare. The average molecular weight is offset too many a times. This can be a major issue for DSA applications where the line spacing is strongly affected by domain size and the BCP average molecular weight. A get around

used by manufacturers is to use blends of different BCPs such that the average molecular weight of the blend and the BCP spacing is the targeted value. It is thus important to know the effect of these blends on edge roughness and its ability to form defect free structures as compared to the monodispersed BCP. To blend schemes of average molecular weight 26,000-*b*-26,000 have been studied along with the default monodispersed scheme-1.

Scheme 1 (default), PS-*b*-PMMA: 26,000-*b*-26,000 gmol⁻¹, N121 (100 %)

Scheme 2, PS-*b*-PMMA: 28,000-*b*-28,000 gmol⁻¹, N129 (50 %) and 24,000-*b*-24,000 gmol⁻¹ N112 (50%)

Scheme 3, PS-*b*-PMMA: 30,000-*b*-30,000 gmol⁻¹, N139 (50 %) and 22,000-*b*-22,000 gmol⁻¹ , N102 (50%)

For better fundamental understanding, it is important to analyze the distribution of the two blends, both at a higher temperature during anneal and at a lower *pre-etch* cooled temperature. As seen in figure 5.1, the interfacial BCP width is higher for the anneal phase for the blends and the BCP domains have a higher spread at higher temperature. More interestingly, it is observed that the lower molecular weight BCP has a slight preference to self-assemble at the domain edge (BCP interface) as opposed to the higher molecular weight that prefers domain centers.

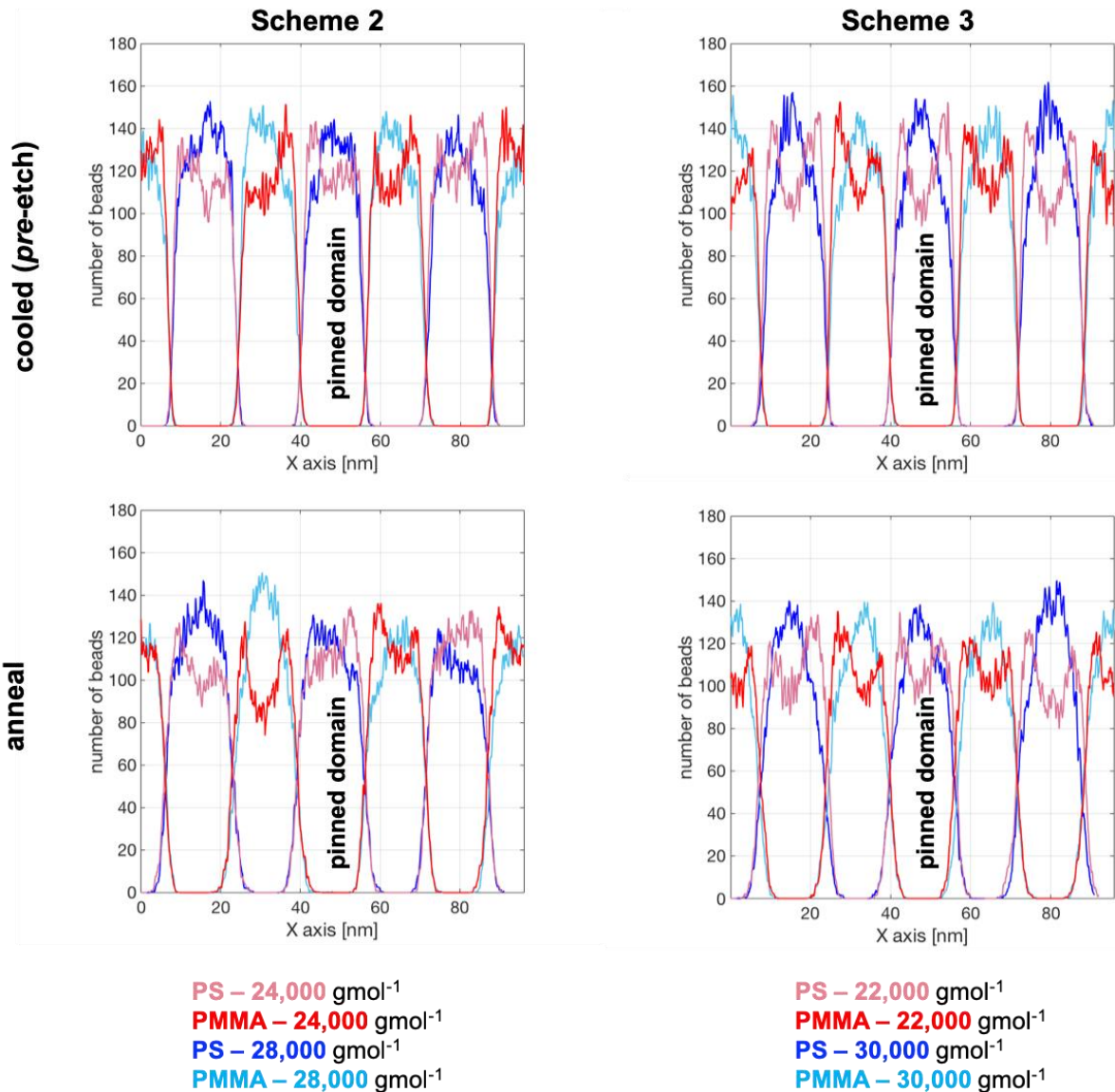


Figure 5.1: Concentration plots for scheme-2 on left and scheme-3 on right for the anneal and pre-etch process stage. Lower molecular weights have a preference to self-assemble near the domain edge while higher molecular weight prefers the domain centers

This preference is more prominent for scheme-3 in which the difference in the molecular weight of the two blend components is higher than scheme-2. This arrangement of the two blends can be explained by entropic constraints that are imposed on the lower chain lengths. The chains want to remain in less stretched state. Hence the lower chain lengths will prefer to be near the edge close

to the covalently bonded BCP from the neighboring domain reducing the chain stretching. The higher chain length can thus move to the center of the domain as it will be stretched lesser than its counterpart thus leading to the lowest free energy state for the system.

As the concentration spread for the components of the blends is realized, it is still important to understand how the blend changes the BCP morphology, including the edge profile. In figure 5.2, the Line-Width and LWR is plotted against the film thickness for the two-blend Scheme-2 and Scheme-3 and compared with default Scheme-1. The gradient is higher for the blends for the pinned domain as seen in the Line-Width plots. The average Line-Width is not fairly different for the three schemes. A small distinction can be made at the extremities of the domains, with scheme-1 being rougher on average near the bottom substrate. The preference for scheme-1 to spread on the bottom substrate is more noticeable in the LER plots (figure 3), thus leading to rougher resists near the bottom substrate.

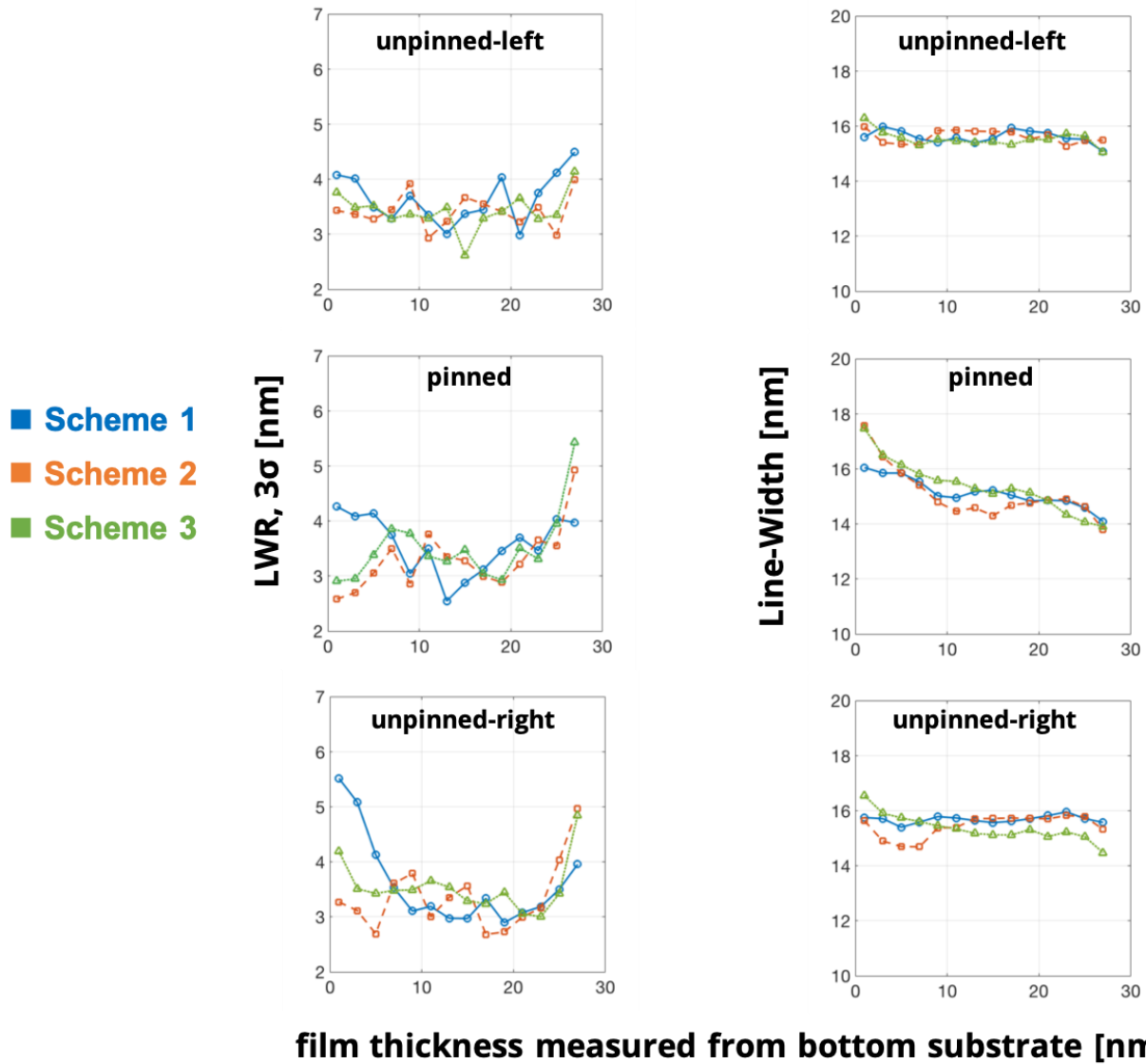


Figure 5.2: Line-Width Roughness (LWR) and Line-Width vs film thickness for the two blends, scheme-2 and scheme-3 compared to the scheme-1 in default. BCP blends have a slight gradient in the Line-Width especially for the pinned domain.

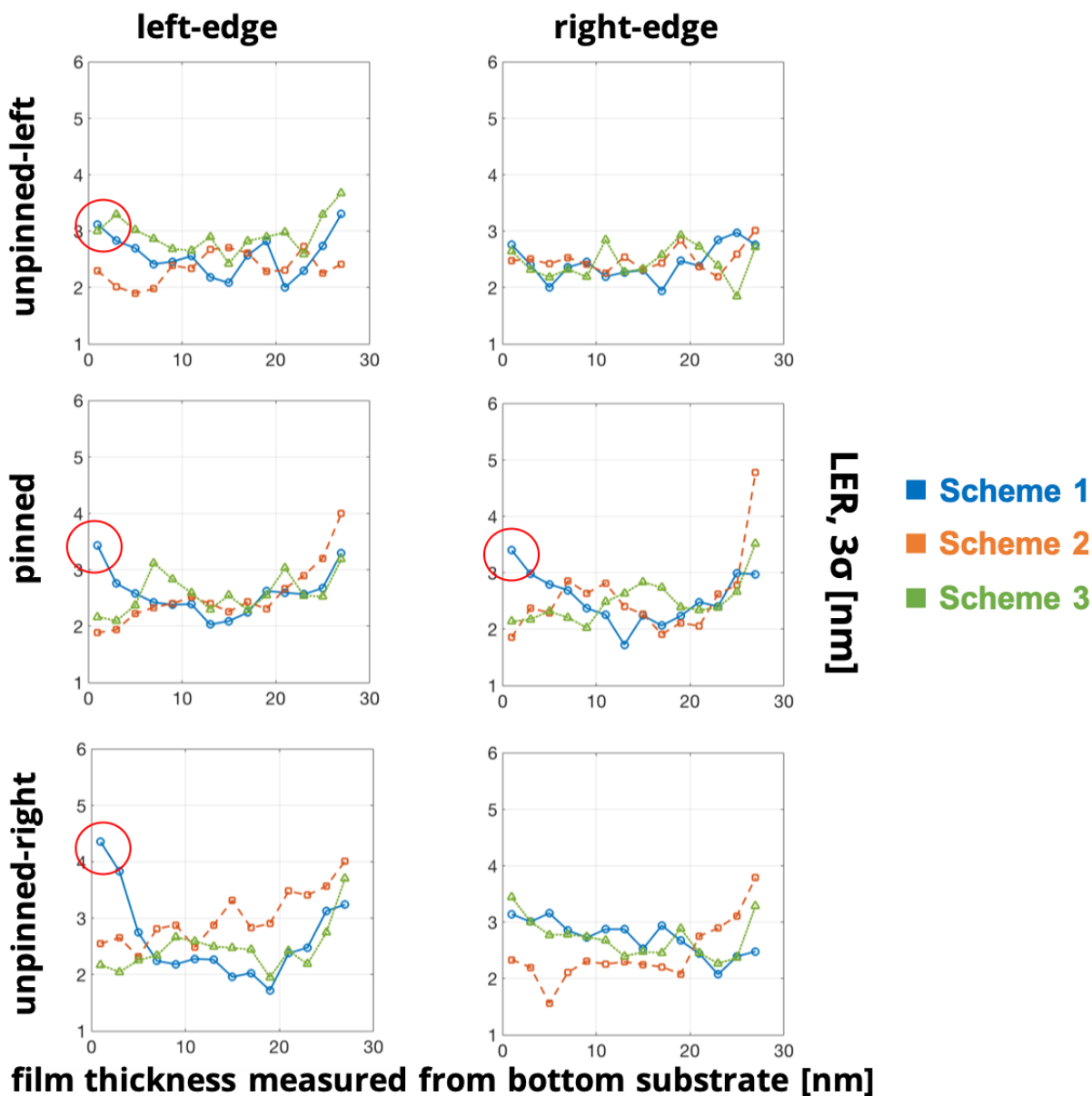


Figure 5.3: Line-Edge Roughness vs film thickness for the left and right edges for the three resist domains for the BCP blends: scheme-2 and scheme-3 compared with the default scheme-1. Non-blend Line-flow have more roughness at the bottom substrate

These deviations we see in the morphology are minor and not that significant to the default trials.

The average roughness bar graphs seen in figure 5.4 a-b, further confirm the fact the blends of similar average molecular weights do not strongly affect average roughness for the molecular weights studied. Thus, the strategy employed by chemists, including our collaborators, of using

blends of known molecular weights such that the BCP period of the blend matches the target seems to be unhindered from a roughness perspective.

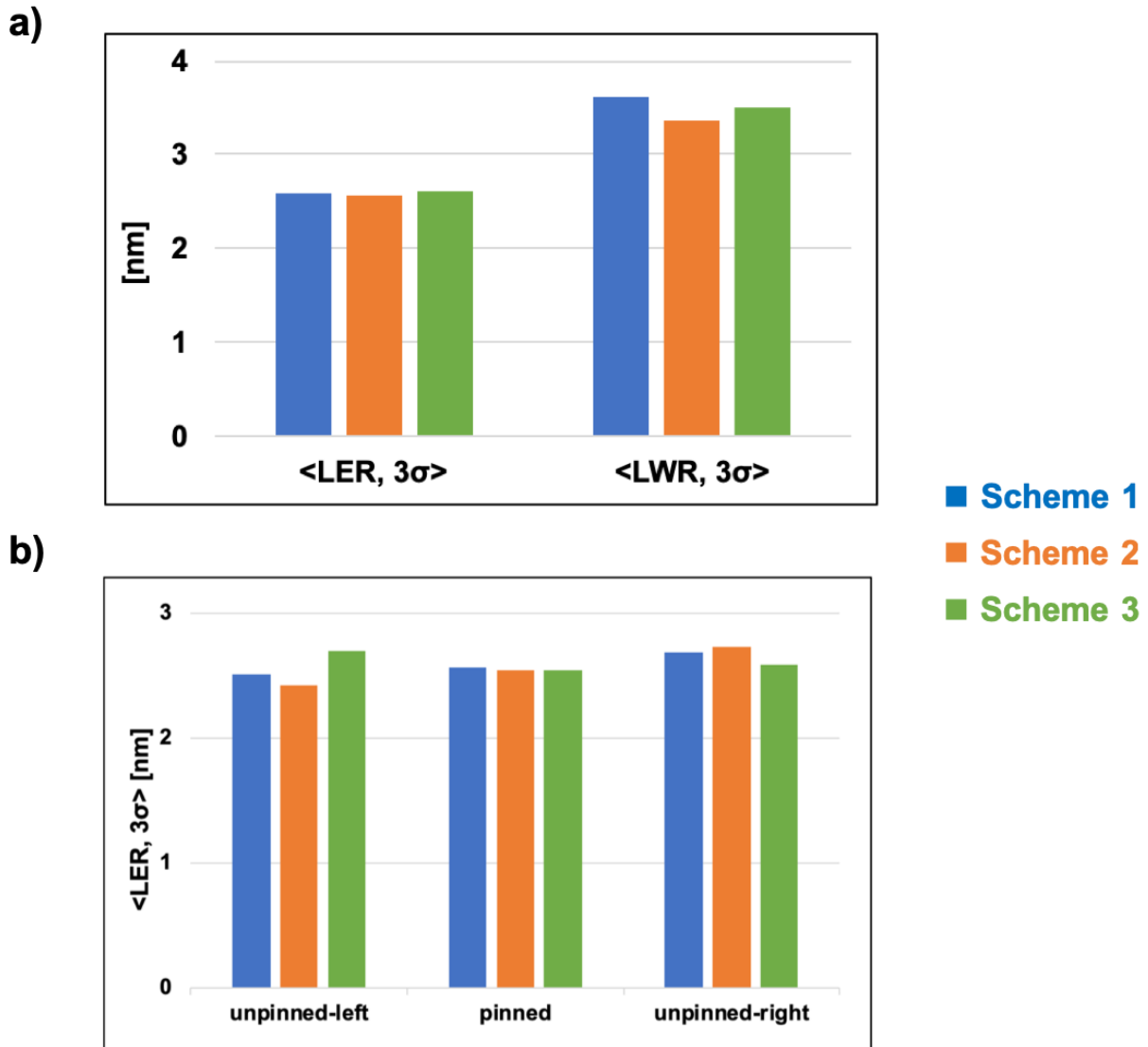


Figure 5.4 a) Height averaged roughness values (LER and LWR) for the two blends schemes-2 and schemes-3 as compared to the default scheme-1. b) LER averaged values for the left and right edge for the three resist domains. There is not significant difference in the roughness for the two blend schemes and the non-blend scheme.

5.2 BCP and homopolymer blends: effect on defectivity

Apart from roughness, the blends also need to be evaluated for its ability to form defect free structures. The LiNe flow trials described in chapter 3, are repeated for the three schemes. Five different unbiased initial states are studied. Systems with propensity to form defects are also sensitive to initial co-ordinates (after equilibration). Hence multiple trials with different initial conditions are desired for the same set of parameters. The BCP morphology is evaluated and the trajectory is saved every 200,000 steps. The first frame when the BCP forms defect free structure is recorded as the time required to completely annihilate all defects. Not all non-ideal lamellae can be considered as defects (figure 5.5)

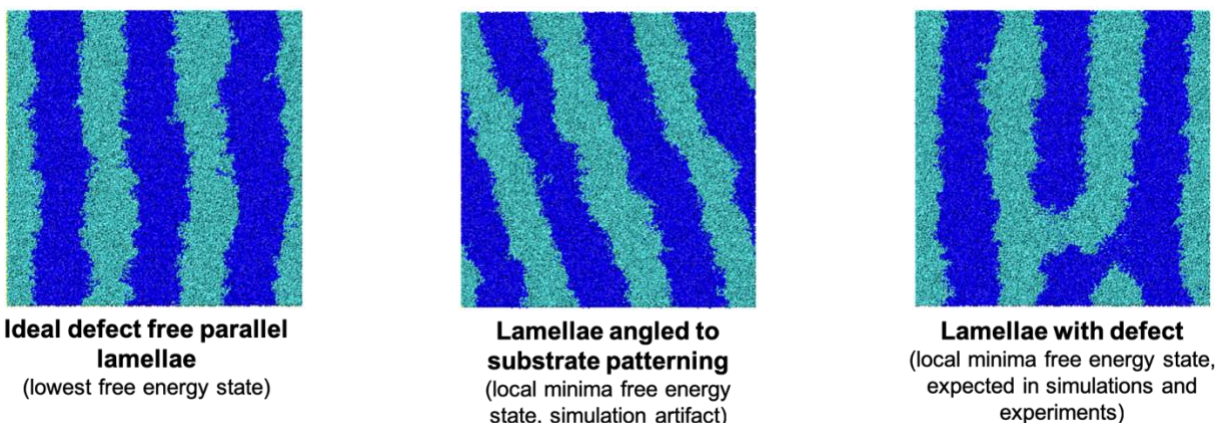


Figure 5.5: Morphologies seen for LiNe DSA flow. Lowest free energy state lamellae are desired. Angled lamellae are simulation artifacts and bridging are known defects.

An ideal defect lamellae will have the domains parallel to each other with no bridging between neighboring domains of the same monomer. This will be the global minima and the lowest free energy state, both in experiments and simulations. An anomaly in the form of angled lamellae (with respect to the substrate patterning) can also be formed. This would be a local minima free energy state, but such a morphology is not observed in experiments. This is a simulation artifact

probably formed by a limited box size. These results are not considered, and the trials are repeated with a different initial condition. Lastly, the system can also form defects like micro-bridge and dislocation defects. These are local minima free energy states which are seen both in simulations and experiments. The system is kinetically trapped and required further annealing to escape the potential well.

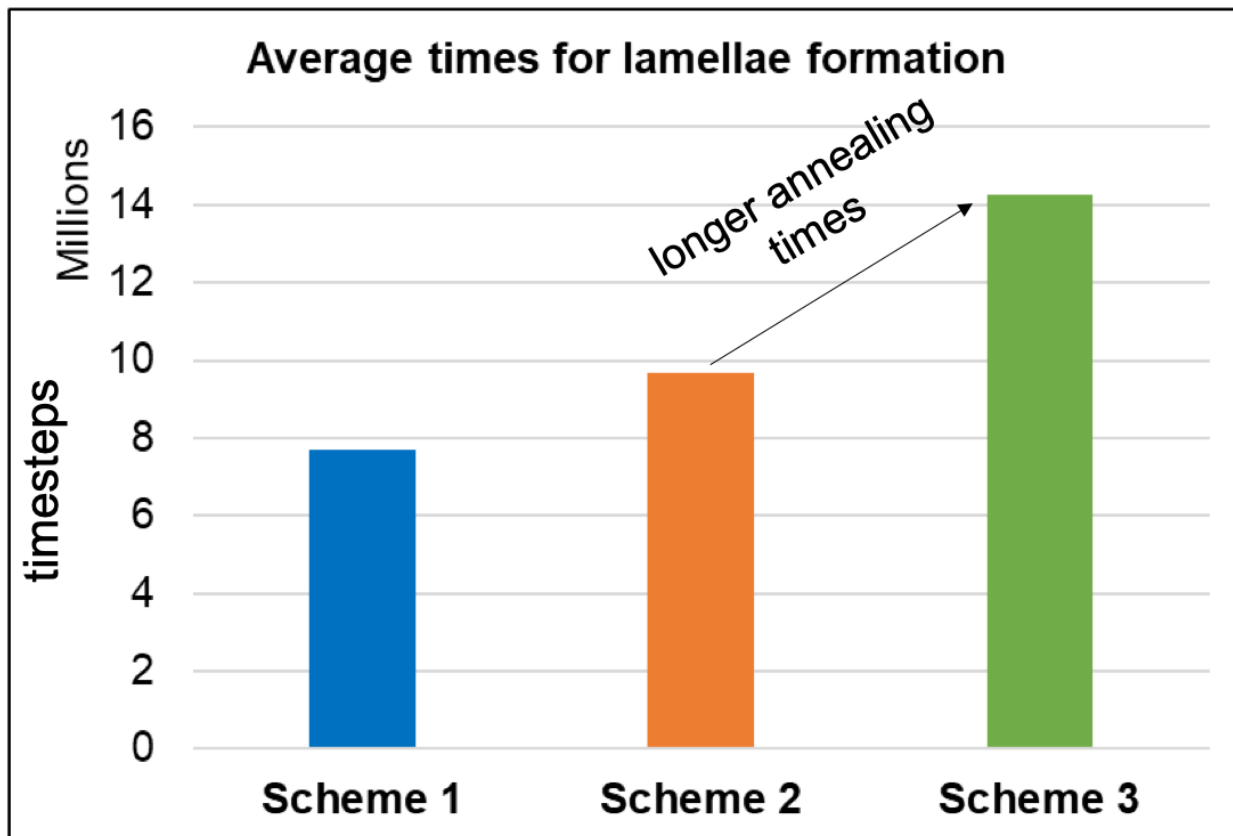


Figure 5.6: Ease of lamellae formation for the three schemes. Higher difference in the molecular weights of the two BCPs, more is tendency to form defects

As can be seen in figure 5.6, higher difference in chain lengths for the blends makes it more susceptible to defects. While scheme-2 required longer times for almost all trials attempted as compared to the defaults in scheme-1, its propensity to form defects is substantially lower than the scheme-3. The lower mobility by the longer chains nullifies the more mobile shorter chains for the

system to remain kinetically trapped for scheme-3 trials. It is important to note here that pinning width = 16nm $\sim 0.6L_0$. The L_0 corresponds to Scheme-1 BCP bulk pitch of 28nm. There may be some other pinning-width and pinning width interactions that reduces the inclination of scheme-3 to form defects.

Another popular strategy employed by polymer chemist to keep the BCP period constant irrespective of the batch-to-batch variation in synthesis is to mix small fractions of homopolymer (HP) blends to the system. These blends are mixed so as to keep the total PS to PMMA fraction constant. In our simulations, we also keep the total site density same for the homopolymer + BCP system as the monodispersed BCP system. A distinction from the non-homopolymer blend trials from the homopolymer blend is that the initial coordinates for the three systems being compared is the same for the latter. Hence, the effect of different initial state will not affect the simulations. In figure 5.7, the initial coordinates are the same unbiased state for all the three trials, with varied amount of homopolymers in the blend at constant total site density.

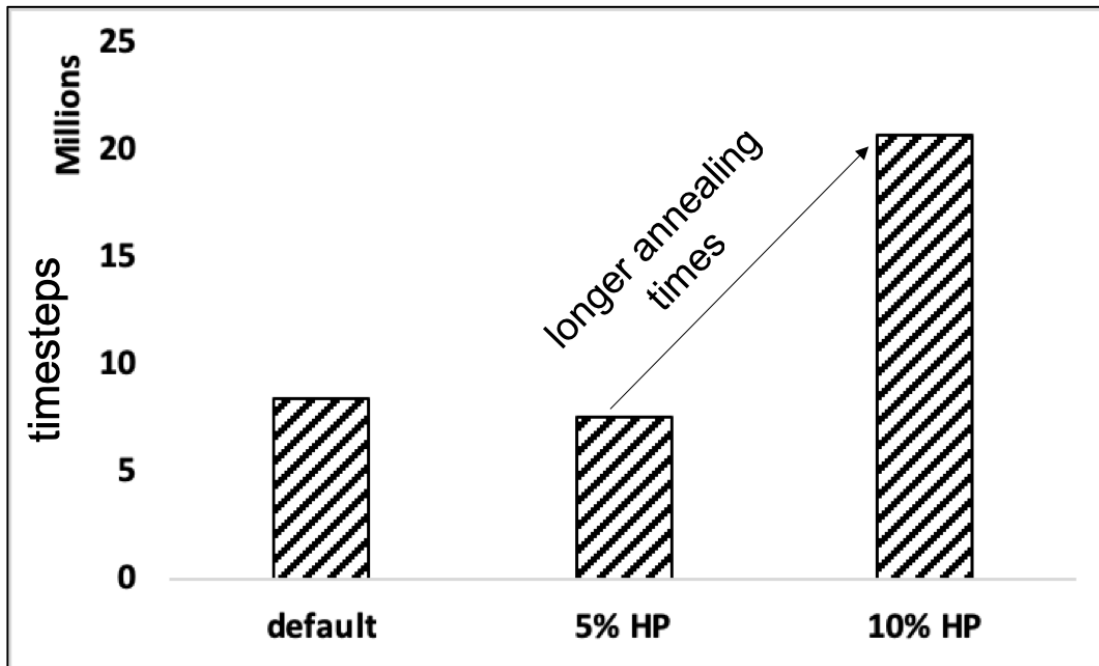


Figure 5.7: Effect of homopolymer addition on defectivity. 5% homopolymer addition helps in the ease of lamellae formation, adding 10% greatly increases the odds of forming a defect

Adding small quantities of homopolymer (~ 5 %) leads to lower annealing times whereas adding around 10% of homopolymers substantially affects the defect annihilation times. Homopolymer have a smaller chain length and offers more mobility than the BCP. As the homopolymer beads diffuse through the system, it helps the BCPs to escape from the kinetically trapped defect state. Increasing the amount of HP substantially, moves the system away from the default equilibrium that was achieved for the pinning width and pinning interactions for a default system.

Defects can be of different kinds. Simple micro-bridges as seen in figure 5.5 are easily annihilated by annealing the system further. If the width of this bridge is close to $\sim 0.5L_0$ then the defect would be bridge defect as opposed to a micro-bridge. These are comparatively more stable but seldom propagate entirely throughout the film thickness. On the other hand, defects like dislocations have deeper depth in their potential well and requires significant energy to be nullified. A question also

arises on the location of these dislocation defects: do they occur on the pinned domain or over the neutral substrates? Does the bottom substrate and the patterned substrate affect the defectivity across the film thickness? New simulations on a larger box were carried out to possibly answer these questions.

The default box size described in chapter 3 and chapter 4 have only one patterning per simulation box. This limits our ability to pinpoint the exact location of the dislocation. Hence new trials were performed on a larger box size, with twice the size in the direction perpendicular to the patterning.

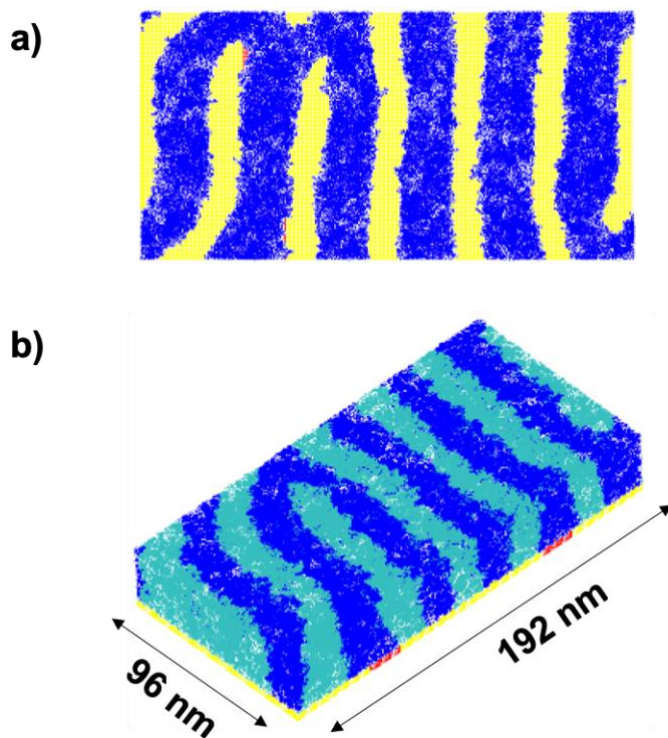


Figure 5.8: Larger simulation box with two PS patterning line in the x-direction. a) shows only PS domains with dislocations b) shows entire BCP defect morphology with the box dimension

There are now two patterned substrate lines on the substrate. Various initial conditions are tested so as to simulate dislocation defects. The system morphology for a dislocation defect is seen in

figure 5.8. Two defects are observed. One of the resists above the patterned line (pinned domain) is a defect less lamellae while the other is not. It cannot be said for certain that more dislocation defects will be seen over the pinning line strip as opposed to the neutral substrate. Even though the system is double the size as the default box, the defect density is still greatly exaggerated as compared to the experiments. These simulations are computationally expensive and do not scale linearly with the box size, thus limiting lower defect densities that could be studied.

5.3 ETCHING DEFECTIVE SYSTEMS

Post self-assembly, the morphology is analyzed by a scanning electron microscopy imaging of the system. SEM images only provides a 2-D top view image of the LiNe flow system. More sophisticated techniques like STEM can provide a 3-D tomogram but have yet to be integrated into industrial processes. 3-D tomograms are essential as the morphologies can have hidden defects that may not visible in top-views. These defects may be located at a lower film thickness close to the bottom substrate, but a 2-D SEM image can make the experimentalist conclude that the morphology is defect free. A defect free system is subsequently etched generally using a dry-etching scheme. As the etching process is not completely ideal, some of the PMMA phase is also consumed along with the resist PS phase. Thus, there lies a possibility for some of the defects, especially those at a higher film thickness that can be annihilated by appropriate etch chemistry and etching parameters. For this purpose, three systems were considered that were etched using the parameters described in chapter 4.

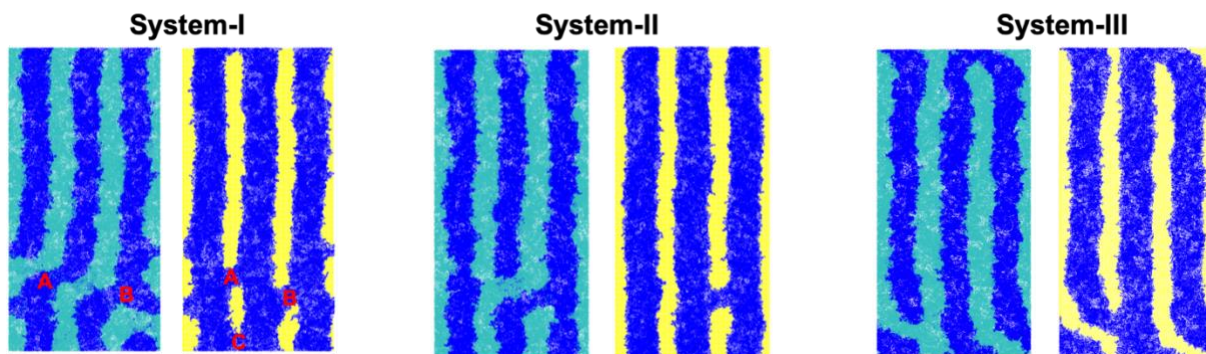


Figure 5.9: Defective BCP systems chosen for etching studies. System-I has three defects(A,B, and C) located at different locations across the film thickness. Defect C is hidden. System-II has a micro-bridge defect and system III has a dislocation propagated through the film thickness.

The morphology before etching as shown in figure 5.9 is not the lowest free energy state but were chosen as each of them represented interesting cases with distinct defects. System-I had three defects (**A**, **B**, and **C**). **A** and **B** are defects away from the bottom substrate, but **C** is close to the bottom substrate. System-II has only one micro-bridge defect and system-III has a dislocation that is propagated across the film thickness. For all the three systems, etching is performed at a constant pressure, $P = 10$ mTorr and $V_z = 0.01 \sigma/\tau$. The etch selectivity is a variable.

In figure 5.10, four selectivities, $S = 1.5, 2.5, 5.5, 10.5$ are studied and the morphology is observed at five snapshots. In these images t_{etch} , is the morphology frame at 100% PMMA removal. For $S=1.5, 2.5,$ and 5.5 after around half the t_{etch} , **A** and **B** defects that are away from the bottom substrate are annihilated as the PMMA selective etch beads consume the PMMA bridges and the PS selective etch beads consume the its PS counterpart. If the etching was stopped at $\frac{1}{2} t_{etch}$ and imaged using SEM, the system would appear to be defect free as the underlying defect **C** is not seen. Further etching would reveal the underlying defects as seen in the snapshots at $\frac{3}{4} t_{etch}$ and t_{etch} for $S = 1.5, 2.5,$ and 5.5 . For higher etch selectivity as in $S=10.5$, the number of PS selective etch beads are substantially lower than PMMA selective etch beads. Thus, $\frac{1}{2} t_{etch}$ is not sufficient time to annihilate defect **A** and defect **B** for the highest selectivity attempted. At complete t_{etch} , none of the selectivities can annihilate the microbridge of the resist from the pinned domain to unpinned-left domains. Lower selectivities, also leads to missing resist line at complete PMMA removal for $S = 1.5$ and 2.5

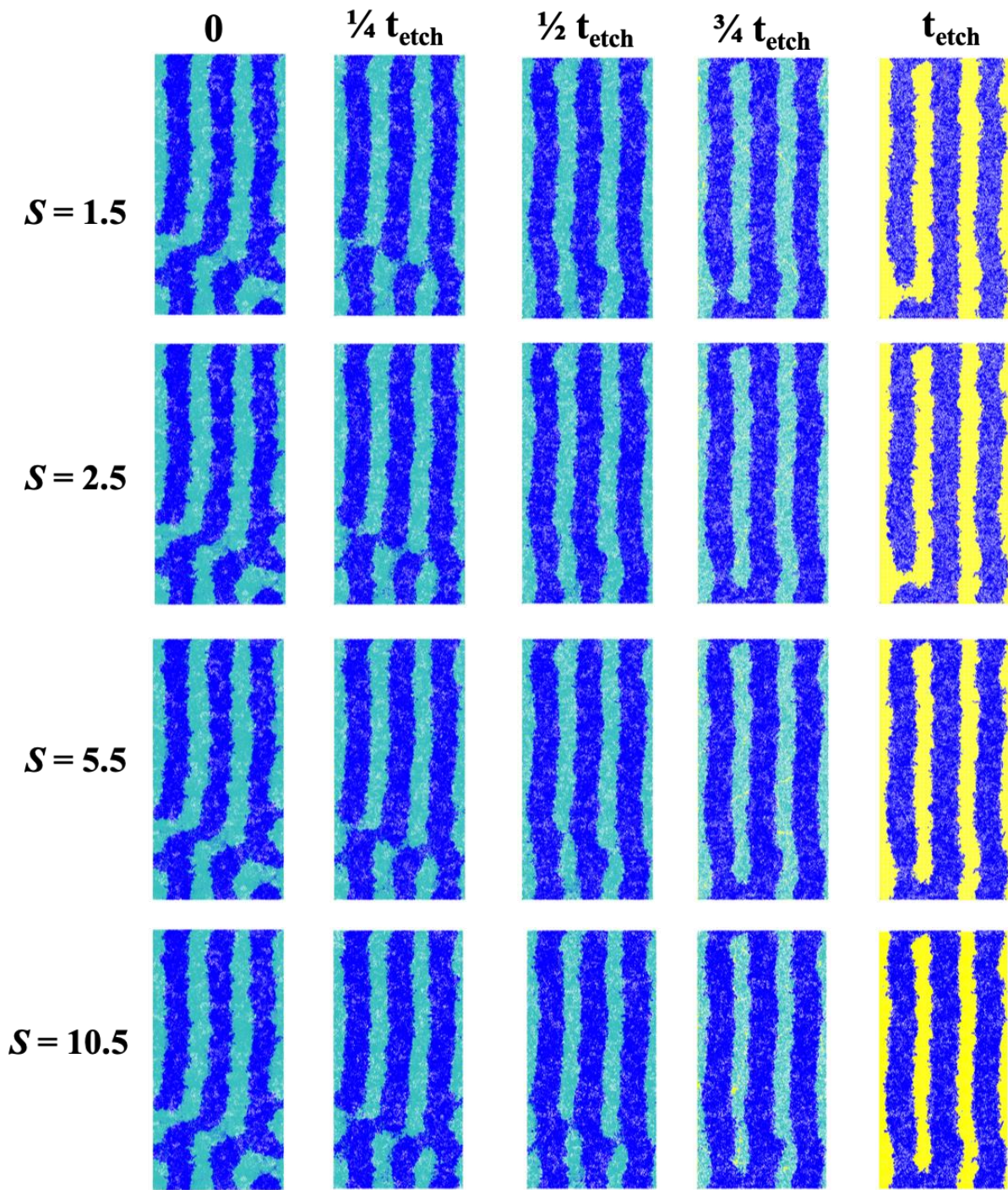


Figure 5.10: Etching on a defective morphology for system-I. Four selectivities are attempted. Those defects away from the bottom substrate are annihilated. Lower selectivities remove these defects quicker but lead to missing PS lines at complete PMMA removal.

For system-II, there exist only a microbridge between the middle resist domain and unpinned-right resist domain. This resist is close to the top-air interface and thus would be detectable in an experimental SEM image. It might appear that this system would be unviable for further processing and the manufacturer might discard it. As in system-I, etching is performed at $P = 10$ mTorr and $V_z = 0.01\sigma/\tau$ with a variable etch selectivity.

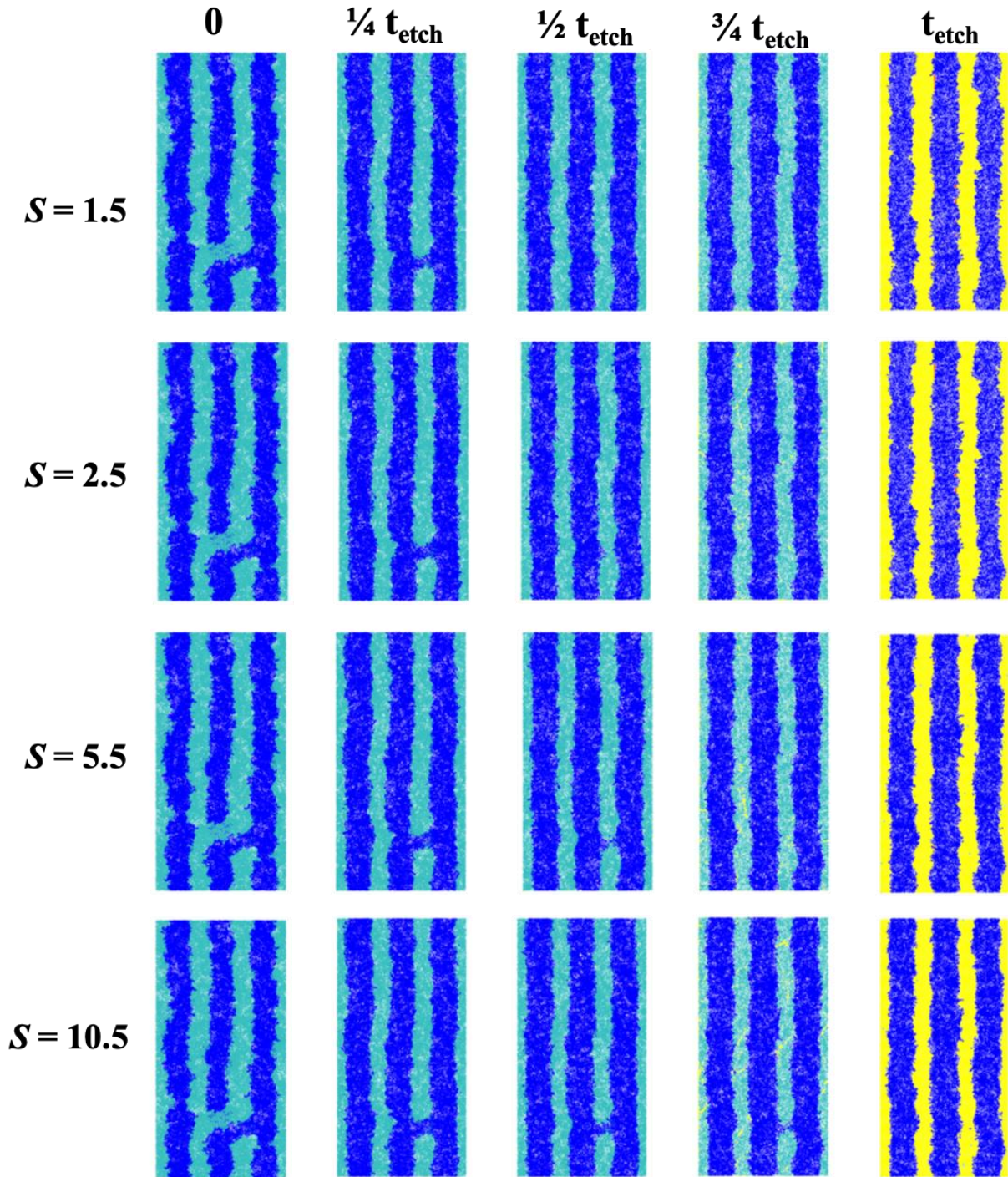


Figure 5.11: Etching on a defective morphology for system-II with only one micro-bridge defect. Four selectivities are attempted. Lower selectivity leads to faster defect annihilation via etching.

As seen in figure 5.11, etching the system causes the microbridge to be removed for most selectivities attempted. For $S = 1.5$ and 2.5 the micro-bridge is annihilated at $\frac{1}{2} t_{etch}$. For higher

selectivities, owing to lower number of PS selective etch beads higher etching time is required. For $S=5.5$, the defect is removed at snapshot $\frac{3}{4} t_{etch}$ and for $S=10.5$, the etch is removed close to t_{etch} . As long as the defect is annihilated before complete PMMA removal, the etching system will be effective in defect annihilation. Higher etch selectivity requires longer time for defect annihilation but the system at complete PMMA removal will have higher resist height leading to more resist for subsequent Silicon processing.

The last defect system etched is a dislocation defect in system-III. Two defects E and F seen. Note that F is propagated through the periodic y -direction and exist close to top-air interface. E defect is close to the bottom substrate. Figure 5.12 shows the snapshot for etch selective $S = 2.5$, $P=10$ mTorr and $V_z = 0.01\sigma/\tau$. E defect is annihilated around $\frac{3}{4} t_{etch}$. Whereas the F defect that is propagated through the film thickness cannot be annihilated for all the parameters attempted.

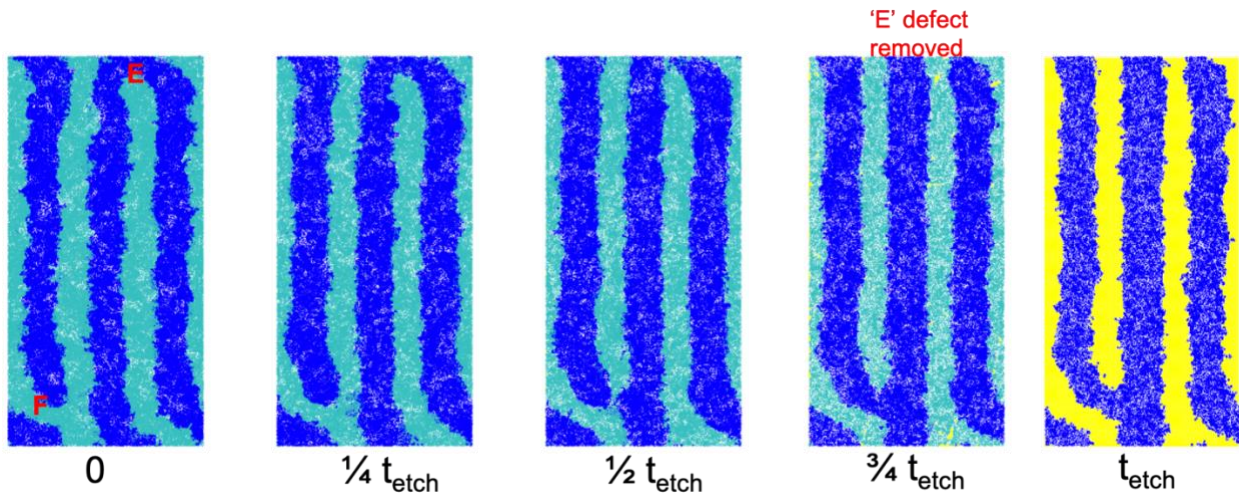


Figure 5.12: Effect of etching on defective system-III with a dislocation defect. $S = 2.5$, $P=10$ mTorr and $V_z = 0.01\sigma/\tau$. Dislocation defect that propagates through the film thickness is not annihilated.

This defect etching study thus sheds light on the possibility of annihilation of certain defects. While lower selectivities leads to lower resist height as seen in chapter 4, it does possess the ability to effectively annihilate certain defects.

5.4 ADDITIVES STUDY FOR ROUGHNESS REDUCTION

In the previous chapter and in section 5.1 of the current chapter, we have evaluated the roughness estimates from CGMD simulations. The average LER for the different lines for various simulations had values ~ 2.5 - 3.0 nm. This LER is the post-PMMA etch LER. The pattern transfer to the subsequent Silicon leads to reduction in LER comparable to the sub-2nm ITRS requirement. The high post-PMMA LER values could be attributed to either the inherent PS-*b*-PMMA interfacial width or to the possible imperfection caused by etching. The possible strategy to mitigate high roughness should be able to alter the probable causes. One such possible solution was to use to oligomeric additives that would self-assemble at the PS and PMMA interface. These polymeric chains, with substantially lower molecular weight than the BCP should be thermodynamically driven to the interface.

The goal of this study was to first elucidate the necessary conditions required to achieve the favorable self-assembly and subsequently analyze the effectiveness of the strategy to help mitigate the roughness. Some of the parameters varied include: oligomer chain length, additive concentration (expressed as percentage of the total polymeric content in the system), and the type of interaction of the oligomer with the BCP. The oligomer here is coarse-grained like PS (4 molecules = 1 CG bead ~ 400 g mol⁻¹). Table 5.1 summarizes the interaction of the oligomeric beads with other beads in the simulation.

Table 5.1: Interactions of the various types of additives with other bead types in the simulation.

Oligomer	PS	PMMA	Oligomer	Neutral brush	PS mat
PS attractive additive	Attractive LJ	Repulsive LJ	Attractive LJ	Attractive LJ	Attractive LJ
PS repulsive additive	Repulsive LJ	Attractive LJ	Attractive LJ	Attractive LJ	Repulsive LJ
Neutral additive	Attractive LJ	Attractive LJ	Attractive LJ	Attractive LJ	Attractive LJ

In the simulations attempted, PS repulsive oligomer was much more resistive to lamellae formation than PS attractive or neutral additive. The system would get stuck in a defective state that would be difficult to annihilate. Hence, for the detailed analysis PS attractive and neutral additives were preferred. Figure 5.13 shows a sample morphology formation for 3X multiplication, neutral additives (2.5%) of chain length $N13$. A large fraction of the oligomeric chains was self-assembled at the BCP interface. A similar observation was true for neutral oligomers of lower chain length and 2X multiplications, though the fraction assembled varied. Figure 5.14 gives a more detailed understanding of the effect of chain length and concentration.

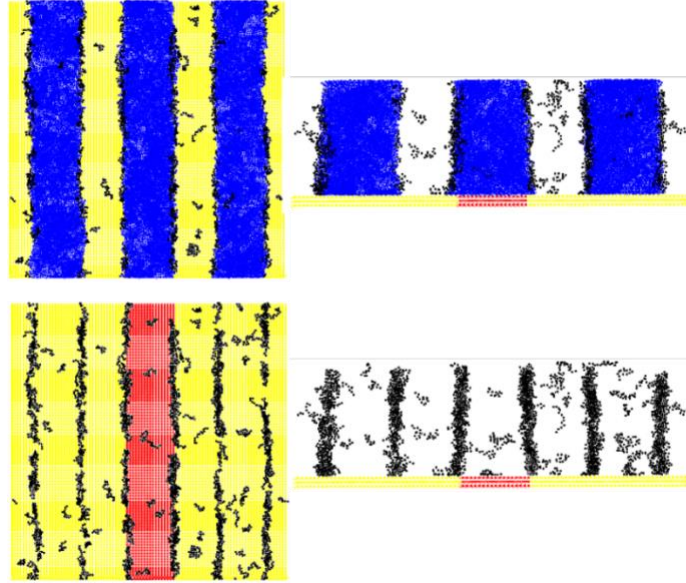


Figure 5.13: Morphology formed for neutral $N7$ additive for 3X multiplication. Black beads show additives

These trials were performed for neutral oligomers but on a substrate with 2X multiplication. In figure 5.14a, we see that for an additive concentration of 2.5%, we observe that the shorter chains ($N1$) spread across the domains more than the longer chains. Higher chain lengths ($N5$ and $N10$) have larger fraction of oligomeric beads at the BCP interface. The same trend held true for an additive concentration of 5%.

Next, the oligomeric chain length was kept fixed at $N5$ and the concentration was varied from 2.5-10% (figure 5.14b). We observe that lower concentrations have larger fractions at the interface. Higher the concentration, more will be the number of beads at the interface, but the fraction of the total oligomeric beads is lower indicating more spreading and swelling of the BCP domains. Similar trials were performed for PS attractive oligomers, but their efficacy was much lower than neutral oligomers. Additives that are repulsive to both PS and PMMA formed poor morphology due to high degree of agglomeration of the oligomers leading the trials inviable. We could summarize the following from the study:

- Neutral additives have the highest tendency to self-assemble at the interface. If the additive prefers PS, shorter chains will show a slight preference to the interface.
- For neutral additives, chain lengths of $N5-N10$ ($\sim 2,000-4000 \text{ gmol}^{-1}$) were the most suitable.
- For neutral additives, concentration of 2.5-5% of the total polymeric content (BCP + additive) is ideal.

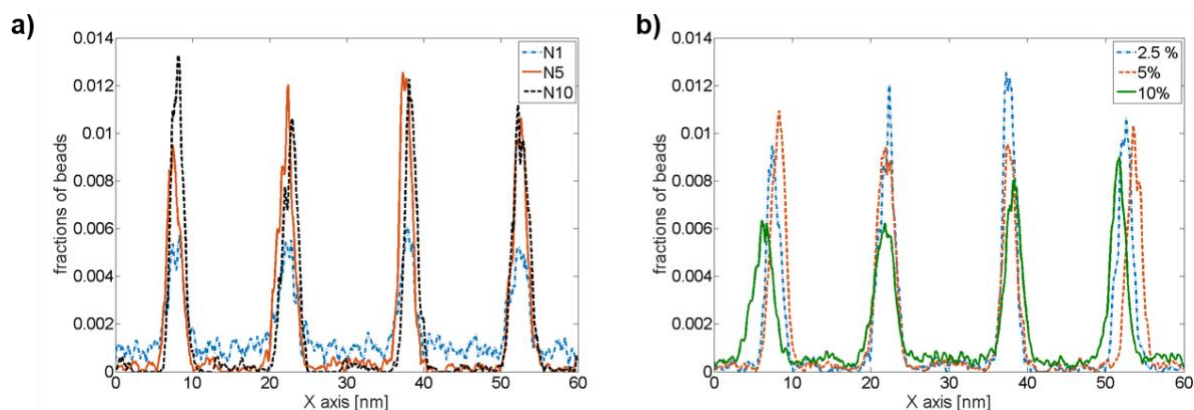


Figure 5.14: a) Effect of oligomeric chain length for 2.5 % neutral additive concentration and substrate 2X multiplication. b) Effect of oligomeric concentration for $N5$ neutral oligomers and 2X substrate.

Although the earlier trials tried to find the necessary conditions to drive the additives at the PS and PMMA interface, there still lies question on how effective the strategy would be to reduce the edge roughness. To answer these concerns, we compare the morphology of a pre-etch system with no additive with a neutral additive system. The substrate has 3X multiplication (with 6 BCP interfaces), no topography in both the cases and the additive trials have a concentration of 2.5%. Two oligomeric chain lengths of $N7$ and $N10$ were studied.

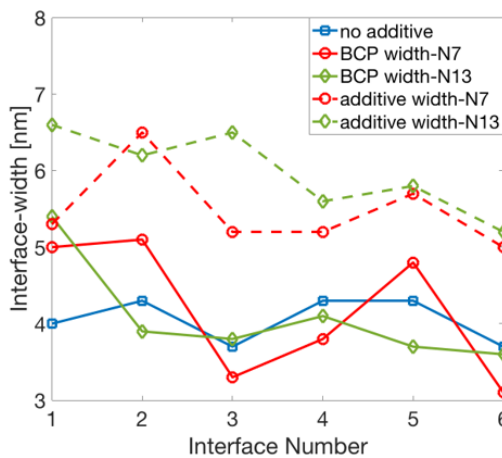


Figure 5.15: Effect of additives on the BCP interfacial width

Additive	Average BCP-interfacial width [nm]	Average additive spread width [nm]
No additive	4.05	-
<i>N7-neutral</i>	4.18	5.48
<i>N13-neutral</i>	4.08	5.98

Figure 5.15 shows a slight increase in the interfacial BCP-width due to the additives. This increase was higher on average for the lower chain of *N7* as compared to *N13*. Interestingly, the width of the additive phase (concentration spread) was substantially higher ($> 1\text{nm}$) for both the chain lengths as compared to their respective BCP interfacial widths. Optimally designed additives can thus possible protect the edges from the incoming dry etching ions and in-turn preserve the BCP interface.

One of the drawbacks of addition of these oligomers is that a substantial fraction self-assembles in the center of the domains and not just at the BCP interface. This leads to poor efficacy and material wastage. The additives can also lead to issues especially in an industry like the semiconductor industry wherein high purity products are desired. An alternative way to protect the edges was to

manipulate the BCP architecture by using BCPs with a small pendant group and a tri-block BCP with a smaller third block in between PS and PMMA (figure 5.16)

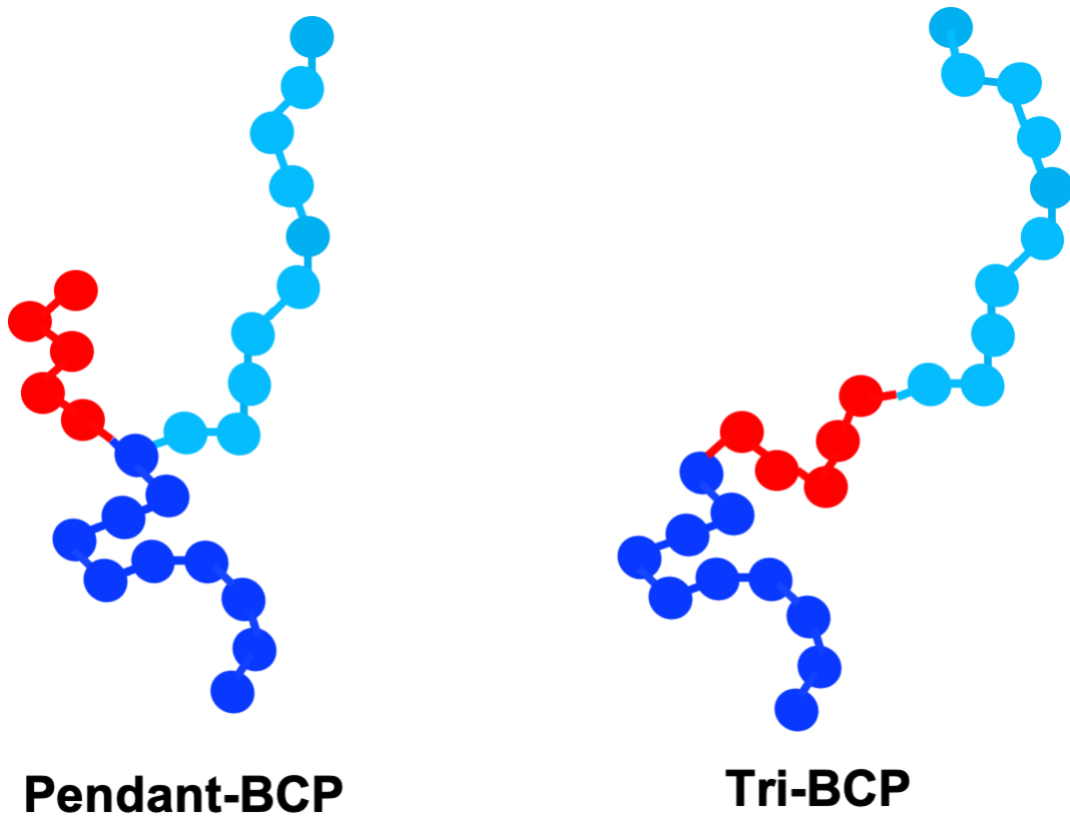


Figure 5.16: BCP structure manipulation with additives

As can be seen in figure 5.17, the third block beads self-assemble at the interface with no wastage in the PS or PMMA domains. Interestingly, the BCP interfacial width is always lower than the PS-PMMA concentration spread at the BCP interface suggesting possible protection from incoming dry-etch ions. As the chain length is only $N1$, the protection offered might not be sufficient for substantial protection. Higher chain lengths made it difficult to form lamellae as the system got stuck in a defective state.

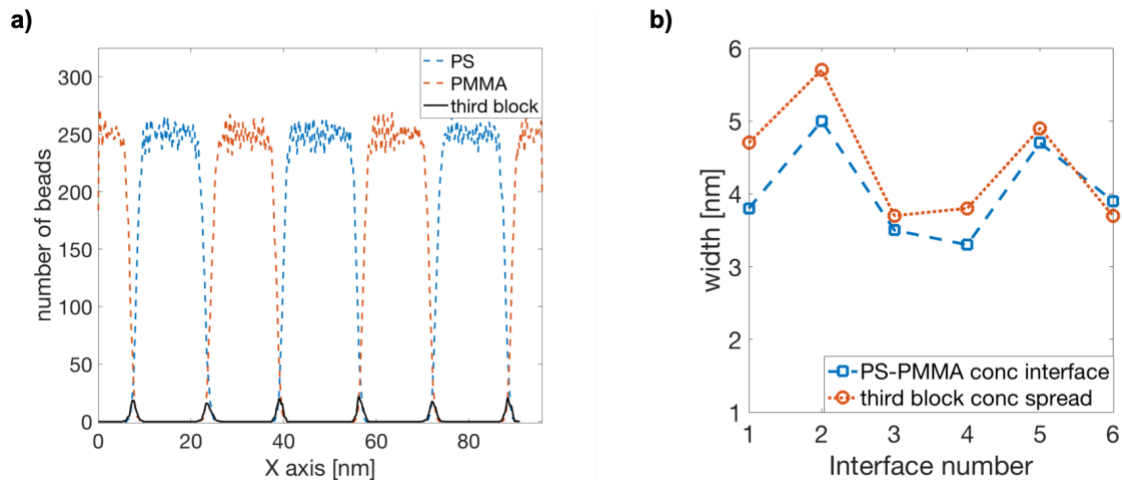


Figure 5.17: a) Concentration spread for tri-BCP. Additives self-assemble at the BCP interface with minimum wastage. b) Interfacial width for PS-PMMA and third block BCP spread.

Similar trials have been performed for BCPs with a pendant group at the PS and PMMA interface. In figure 5.18a, for a pendant chain length of $N2$, three types of pendant-BCP interactions have been attempted. The pendant can either be neutral, PS attractive or PS repulsive. The repulsive pendant on average has taller and narrower peaks. The pendant spread width is 6.2nm, 5.9nm, and 5.5nm for neutral, PS attractive, and PS repulsive pendants respectively. In figure 5.18b, the effect of pendant chain length is analyzed for pendants repulsive to PS and PMMA. Longer chains are taller and spread more and hence better protection from dry-etching is expected from $N5$. Trials with pendant chain length $N10$ were attempted but were highly resistive to lamellae formation.

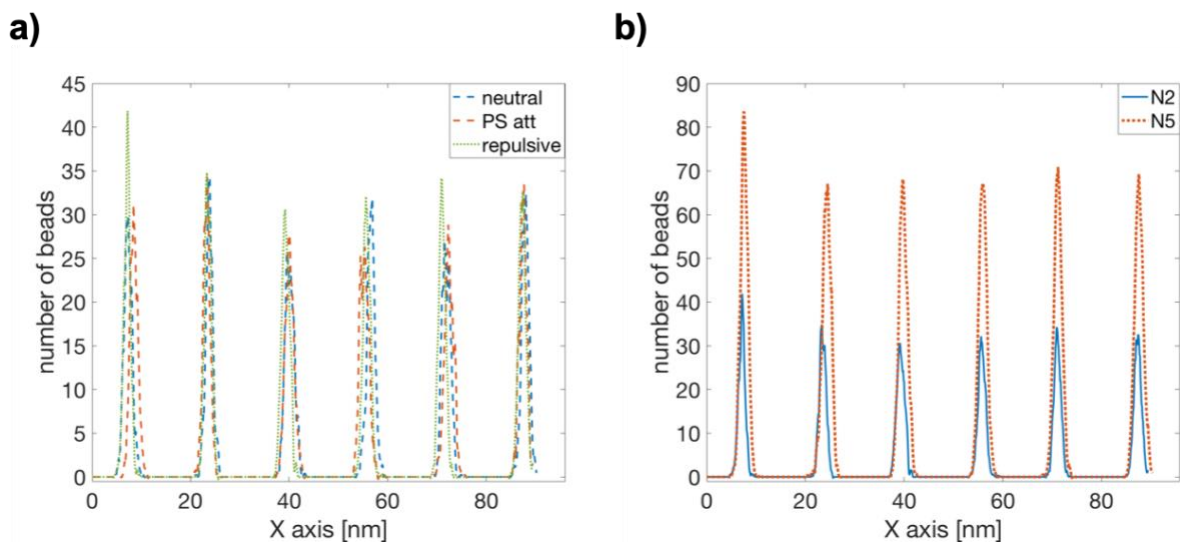


Figure 5.18: a) Concentration spread for the pendant group for three pendant types for $N2$. b) Effect of chain length for pendants repulsive to PS and PMMA.

These encouraging results can pave way for a more comprehensive, multi-faceted roughness mitigation strategy in the efforts to meet the desired ITRS targets.

CHAPTER 6

FUTURE WORK: NEXT-GENERATION LITHOGRAPHY TECHNOLOGIES

As the demands for Moore's Law continue to push for smaller, miniaturized devices, the current photolithography techniques aided with photomasks and optical masks corrections is eventually expected to reach its limitation². Critics of photolithography have been predicting its demise for many years now, but resourcefulness of the semiconductor industry in optimizing the current technology by developments like 3-D integration has flourished photolithography as the industry favorite technology³.

Alternatives like Directed Self-Assembly although is expected to be economically viable and can form technology nodes of similar order as photolithography, face bottlenecks due to high LER and defectivity. Efforts are in place in the industry and academia alike to tackle these holdup issues. Once these issues are solved, DSA can possibly be commercialized for the 14 nm node but forming lamellae domains sub-10 nm would be a major challenge. PS-*b*-PMMA with a BCP period of 28-30 nm is expected to have a BCP interfacial width of greater than 4 nm. This interfacial width does not scale linearly with the molecular weight of the BCP⁴. Thus, to form smaller nodes, when BCP with lower molecular weight are used, the problems of LER is expected to get worse. Moreover, the BCP interaction strength, χN will be lower, leading to a lesser driving force for the BCP phase-separation. Using high- χ BCPs like Poly(styrene-*b*-(lactic acid-*alt*-glycolic acid))⁵ is a prospect that has been explored. These BCPs can theoretically form smaller domains, but the issues with defectivity is worse than BCP with moderate to low χ values. PS-*b*-PMMA, has similar affinity to the air layer (or to a neutral gas like N₂ or Ar). With most high- χ BCPs, the two monomers have

contrasting interaction with air layer leading to a preferential phase separation that is non-uniform close to the BCP-air interface. Hence, a protecting layer in the form of a top-coat is required for many of the DSA with high- χ BCPs.

The current consensus among semi-conductor industry professionals seem to be that unless the issues of high defectivity and LER are solved soon, it will be highly unlikely that DSA will be commercialized anytime soon. When these issues are overcome, DSA might not be the technology for the manufacture of latest processors in the coming years but can still be an excellent economical choice for the future 'entry level' processors that some may characterize as high-end today. Apart from logic nodes, DSA's potential in storage devices still looks bright. To digitalize the entire globe on a budget, it is crucial that the industry does not part with this technology and invest its time and resources in the research and development of DSA.

6.1 NANOPATTERNS USING OLIGOMERIC SELF-ASSEMBLED MONOLAYERS

6.1.1 INTRODUCTION

Self-assembled monolayers (SAMs) are organic films that are formed by oligomeric materials by covalently bonding to solid surfaces. They have been used to impart functionality to surfaces modifying their surface properties like adhesion, friction, hydrophilicity, and protection against lithography.⁷⁻⁹ These molecules are extremely thin (~1-3 nm) and can be controlled to uniformly coat surfaces.⁸ Among the popular SAMs, alkanethiols have been used popularly to modify surfaces because of the high stability offered by their SAM structures.¹⁰⁻¹² These SAMs can be used in variety of industrial nanotechnological applications, in particular for microelectronics and semiconductor industry¹³⁻¹⁴. Alkanethiols are generally self-assembled on metals like Gold using bifunctional oligomers¹³.

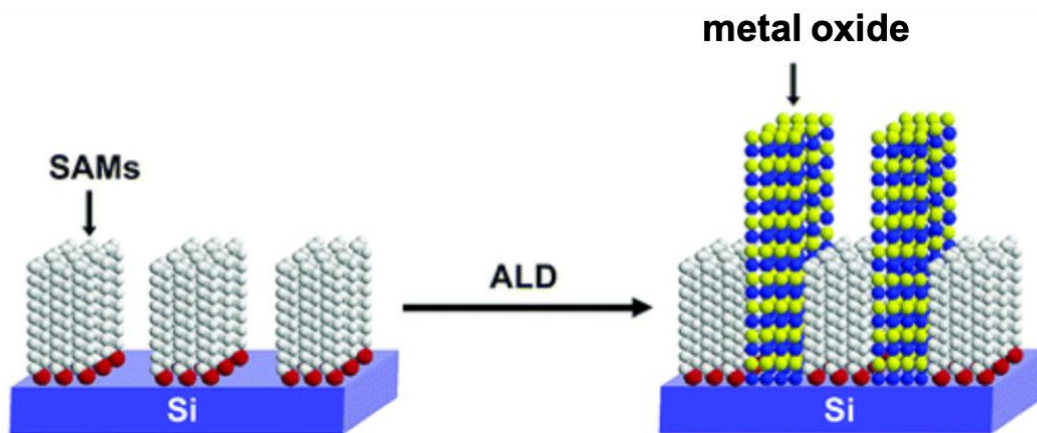


Figure 6.1: Schematic of using SAMs with atomic layer deposition adapted from Park *et. al*⁷

Alternatively, there are organic molecules like octadecylsiloxane⁷ that are attached to Si or SiO₂ substrates via self-assembly. As Si still remains the favorite for the industry due to the vast expertise, infrastructure and knowledge developed over the years, the oligomers that form SAMs on Si based surfaces are of more interest for lithographic studies. These SAMs aided with other lithographic techniques can be used to form nanolithographic patterns (<10 nm) in order to compete with lithographic technologies of the future like EUV with higher NA. The SAMs can be economically deposited on a patterned monolayer by site selective deposition like microcontact printing lithography¹⁵, nanografting¹⁶, dip-pen nanolithography¹⁷⁻¹⁸ etc. Post self-assembly and removal of access material, a topographic surface is formed which can act as a base for atomic layer deposition to form a metal-dielectric pattern (figure 6.1).

6.1.2 MODEL AND METHODOLOGY

A surfactant-based model is employed for the SAM simulations¹⁹. This model was first introduced by Telo de Gamma and Gubbins²⁰ followed by Grest *et al*²¹ and Smit *et. al*²². The model has been popularly used for amphiphilic short to moderately chained organic molecules with one end being hydrophilic and other being hydrophobic. These oligomeric chains can be single-chained, dimeric or trimeric, architectures popular among gemini surfactants²³ with spacer molecules.

For the current work, the oligomeric chains are described with beads and springs. The chains have a terminal head and a longer tail, the head being hydrophilic and the tail hydrophobic. This definition can be interchanged as per the requirement. The beads are joined together by a harmonic spring and non-bonded interact with appropriate versions of long-range Lenard Jones potentials. As in Maiti *et. al*.¹⁹, the model currently does not assume any bond bending or dihedral potential as the Kuhn-length for these short-chained polymers are sufficiently small.

The size of the coarse-grained bead in the model is $\sigma = 0.34$ nm and a bead mass of $m = 36$ g/mol. The default Lenard-Jones potential strength for all pair-wise interactions is $\epsilon = 2.5$ kJ/mol. All the simulations are carried out a reduced temperature $\tau = 1.0 \sim 300$ K for about 7 ns. The like beads interact with a tail-corrected Lenard Jones potential as described below:

$$U_{att}(r) = \begin{cases} 4\epsilon \left[\left(\frac{\sigma}{r}\right)^{12} - \left(\frac{\sigma}{r}\right)^6 \right] + S_{LJ}(r) & r < r_c \\ 0, & r > r_c \end{cases} \quad \text{equation 6.1}$$

$$S_{LJ}(r) = \begin{cases} C, & r < r_1 \\ \frac{a}{3}(r - r_1)^3 + \frac{b}{4}(r - r_1)^4 + C, & r_1 < r < r_c \end{cases} \quad \text{equation 6.2}$$

The unlike beads interact with the Weeks-Chandler Anderson potential,

$$U_{rep}(r) = \begin{cases} 4\epsilon \left[\left(\frac{\sigma}{r}\right)^{12} - \left(\frac{\sigma}{r}\right)^6 \right], & r \leq 2^{\frac{1}{6}} \sigma \\ 0, & r > 2^{\frac{1}{6}} \sigma \end{cases} \quad \text{equation 6.3}$$

The short-ranged interactions are defined by a harmonic potential:

$$U(r) = \frac{1}{2}k(r - r_0)^2 \quad \text{equation 6.4}$$

$$k = \text{harmonic spring constant} = 30 \epsilon \sigma^{-2}$$

$$r_0 = \text{equilibrium bond length} = 1.2 \sigma$$

The site density for the oligomer is kept constant at 0.85 beads / σ^3

6.1.3 RESULTS

Prior to the simulations on a representative substrate, bulk simulations were performed to study the self-assembly under the conditions above. The chain lengths studied were: $N3$ (118 gmol^{-1}), $N5$ (180 gmol^{-1}), $N8$ (288 gmol^{-1}), and $N10$ (360 gmol^{-1}) and the length of the simulation box was 30σ in each dimension. The morphologies at equilibrium are shown in figure 6.1.

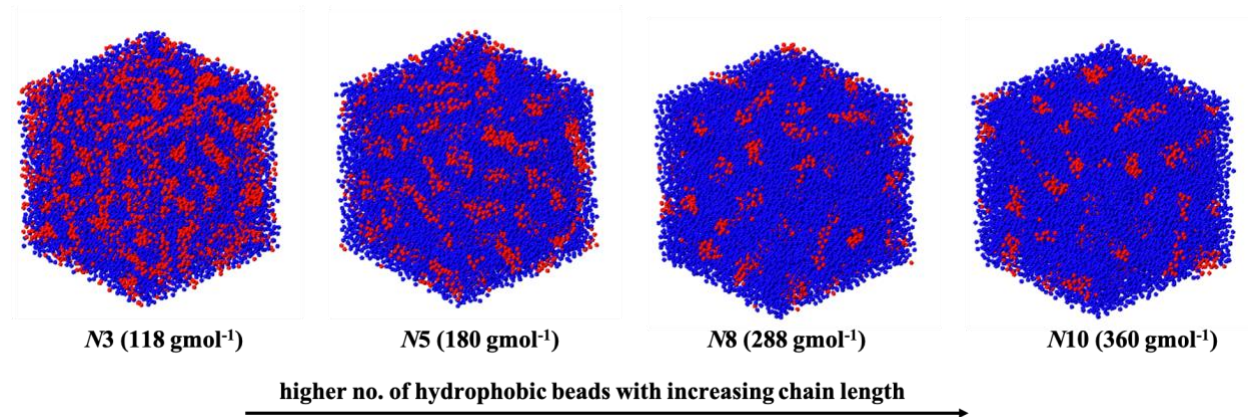


Figure 6.2: Bulk self assembly of the oligomer. Higher chain length has lower percentage of head groups.

For all these chain lengths, only one terminal bead per chain is hydrophilic and the rest of the chain is hydrophobic. For lower chain lengths, as the total percentage of hydrophilic chains in the system is high, agglomeration of these chains is observed leading to formation of larger domains as compared to the higher chain lengths. For the subsequent trials, $N5$ and $N10$ were chosen as the default chain lengths for the systems.

6.1.3.1 *Self-assembled monolayer on a substrate*

For the trials with substrate, the oligomeric interactions and density is kept same as the previous section. The oligomer self-assembles on a substrate that has three layers of beads that are hexagonally packed. The bead size of the substrate is same as that of the oligomer, $\sigma=0.34$ nm. The substrate thickness is $2.5 \sigma \sim 0.85$ nm. Trials were first performed on a substrate that is completely biased (figure 6.2a), i.e. all the beads on the substrate are selective. In this case, the substrate beads have a preference to the hydrophilic head of the oligomer and are defined by an attractive potential while the hydrophobic tail is defined by a repulsive LJ potential. Chemically, the hydrophilic bead has a functional group like hydroxyl or thionyl group that has a propensity to form a permanent bond with the functionalized substrate. The model implemented assumes that the head bead bonds permanently with the substrate with 50% probability if the two beads are within $(\sigma+0.1)$. This probability is a variable and lower values lead to slower kinetics.

The second type of substrate is patterned with only a part of it having a preference to the oligomeric head (figure 6.2b). The beads shown in purple in figure 6.2b are attractive to the hydrophilic head and repulsive to the hydrophobic tail.

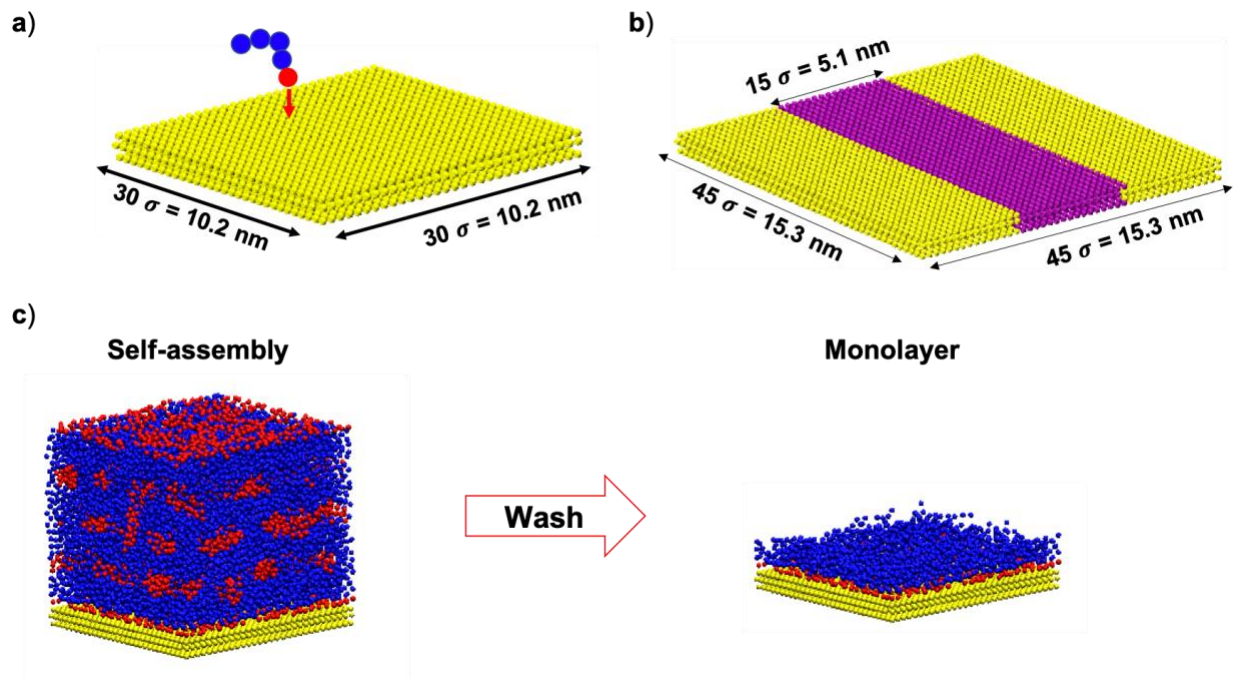


Figure 6.3 a) Biased bottom substrate with beads attractive to the oligomer head beads. Head beads within the etch radii has a 50% probability to be permanently bonded with the substrate. b) Patterned substrate with the patterned line (purple) being attractive to the head beads and can form a permanent bond with 50% probability. Patterned beads are repulsive to the oligomer tail. The non-patterned substrate(yellow) can either be biased opposite to the patterned or neutral. c) Morphology of the beads after the self-assembly phase and subsequent washing on a biased unpatterned substrate

After the self-assembly, the simulation is stopped when the number of chains being tethered to the substrate reaches saturation. Tests are different parameters revealed that this equilibrium is reached around ~ 7 ns. The next phase involves removal of those oligomeric chains that are not tethered to the substrate. Experimentally this is achieved by washing the substrate with a benign solvent. In our simulations, this is achieved by simple deletion of the untethered chains (figure 6.2c)

For both these substrate, different film thicknesses were studied keeping other parameters constant. The morphology for $N_5=180$ g/mol *post-self-assembly* and *post-washing* are shown in figure 6.3 for four film thicknesses = 5σ , 10σ , 20σ , and 25σ . The results seen have some similarities with flat substrate trials in chapter 2. Increasing the film thickness, results in a greater number of head-

domains sandwiched. While 5σ has two surface domains and no middle domains, increasing the film thickness to 10σ , 20σ , and 25σ leads to formation of additional 1, 2 and 3 middle domains. These trials were also repeated for oligomeric chain length of $N10 \sim 360$ g/mol. For the higher chain length, lower film thicknesses cause higher confinement effects leading to discrepancies in the simulations. Hence only film thicknesses of 15σ , 20σ , and 25σ were considered for $N10$ trials and the subsequent patterned substrate trials. The chain tethering and surface coverage statistics are recorded in figure 6.3b-c for these simulations. Higher molecular weight oligomers cause steric hindrance towards bead tethering. The approach of head beads to the substrate is hindered by the longer tail of $N10$. Hence the number of beads tethered is lower for $N10$ as compared to $N5$. Interestingly, higher molecular weight oligomer will have higher coverage owing to a greater number of beads per oligomeric chain, even for lower tethering.

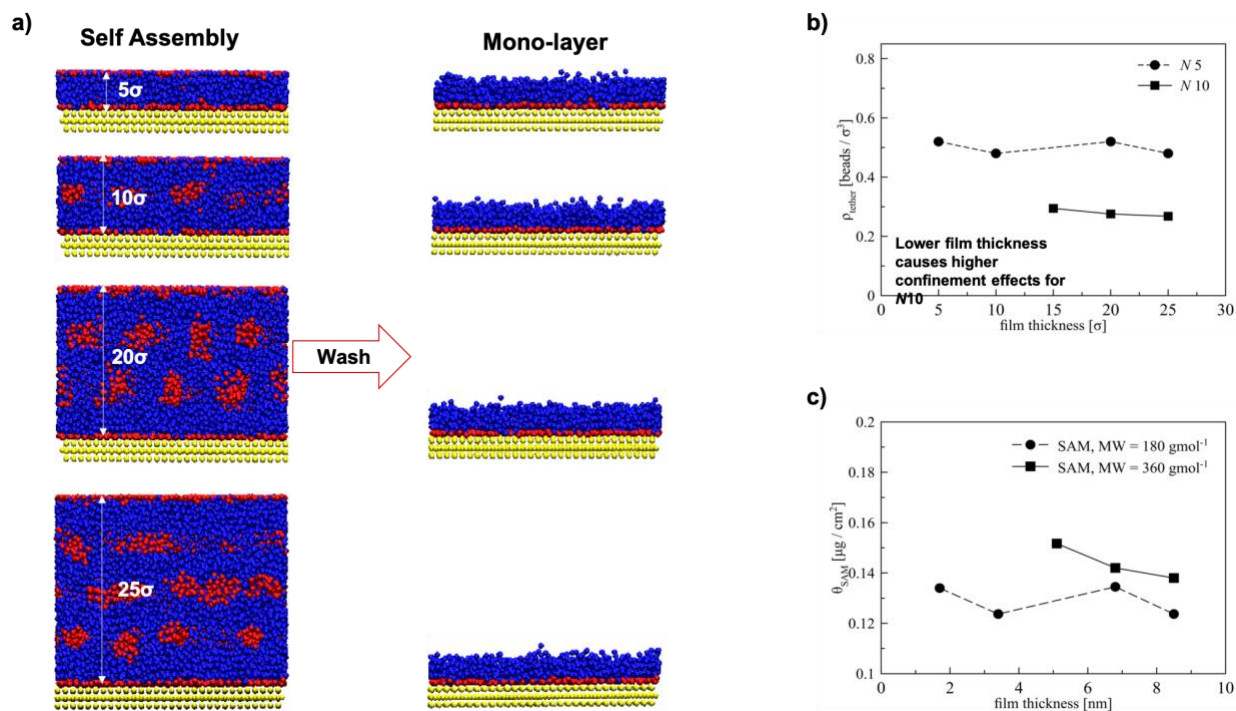


Figure 6.4: a) Morphology after self-assembly and monolayer formation post washing for $N5 = 180 \text{ g/mol}$ for film thickness = 5σ , 10σ , 20σ , and 25σ . b) bead tethering density for $N5 = 180 \text{ g/mol}$ and $N10 = 360 \text{ g/mol}$ as a function of the film thickness. Lower chain lengths have higher tethering density. c) Surface coverage vs film thickness for two molecular weights. Higher molecular weights will have higher coverage even though it has lower bead tethering density.

6.1.3.2 Self-assembled monolayer on a patterned substrate

Next, trials were performed on a patterned substrate for $N10$ and $N20$ for film thicknesses 15σ , 20σ , and 25σ . The patterned beads are attractive to the oligomeric head beads and repulsive to the oligomeric tail beads. The part of the substrate shown in yellow in figure 6.2b can either be neutral and unbiased towards oligomers (patterned type-I) or be attractive towards oligomeric tail and repulsive to the oligomeric head (patterned type-II). The morphology for the three film thicknesses is shown for in figure 6.4a for $N5$ and figure 6.4b in $N10$ for patterned type-I substrate. The patterned part for these substrates has a higher concentration for oligomeric heads while the

unpatterned part does not have a strong preference for either of the beads. As seen in the unpatterned substrate trials, the self-assembly morphology has higher middle head domains for higher film thicknesses. For the patterned part of the substrate, the presence of oligomeric head beads leads to a disruption in the middle domains above as compared to the middle domains above the non-patterned part.

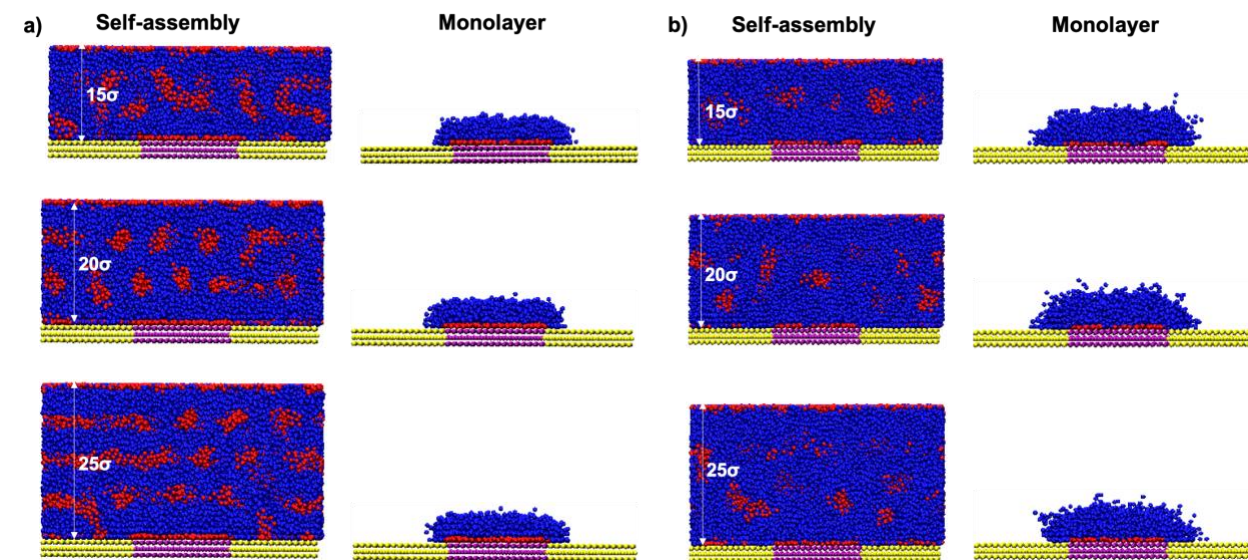


Figure 6.5: Patterned substrate (type-I) self-assembly and monolayer formation for a) $N5 = 180$ g/mol and $N10 = 360$ g/mol. Higher molecular weights form taller mushroomed monolayer.

Interestingly, a mushrooming effect is seen once the untethered beads are washed away. The oligomeric tail spreads outside the patterned substrate into the unpatterned one. This spread and the height of the mushroomed self-assembly is higher for $N10$ as compared to $N5$ which is expected from the long oligomeric chain. The *post*-self-assembly washing leads to a similar monolayer morphology after deletion of the untethered beads.

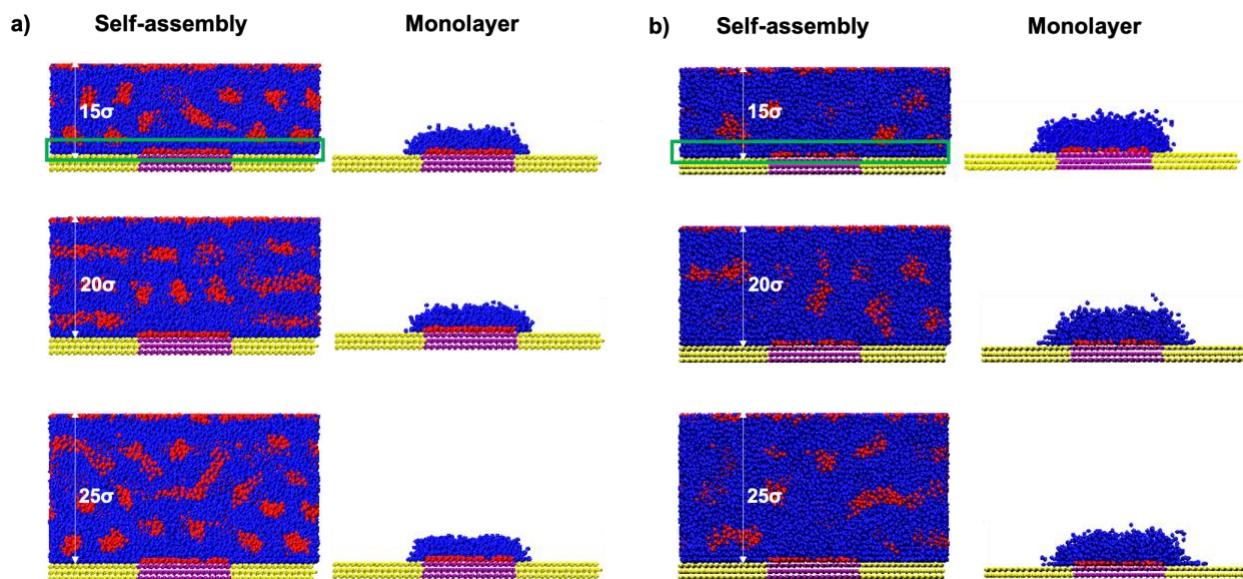
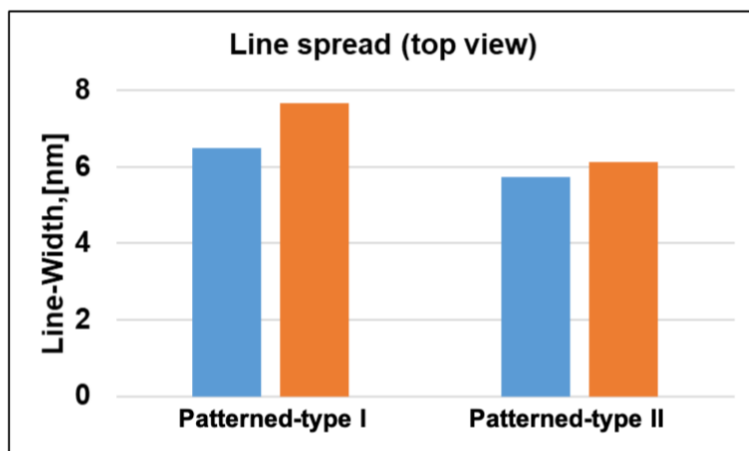


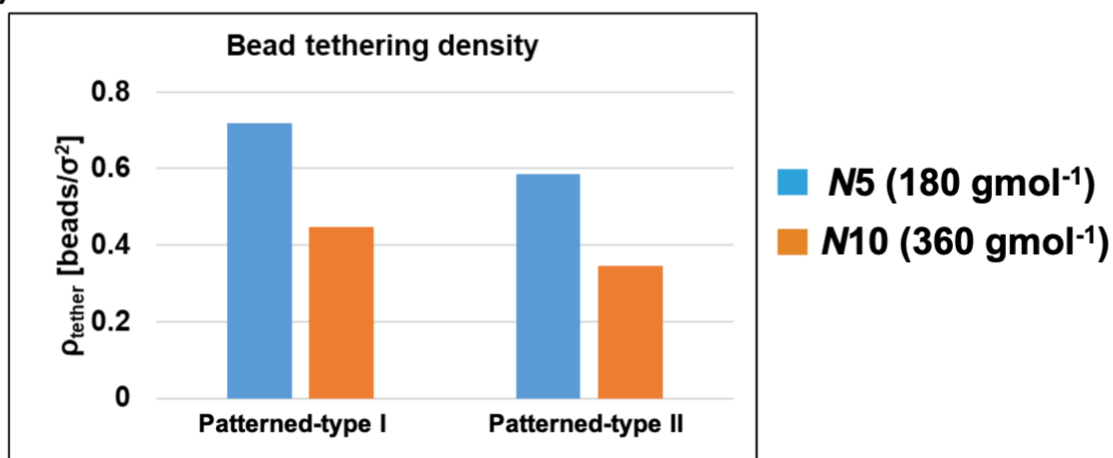
Figure 6.6: Patterned substrate (type-II) self-assembly and monolayer formation for a) $N5 = 180$ g/mol and $N10 = 360$ g/mol. Higher molecular weights form taller mushroomed monolayer as in patterned substrate type-1.

For the patterned type-II, a strong preferential bias is observed for the non-patterned part of the self-assembly morphology by the oligomeric tail (highlighted in green in figure 6.5 a-b). The chain tethering statistics for the mushroomed monolayer for film thickness of $20\sigma = 6.8$ nm is shown in figure 6.6. As seen in figure 6.6a, the average line-widths for the same chain length is higher for the patterned type-I exhibiting higher spreading compared to type-II. The tail beads for the tethered oligomers have enthalpic affinity to the unpatterned part of the substrate for patterned-type II which leads to the higher spreading for these trials. For the same type of substrate, lower molecular weight has a lower line-width and lower spreading. Lower MW oligomers also has higher tethering density but lower total SAM coverage for the same substrate type as seen in figure 6.6 b-c. Type-I substrate also leads to higher tethering density on the patterned substrate for the same molecular weight leading to a higher SAM coverage.

a)



b)



c)

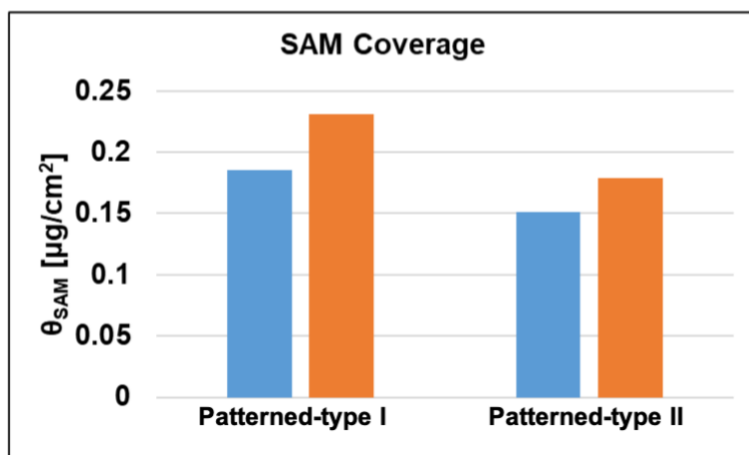


Figure 6.7: Chain tethering statistics for substrate type-I and type-II for chain length $N_5 = 180$ g/mol and $N_{10} = 360$ g/mol. a) Line-Width statistics. b) Bead tethering density. c) Self-Assembled Monolayer surface coverage.

6.1.4 SUMMARY

A Coarse-grained molecular dynamics model has been developed for studying its self-assembly on a patterned substrate and completely unbiased substrate. This preliminary model along with the early results serve as a proof of concept and can be altered depending on the specific system to be studied. The molecular weights of the oligomer and the functionality of the patterned and unpatterned substrate strongly determine the morphology of the patterned SAM line formed. By changing the coarse-graining, interaction strength and associated bead mass, the SAM oligomer and its interaction with the substrate can be made more specific for a closer comparison with experiments.

6.2 STOCHASTICS COARSE GRAINED MOLECULAR DYNAMICS SIMULATIONS FOR EXTREME-ULTRAVIOLET RESISTS

6.2.1 INTRODUCTION

The immediate and as some industry experts point out as the more viable alternative to DSA is Extreme Ultra-Violet Lithography (EUVL)²⁴. Intel, the world-leader in semiconductor technologies along with their collaborators are expected to start high-volume manufacturing of transistors using EUVL by 2020²⁵. The investments in DSA by the semiconductor industry has been fractional of that of EUVL, but issues persist that require quick solutions prior to the 2020 manufacturing deadline²⁶. Experimental solutions to many of the EUV bottlenecks have been developed over the last few years, but the fundamental understanding of many of the processes remains poor. Continuum based models²⁷⁻²⁸ have been developed, but many of these models have stochastics-based limitations and hence are not ideal to study stochastic effects like photon noise and acid diffusion leading to non-idealities like LERs. It is therefore crucial to model the EUV process using a non-continuum stochastic approach like coarse-grained molecular dynamics along with Monte-Carlo simulations²⁹⁻³⁰.

In this section of the chapter, coarse-grained molecular dynamics model for EUV resist self-assembly and subsequent process modeling are introduced. The processes for the technologies are explained along with the methodology for the simulation. Proof of working and some preliminary results are then presented for various process phases.

6.2.2 EUV PROCESS

Four stages can be defined and simulated to characterize the EUV process to obtain a nano-patterned resist (figure 6.7)³¹.

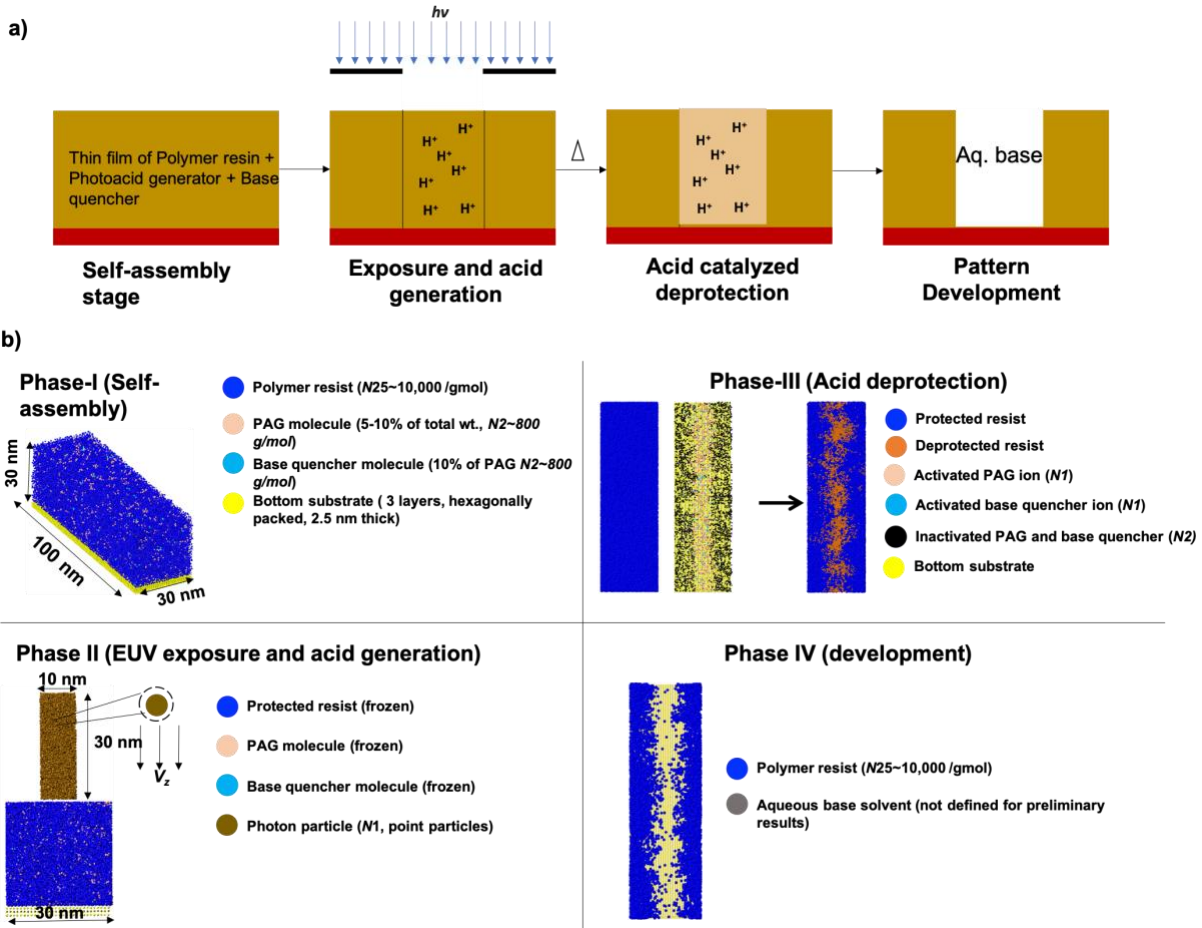


Figure 6.8: a) EUV process schematic b) Process stages and the individual components

In the *self-assembly* phase, the chemically amplified resist mixture is spin coated on the substrate. This mixture comprises of a polymer resin resist, a photoactivated acid group (PAG) molecule, and a base quencher^{32,33}. The substrate on which this mixture is coated mainly be Silicon with a layer of SiN. The polymer resin usually has a molecular weight between 5,000-10,000 g/mol with an expected radius of gyration between 6-10 nm. Chemically, the resin will have a etch-barrier, aliphatic backbone, acidic group and a protecting group. The etch-barrier provides the resist its

material property. The acidic group provides solubility to the resin and the protecting group makes it inert to removal by aqueous base solvents. The polymer resin can have different chemistries like Poly(4-hydroxystyrene) type, acrylate type and a hybrid of the two.

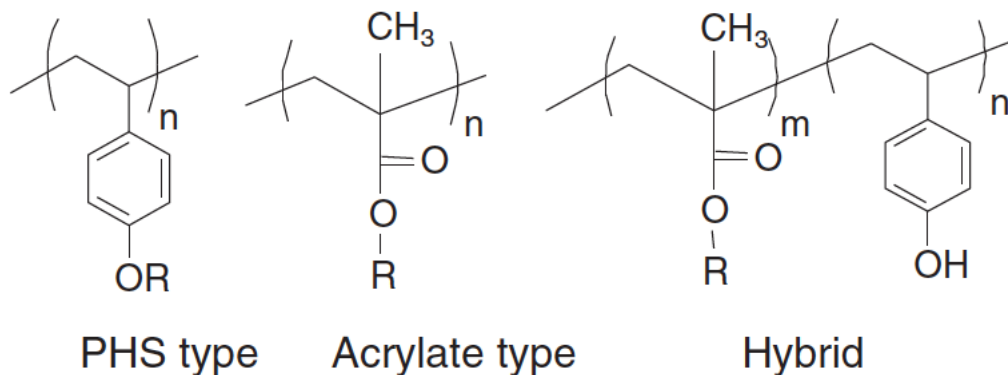


Figure 6.9: Polymer resin types for chemically amplified EUV resists

PAG molecule will comprise between 5-10% of the total resist weight. It usually consists of cationic and anionic part and interaction with a photon of a particular wavelength leads to dissociation of the PAG molecule in phase II, *photon absorption and acid generation*. For EUV resist, this wavelength will fall be around 13nm. Base quencher molecules are also photoactivated and is expected to react with photoacid to limit acid diffusion and thus reduce line-edge roughness.

A crucial distinction for EUV resists from Deep UV is that apart from the photogeneration of the acid from the PAG molecule either by photon absorption by the PAG molecule or by the resist and subsequent energy transfer to PAG, EUV photon also generate photoelectrons by initial absorption of photons. These photoelectrons along with the PAG acid further catalyze the deprotection reactions. It is important to note here that the as compared to 193 nm lithography, the number of photons are much lower in EUV and the energy per photon is thus significantly higher. The total

energy of the doses for EUV are also much lower. The discrete nature of photons and molecules in the resist and the interactions between them leads to more prominent stochastic defects failures. Photon generation can be modeled as a random process with a Poisson distribution, $\frac{\sigma_N}{N} = \frac{1}{\sqrt{N}}$, where N is the average number of photons and standard deviation of the number of photons is given by σ_N . As the photon density is quite low, any variability in this distribution can strongly affect the PAG generation and subsequent deprotection leading to defects or high edge roughness. Just as in 193nm and 193nm immersion lithography, masks can be used with various nanopatterns to form line and space patterns, contact holes or other specific patterns.

Post photoacid generation, the resist mixture is baked leading to acid diffuses through the resist in third phase of the process – *acid catalyzed deprotection*. The photoacid along with the secondary electrons catalyzes the deprotection reactions. The acid removes the deprotecting group making the resin soluble in aqueous base solvents. Finally, in phase-IV, *development*, the deprotected resin is carried away in the aqueous bath leaving behind a nano-pattern of the photo-resist.

6.2.3 MODELING DETAILS

A bead-spring coarse-grained model is adopted for the polymer resist additive mixture. The size of a coarse-grained bead, $\sigma = 1$ nm. Assuming a Poly(4-hydroxystyrene) type polymer resin, a coarse-grained bead is assumed to have about four 4-hydroxystyrene molecules ~ 400 g/mol. The polymer molecular weight considered is 10,000 g/mol with a chain length of $N25$. A short ranged fene bond potential is defined for the polymer resin. The PAG and base quencher molecules are also defined as the same size as the polymer for the preliminary trials. The PAG and base quencher short ranged interactions are defined with a harmonic bond.

$$U_{harmonic}(r) = \frac{1}{2}K (r - r_0)^2 \quad \text{equation 6.4}$$

$$k = \text{harmonic spring constant} = 30 \epsilon \sigma^{-2}$$

$$r_0 = \text{equilibrium bond length} = 1.2 \sigma$$

Interaction with photons can break this bond leading to release of the PAG acid. Similar to the SAM trials, the like interactions are defined by tail-corrected LJ potential,

$$U_{att}(r) = \begin{cases} 4\epsilon \left[\left(\frac{\sigma}{r}\right)^{12} - \left(\frac{\sigma}{r}\right)^6 \right] + S_{LJ}(r) & r < r_c \\ 0, & r > r_c \end{cases} \quad \text{equation 6.5}$$

$$S_{LJ}(r) = \begin{cases} C, & r < r_1 \\ \frac{a}{3}(r - r_1)^3 + \frac{b}{4}(r - r_1)^4 + C, & r_1 < r < r_c \end{cases} \quad \text{equation 6.6}$$

The unlike beads interact with the Weeks-Chandler Anderson potential,

$$U_{rep}(r) = \begin{cases} 4\varepsilon \left[\left(\frac{\sigma}{r}\right)^{12} - \left(\frac{\sigma}{r}\right)^6 \right], & r \leq 2^{\frac{1}{6}} \sigma \\ 0, & r > 2^{\frac{1}{6}} \sigma \end{cases} \quad \text{equation 6.7}$$

The depth of the potential well is assumed to $\varepsilon = 3.5$ KJ/mol with a baking temperature of $T=1.0$ ~390 K. The dimensions of the system are shown in figure 6.7b which corresponds to a system size 85,800 beads at a resist site density of 0.85 beads/ σ^3 . For phase-I, the system annealed for 0.5 million steps @ 0.01τ timestep ~ 88 ns.

6.2.4 RESULTS

6.2.4.1 Phase-I (Self-Assembly)

The resist mixture of the polymer, PAG and base quencher is allowed to self-assemble. The PAG concentration is varied at 5% and 10% and the number of base quencher beads is 10% of PAG. Two types of interactions for the additives are considered. PAG+base quencher can either react with the resist with an attractive potential (neutral overall) or with a repulsive potential (selective additives). As can be seen in figure 6.9a-b, the additive spread is uniform in all directions. The concentration plot in the x-direction is seen in figure 6.9b. Similar plots can also be generated for y and z directions. These plots show that irrespective of the additive interaction with the resist, similar concentrations of the additives leading to similar distribution spread. The interaction type is not as sensitive to the concentration spread as the PAG is only a dimer.

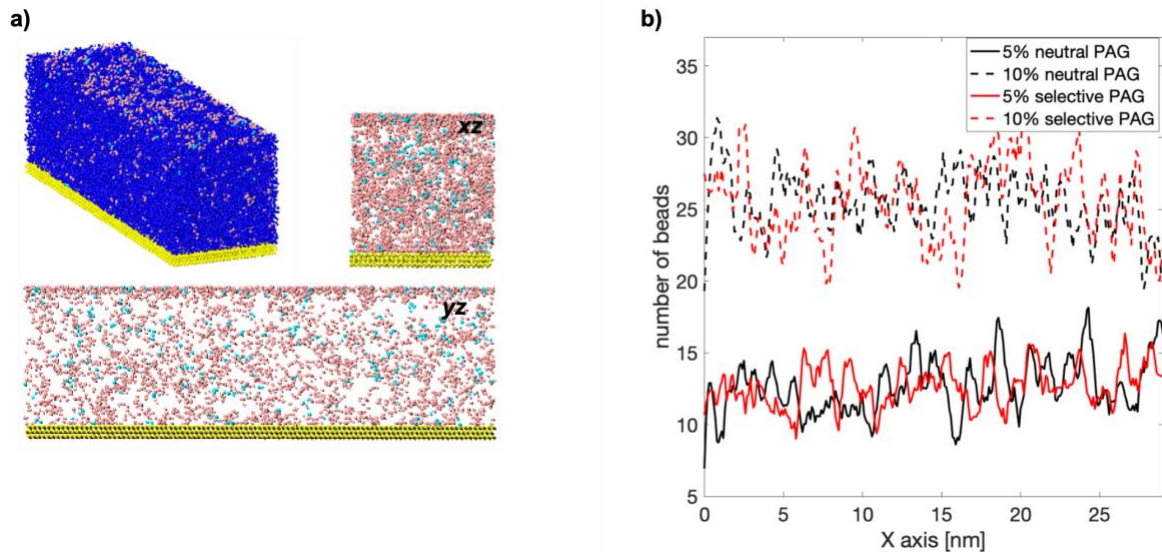


Figure 6.10: Morphology of the chemically amplified resist after phase-I. b) concentration spread for the additives for 6.10a.

6.2.4.2 Phase-II (Photon exposure and PAG dissociation)

Point particles (photons) generated above the polymer thin film. Particles can have specific z -velocity profile. Preliminary model assumes a delta function for velocity distribution, with no base quencher activation leading to close to 100% PAG activation in the 10 nm spacing. The particles do not interact with polymer CG beads. Particle generation pattern can be varied depending on the mask. Cationic PAG bead within reactive radius (R_{reax}) is changed to a different atom type after bond breakage. This event is stochastic with a user defined probability. Specific Monte-Carlo models can be generated for activation events. Post phase II completion, a fraction of cationic PAG bead / base quencher are changed into a different atom type as shown in figure 6.10a.

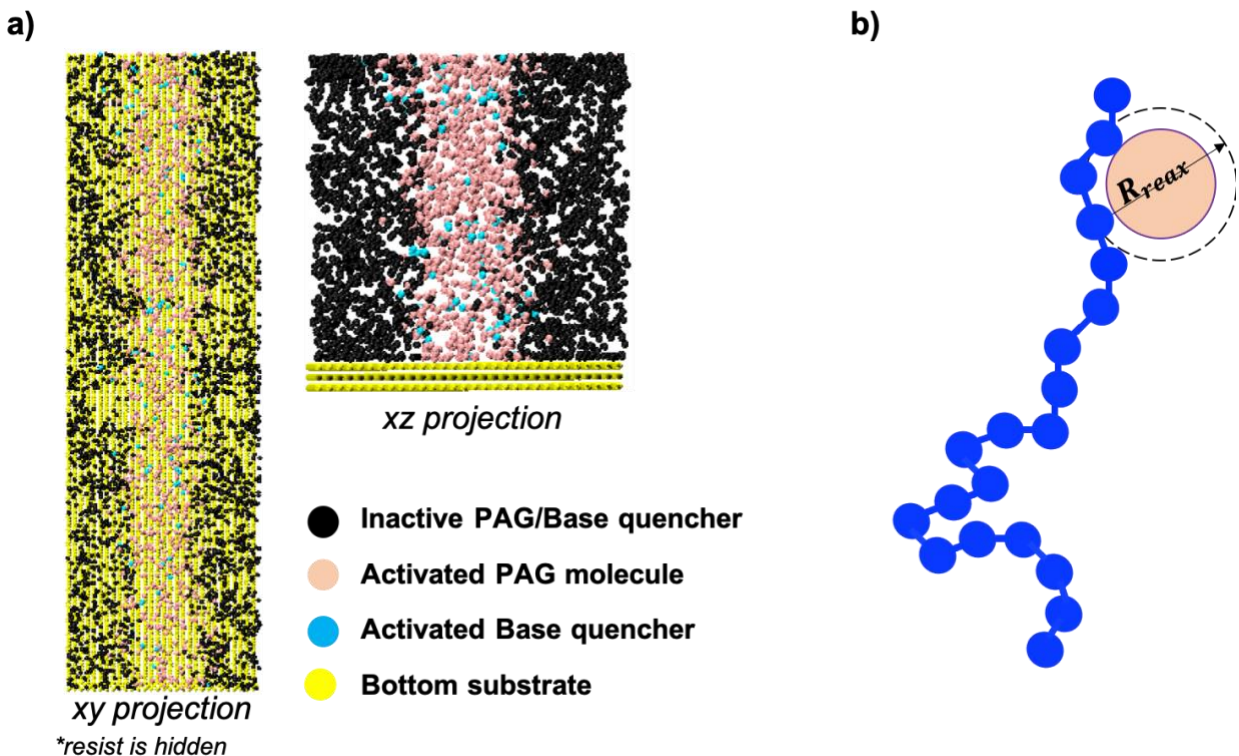


Figure 6.11: a) morphology post-EUV exposure and acid dissociation. b) schematic of attack of a reactive acid ion to a deprotected resist chain

6.2.4.3 Phase III (Acid deprotection) and Phase IV (development)

PAG and base quencher beads with new atom type are reactive beads and unexposed additive beads remain in the system. Polymer resin beads are unfrozen from phase and additive beads are allowed to diffuse at $T_{bake} \sim 390$ K. Acid bead within certain reactive distance of base quencher bead will be deleted or rendered unreactive. For the preliminary results, the base quencher action is not studied. A fraction of polymer resin bead within certain reactive distance (R_{reax}) of acid beads are changed to a different type and deleted in subsequent development phase. This fraction signifies the probabilities event that the acid interaction with the polymer resin can lead to deprotection. For the preliminary results, the fraction is assumed to be 1 leading to fast-deprotection kinetics. Development is defined by just deprotected bead removal. Effect of solvent on resist morphology is not studied.

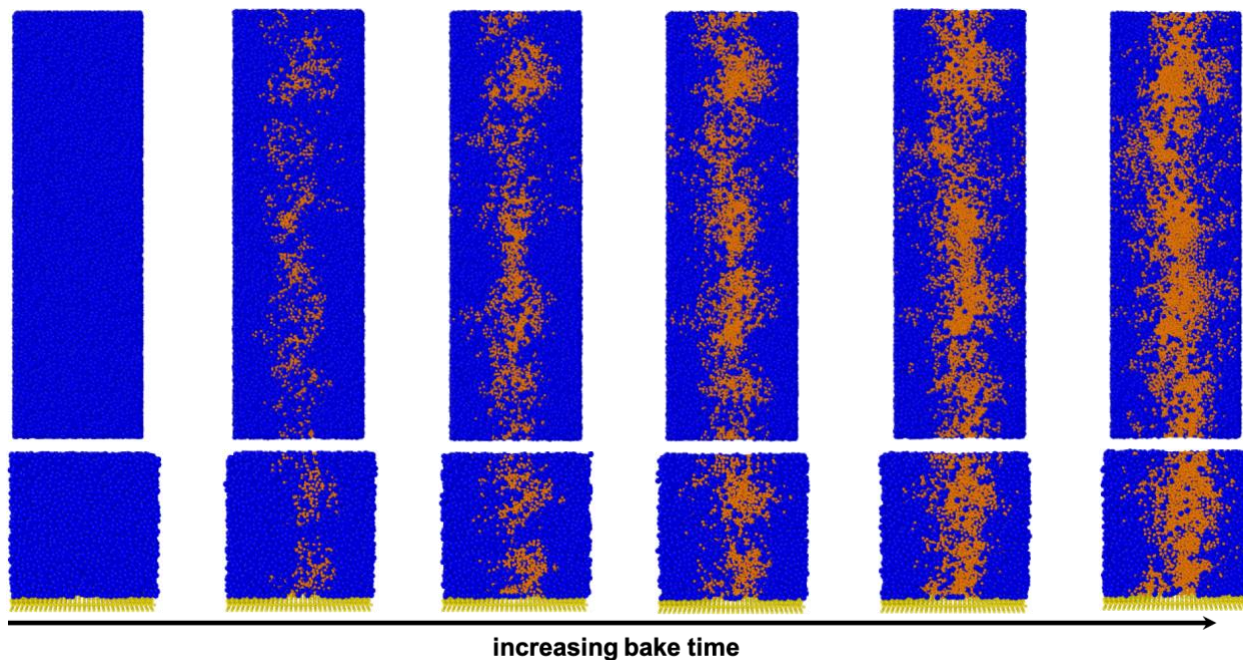
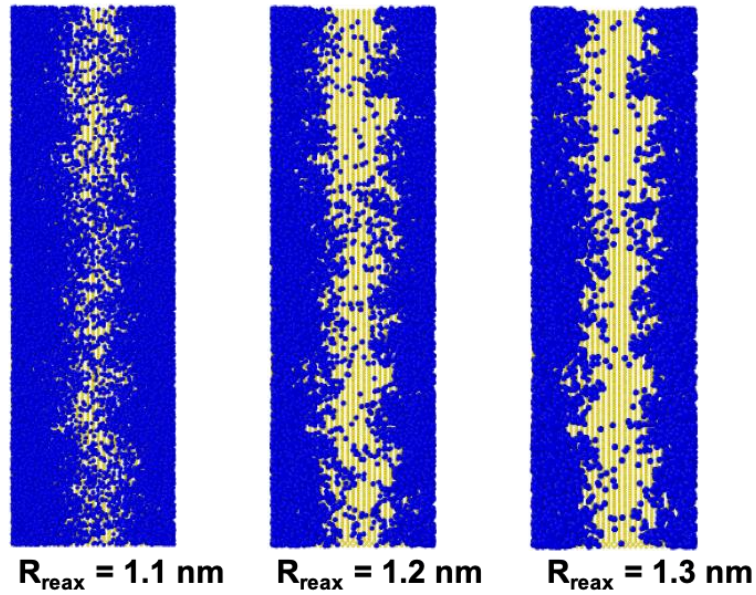


Figure 6.12: Acid deprotection kinetics. Protected resist beads are shown in blue while deprotected resist is shown in orange.

Another crucial parameter that has an effect on the deprotection kinetics is the extent of acid bead reactivity, R_{reax} . Three different R_{reax} of 1.1σ , 1.2σ and 1.3σ have been tried. The morphology post development at the same deprotection time along with the concentration spread is seen for the acid bead reactivity. Higher the R_{reax} , longer deprotection time are required to form an appropriate pattern which in this case is a line. As the figure 6.12 shows, for the same deprotection time, higher R_{reax} leads to more deprotection of the polymer. Hence for the region where the photon is dosed, the concentration of resist beads is the lowest. It is also important to note that for higher deprotection times when the acid bead is allowed to diffuse further into the resist, defects can arise in the form resist pores or resist edge roughness. Using base quenchers will not only lead to slower deprotection kinetics but also reduce these defects.

a)

different acid reactivity at same acid-diffusion time



b)

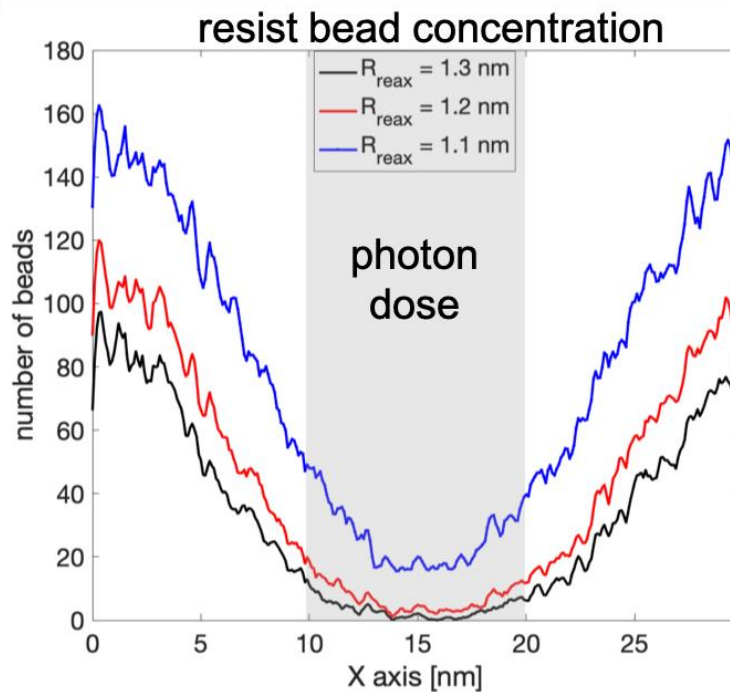


Figure 6.13: a) Effect of acid reactivity with variable acid bead reactive radius on deprotection. b) acid bead concentration across patterned substrate post deprotection and development. The mask allows photons to pass through 10-20 nm. Higher reactive radii leads to lower concentration in the photon dose area.

6.2.5 SUMMARY

Preliminary coarse-grained molecular dynamics simulations were performed to model EUV lithography. The first phase is the self-assembly phase in which the chemically amplified resist mixture of polymer resin, PAG and base quencher is baked. The distribution of the additives in the resin is uniform in all directions. Upon the self-assembly, photon particles are generated above the resist for the EUV exposure, which are imparted a z-velocity. As the photons interact with the additives, the PAG gets dissociated to form an acid cation. This acid bead then diffuses and deprotects the polymer resist. The deprotected polymer is developed to reveal the resist nanopattern. Preliminary results show the importance of the reactive radius of the acid bead and how it affects the deprotection kinetics.

6.3 REFERENCES

1. Moore GE. Cramming more components onto integrated circuits, Reprinted from Electronics, volume 38, number 8, April 19, 1965, pp. 114 ff. IEEE Solid-State Circuits Society Newsletter. 2006 Sep;11(3):33-5.
2. Waldrop MM. The chips are down for Moore's law. Nature News. 2016 Feb 11;530(7589):144.
3. Ramm P, Klumpp A, Weber J, Lietaer N, Taklo MM, De Raedt W, Fritzsche T, Couderc P. 3D integration technology: Status and application development.
4. Sunday DF, Kline RJ. Reducing block copolymer interfacial widths through polymer additives. Macromolecules. 2015 Jan 16;48(3):679-86.
5. Zhang X, He Q, Chen Q, Nealey PF, Ji S. Directed Self-Assembly of High χ Poly (styrene-*b*-(lactic acid-*alt*-glycolic acid)) Block Copolymers on Chemical Patterns via Thermal Annealing. ACS Macro Letters. 2018 Jun 6;7(6):751-6.
6. Wang HS, Kim KH, Bang J. Thermal Approaches to Perpendicular Block Copolymer Microdomains in Thin Films: A Review and Appraisal. Macromolecular rapid communications. 2018 Nov 30:1800728.

7. Park MH, Jang YJ, Sung-Suh HM, Sung MM. Selective atomic layer deposition of titanium oxide on patterned self-assembled monolayers formed by microcontact printing. *Langmuir*. 2004 Mar 16;20(6):2257-60.
8. Ulman A. *Ultrathin Organic Film*. Academic Press. San Diego, CA. 1991.
9. Swalen JD, Allara DL, Andrade JD, Chandross EA, Garoff S, Israelachvili J, McCarthy TJ, Murray R, Pease RF. Molecular monolayers and films. A panel report for the Materials Sciences Division of the Department of Energy. *Langmuir*. 1987 Nov;3(6):932-50.
10. Schreiber F. Structure and growth of self-assembling monolayers. *Progress in surface science*. 2000 Nov 1;65(5-8):151-257.
11. Ulman A. Formation and structure of self-assembled monolayers. *Chemical reviews*. 1996 Jun 20;96(4):1533-54.
12. Kim H, Saha JK, Zhang Z, Jang J, Matin MA, Jang J. Molecular dynamics study on the self-assembled monolayer grown from a droplet of alkanethiol. *The Journal of Physical Chemistry C*. 2014 May 9;118(20):11149-57.
13. Aswal DK, Lenfant S, Guerin D, Yakhmi JV, Vuillaume D. Self assembled monolayers on silicon for molecular electronics. *Analytica chimica acta*. 2006 May 24;568(1-2):84-108.

14. Alaboson JM, Wang QH, Emery JD, Lipson AL, Bedzyk MJ, Elam JW, Pellin MJ, Hersam MC. Seeding atomic layer deposition of high-k dielectrics on epitaxial graphene with organic self-assembled monolayers. *ACS nano*. 2011 May 12;5(6):5223-32.
15. Aizenberg J, Black AJ, Whitesides GM. Control of crystal nucleation by patterned self-assembled monolayers. *Nature*. 1999 Apr;398(6727):495.
16. Xu S, Miller S, Laibinis PE, Liu GY. Fabrication of nanometer scale patterns within self-assembled monolayers by nanografting. *Langmuir*. 1999 Oct 12;15(21):7244-51.
17. Ginger DS, Zhang H, Mirkin CA. The evolution of dip-pen nanolithography. *Angewandte Chemie International Edition*. 2004 Jan;43(1):30-45.
18. Piner RD, Zhu J, Xu F, Hong S, Mirkin CA. "Dip-pen" nanolithography. *science*. 1999 Jan 29;283(5402):661-3.
19. Maiti PK, Lansac Y, Glaser MA, Clark NA, Rouault Y. Self-assembly in surfactant oligomers: a coarse-grained description through molecular dynamics simulations. *Langmuir*. 2002 Mar 5;18(5):1908-18.
20. Telo da Gama MM, Gubbins KE. Adsorption and orientation of amphiphilic molecules at a liquid-liquid interface. *Molecular Physics*. 1986 Oct 10;59(2):227-39.

21. Grest GS, Kremer K. Molecular dynamics simulation for polymers in the presence of a heat bath. *Physical Review A*. 1986 May 1;33(5):3628.
22. Smit B, Hilbers PA, Esselink K, Rupert LA, Van Os NM, Schlijper AG. Computer simulations of a water/oil interface in the presence of micelles. *Nature*. 1990 Dec;348(6302):624.
23. Menger FM, Littau CA. Gemini-surfactants: synthesis and properties. *Journal of the American chemical society*. 1991 Feb;113(4):1451-2.
24. Wu B, Kumar A. Extreme ultraviolet lithography: a review. *Journal of Vacuum Science & Technology B: Microelectronics and Nanometer Structures Processing, Measurement, and Phenomena*. 2007 Nov 11;25(6):1743-61.
25. Moore SK. Getting EUV Ready for 2020 [Internet]. *IEEE Spectrum: Technology, Engineering, and Science News*. IEEE Spectrum; 2018 [cited 2019Jan18]. Available from: <https://spectrum.ieee.org/nanoclast/semiconductors/nanotechnology/getting-euv-ready-for-2020>
26. Sperling ED. EUV's Uncertain Future [Internet]. *Semiconductor Engineering*. 2018 [cited 2019Jan18]. Available from: <https://semiengineering.com/euvs-uncertain-future/>
27. Biafore JJ, Smith MD, van Setten E, Wallow T, Naulleau P, Blankenship D, Robertson SA, Deng Y. Resist pattern prediction at EUV. In *Extreme Ultraviolet (EUV) Lithography 2010* Mar 20 (Vol. 7636, p. 76360R). International Society for Optics and Photonics.

28. Brainard RL, Trefonas P, Lammers JH, Cutler CA, Mackevich JF, Trefonas A, Robertson SA. Shot noise, LER, and quantum efficiency of EUV photoresists. In Emerging Lithographic Technologies VIII 2004 May 20 (Vol. 5374, pp. 74-86). International Society for Optics and Photonics.
29. Kozawa T. Relationship between Stochastic Effect and Line Edge Roughness in Chemically Amplified Resists for Extreme Ultraviolet Lithography Studied by Monte Carlo Simulation. Japanese Journal of Applied Physics. 2012 Jul 31;51(8R):086504.
30. Patsis GP, Constantoudis V, Gogolides E. Effects of photoresist polymer molecular weight on line-edge roughness and its metrology probed with Monte Carlo simulations. Microelectronic engineering. 2004 Sep 1;75(3):297-308.
31. Levinson HJ. Principles of lithography. SPIE press; 2005.
32. Ober CK, Xu H, Kosma V, Sakai K, Giannelis EP. EUV photolithography: resist progress and challenges. In Extreme Ultraviolet (EUV) Lithography IX 2018 Mar 19 (Vol. 10583, p. 1058306). International Society for Optics and Photonics.
33. Itani T, Kozawa T. Resist materials and processes for extreme ultraviolet lithography. Japanese Journal of Applied Physics. 2012 Dec 14;52(1R):010002.